NASA Contractor Report 187576

STATIC STRAIN AND VIBRATION CHARACTERISTICS OF A METAL SEMIMONOCOQUE HELICOPTER TAIL CONE OF MODERATE SIZE

Richard L. Bielawa, Rachel E. Hefner, and Andre Castagna

RENSSELAER POLYTECHNIC INSTITUTE
Troy, New York

Grant NAG1-807
June 1991

National Aeronautics and Space Administration

Langley Research Center
Hampton, Virginia 23665-5225

STATIC STRAIN & VIBRATION CHARACTERISTICS OF A METAL SEMIMONOCOQUE HELICOPTER TAIL CONE OF MODERATE SIZE

by

Richard L. Bielawa
Associate Professor

Rachel E. Hefner
Graduate Research Assistant

Andre Castagna
Graduate Research Assistant

Department of Mechanical Engineering,
Aeronautical Engineering and Mechanics

Rensselaer Polytechnic Institute
Troy, New York 12180–3590

ABSTRACT

This report presents the results of an analytic and experimental research program involving a Sikorsky S–55 helicopter tail cone directed ultimately to the improved structural analysis of airframe substructures typical of moderate sized helicopters of metal semimonocoque construction. The study included experimental static strain and dynamic shake–testing measurements as well as correlation studies of each of these tests with a PC–based finite element analysis (COSMOS/M). The tests included static loadings at the end of the tail cone supported in the cantilevered configuration as well as vibrational shake–testing in both the cantilevered and free–free configurations. Generally, excellent to very good correlations were achieved for the first order elasto–mechanical effects. The tests and correlational analyses, while falling short of the ultimate objectives of effecting improved correlation and detailed characterization of damping, represent achievement in firmly establishing the RPI Shake–Test Facility as well as the basic finite element modeling of the S–55 tail cone, as operational resources. As a result, these resources are now poised to address the ultimate objectives indentified above.

ACKNOWLEDGEMENTS

The research leading to the results reported here was directly supported by NASA Contract No. NAG–1–807. The development of the RPI Airframe Component Shake–Test Facility was supported in part by the Army Research Office through the Rotorcraft Technology Center at Renssleaer Polytechnic Institute under contract No. DAAG 29–82–K–0093. Instrumentation used for the experimental phase of the program was purchased in part under NSF Equipment Grant No. MSM–8806257. The S–55 tail cone was donated to RPI by the Sikorsky Aircraft Division, United Technologies Corporation. Also, special thanks go to the Hewlett–Packard Corporation for software which greatly facilitated the experimental data reduction.

TABLE OF CONTENTS

LIST OF FIGURES

LIST OF TABLES

NOMENCLATURE

E	= Young's modulus of (bending) elasticity lb/in^2
EI	= bending stiffness, $lb–in^2$
f	= frequency, Hz
f_n	= nth natural frequency, Hz
G	= modulus of (shearing) elasticity, lb/in^2
m_s	= mass distribution of the tail rotor shaft (devoid of bearings), $lb–sec^2/in^2$
M_{b_i}	= mass of the ith tail rotor shaft support bearing, $lb–sec^2/in$
M_s	= mass of tail rotor shaft (devoid of support bearings), $lb–sec^2/in$.
R	= radius of a section of the tail cone at longitudinal station z, in., also, electrical resistance, ohm
s	= circumferential distance along the outside of a section, in.
S_g	= strain gage factor, $mV/\mu strain$
V	= signal voltage, m volts
x, y, z	= global cartesian coordinate system, x is (+) horizontal to starboard, y is (+) upward and z is (+) aft.
x', y', z'	= local cartesian coordinate system, as relates to finite element shell elements.
z_{cg}	= component of center of mass location in z direction, in.
γ	= shear strain, μ in/in.
ϵ	= axial strain, μ in/in.
θ	= circumferential angular coordinate starting at the horizontal starboard side and proceeding upward, deg.
ν	= Poisson's ration
ρ	= density, $lb–sec^2/in^4$
ω	= frequency, rad/sec

1.0 INTRODUCTION

1.1 Background

Recent studies within industry and government research facilities have identified a substantial inability to predict helicopter vibration levels analytically either with required acuracy or in a timely enough manner to impact on the final design of the airframe. Basically, the problem of accurately predicting helicopter vibration levels turns on three technical disciplines: (1) prediction of rotor loads and impedances, (2) prediction of fuselage dynamic mobilities for excitations at the rotor hub and other locations of high aerodynamic excitation, and (3) formulation of an accurate and practical method for coupling the rotor dynamic characteristics with those of the fuselage.

Of these three disciplines the third, that of rotor–fuselage coupling, appears to be in the best shape technically; the first, that of accurately predicting rotor loads and impedances continues to be a difficult problem but is currently being well addressed and is potentially one ripe for a solution. As identified by the industry and governmental studies, which have focused on the fuselage dynamics technical area, a present fundamental technological deficiency can be stated:

> *Despite carefully bringing to bear current state–of–the–art techniques in finite element analysis modeling, the prediction of fuselage dynamic characteristics is still not nearly accurate enough for practical fuselage vibration prediction.*

Furthermore, several problem areas relating to this general inability to predict fuselage dynamic characteristics have been identified which point to the need for continued studies of a basic research nature. Examples of such problem areas include :

(1) The ability to model complex structures typical of helicopter fuselages with their characteristic attendant cut outs and concentrated masses in terms of finite element masses and stiffnesses must be validated and made more accurate. This strengthening of accurate finite element modeling must begin at the substructure level and will necessarily require code validation using realistic shake test results for representative helicopter substructures.

(2) The ability to predict the discrete mass modeling of special fuselage components, i.e., those with unique elastic attachments, requires upgrading with appropriate experimental validation.

(3) The damping characteristics of helicopter fuselage substructures have to be adequately quantified with regard to construction type (metal semimonocoque vs. composite), size and vibrational environment. This quantification requires the testing of realistic substructures for their dissipative properties.

(4) Analytical methods presently exist and new ones are under development for integrating the separate dynamic characteristics of substructures to define those of the composite whole. The validation of these methods has not yet been acomplished for realistic complex structures representative of helicopter fuselages.

1.2 Research Objectives

The research objectives of this study were directed at the structural dynamic characteristics of a structural component (tail cone) of a typical helicopter of moderate size and metal semimonocoque construction (Sikorsky S–55). Specific research objectives relating to this tail cone are:

(1) To establish and validate finite element modeling predictions of the basic dynamic characteristics (natural frequencies) of a moderate sized (S–55) helicopter tail cone.

(2) To lay the groundwork for quantifying specific dynamic characteristics such as structural damping of structures typified by helicopter tail cones of moderate size and of metal semimonocoque construction.

The objectives of this research program were met with a combined experimental and analytical study using the RPI Airframe Component Shake–Test Facility, the S–55 tail cone and an appropriate finite element modeling (FEM) analysis, COSMOS/M (Ref. 1). All required instrumentation resides at RPI in the form of shakers, accelerometers, load cells, recorders and a dual–channel frequency spectrum analyzer. One item which was fabricated for this research is an adapter ring for mounting the S–55 tail cone to the hard–back structure. This adapter ring was required because of the nonplaner base section

of the tail cone resulting from the tail rotor drive shaft spline. Fabrication of this adapter ring was a straightforward machining task and represented minimum cost to the research program.

1.3 Technical Program

The research program consisted of four major phases, three experimental and one analytical. All of the experimental phases were performed in the RPI Airframe Component Shake–Test Facility located within the high–bay area of the RPI Jonsson Engineering Center. The tests were performed either with the tail cone mounted to a hard–back structure (described in more detail in a later section) or suspended in a simulated free–free configuration using bungee cords. The three experimental phases are further described as follows:

1. Static strain–testing

The initial experimental phase of the study dealt with obtaining measurements of the strain state at selected locations on the tail cone which could be expected to experience relatively high stresses due to static loads applied laterally at the tail cone free end. The strain states were obtained using strain gage rosettes and after suitable conversions principal strains were obtained suitable for correlation with finite element modeling predictions. The purpose of this experimental phase was to provide a relatively elemental correlational basis for validating the stiffness modeling before attempting correlation with the experimental shake–test results.

2. Shake–testing – cantilevered configuration

This test activity was directed at determining the resonance and anti–resonance response characteristics of the tail cone with the tail cone mounted in the cantilevered configuration. In this mode of testing the oscillatory shaker load was applied at the free (aft) end initially horizontally and then later at an oblique (60 deg.) angle to the horizontal, both using burst–chirp excitations. The specific experimental data obtained were in the form of amplitudes of frequency response functions for each of the various accelerometer locations.

3. Shake–testing – free–free configuration

This test activity was directed at providing an alternate set of frequency response data involving again resonance and anti–resonant response characteristics. This phase was performed using bungee suspension techniques in conjunction with the overhead crane available to the Airframe Component Shake–Test Facility. For this test the excitation shaker force was horizontally directed and the swept sine mode of excitation was used.

4. Correlation with FEM analysis

This activity was performed in two subphases: (1) preparation of the finite element modeling input data, and (2) actual running of the FEM code with the prepared data. To this end, since it is unlikely that original FEM data actually existed for this helicopter component, these required FEM data were generated from original engineering prints of the tail cone supplied to RPI by Sikorsky Aircraft Division of United Technologies, the original manufacturers of the tail cone. It is believed that this "starting–from–scratch" approach to the preparation of the data worked as an advantage in that it allowed maximum control over the modeling techniques and, therefore, avoided any previous analyst's possible errors in either judgement or calculation.

Within the context of the above described basic phases of the research project, the following specific tasks were to be performed:

(1) Fabricate an adapter ring, and attach tail cone to to the hard–back structure in the cantilevered configuration.

(2) Install strain gage instrumentation and mounting points for accelerometers.

(3) Conduct static deflection tests, with applied loads at the free end of the tail cone, to provide static deflection data for FEM stiffness description correlation purposes.

(4) Conduct dynamic shake–tests on the tail cone in the cantilevered mount arrangement to provide frequency response data suitable for FEM correlation.

(5) Repeat above Task (4) but with the tail cone suspended in a simulated free–free mount arrangement.

(6) Prepare input data for FEM analysis from engineering drawings and measurements made from the test article itself.

(7) Make FEM calculations for (a) static strains resulting from a lateral load at the aft end and (b) the modal characteristics and frequency response functions for the two dynamic test configurations.

(8) Repeat tests and/or rerun FEM analysis, as appropriate, to devise ways of improving the correlation.

2.0 DESCRIPTION OF EXPERIMENTAL EQUIPMENT AND PROCEDURES

2.1 Airframe Component Shake–Test Facility at RPI

Initial development activities at Rensselaer Polytechnic Institute (RPI) were directed at enlarging the test area itself and to modifying the vibration isolation pad within the laboratory test area. The test area was enlarged to an area of 456 sq ft. (24' x 19'). This area now accommodates structural components with substantial length (up to 20 ft.), and widths up to 12 ft. and is thus ideal for the acquired tail cones (those from a Sikorsky S–55, and two from Bell OH–58A's). The isolation pad consists of a 10,000 cu. ft concrete block imbedded in the laboratory floor with an elastomeric interface and resting on a refusal pile. Modifications to the isolation pad were made for the purpose of efficiently attaching a "hard–back" structure to it.

The hard–back structure, currently in position on the isolation pad, provides a 4 ft wide x 5 ft. high vertical mounting surface for the test articles (see Fig. 1.). The purpose of this structure is to provide a "rigid" vertical attachment surface for a cantilevered (horizontal) mounting of any of the acquired tail cones relative to the vibration isolation pad. As described on Ref. 2, the hard–back structure was designed to have its lowest natural frequency to be no lower that 100 Hz and to be fabricated as a weldment of 2 in thick steel planes. The design was quite successful in meeting these specifications and, although settling resulted (in the attachment bolts, most likely) in some frequency shifting, the hard–back maintains a first natural frequency in excess of 100 Hz. This mode is essentially a cantilever, symmetric fore–and aft rocking mode with the face plane kept rigid.

2.2 Description of Sikorsky S–55 Helicopter Tail Cone

Basic primary structure

The S–55 tail cone, as shown installed on the hard–back structure in Fig. 2, is a conical metal semimonocoque structure, with approximate dimensions of 198 in. in length, 36 in. OD at the base and 11 in. OD at the aft end. Its frames are made of Alclad 2024 and skins are made of magnesium. The tail cone was constructed by wrapping magnesium

skins around Alclad frame rings. All sheets of magnesium were riveted to the Alclad frames. The doublers and stiffeners were in turn riveted to the magnesium skins. In addition, the end frame is actually a relatively more robust magnesium casting intended for accommodating the loads required for supporting an angle gear box which normally is attached at this point.

Tail rotor drive shaft

The tail rotor drive shaft assembly consists of a rotating steel shaft and seven identical sets of bearings and nonrotating bearing mounts. The bearing mounts are each connected to the tail cone with L–shaped braces. Pertinent dimensions of the shaft assembly are shown in Fig. 3. The shaft assembly was removed by unbolting the bearing mounts from the L–braces to allow the shaft mass and stiffness properties to be determined. However, the lightweight sheet metal bearing mounts themselves could not be removed from the tail cone.

The mass of each of the individual bearing mounts, as well as that of the shaft, was calculated as follows. The shaft assembly was first weighed to find the total drive shaft assembly weight, M. Next, the center of gravity was located by balancing the shaft assembly on a narrow horizontal bar. The bearing mass, M_b , and shaft mass, M_s , were then calculated from the following equations:

$$(7)\ M_b + M_s = M$$
$$M\, z_{cg} = M_s\,(L/2) + M_b\,(z_{b_1} + z_{b_2} + \ldots z_{b_7})$$

where m is the total mass; z_{cg} is the horizontal location of the total mass center of gravity; L , is the total length, and z_{b_1}, z_{b_2}, ... are the respective horizontal locations of each bearing mass. By this simple means the bearing mass, M_b, was found to be .0313 lb–sec^2/ft , and the shaft mass, M_s , .520 lb–sec^2/ft.

The lateral bending stiffness, EI_s , was determined experimentally. The first natural bending frequency was measured by securing the shaft assembly to a frame with a C–clamp in a cantilevered fashion at the shaft's mass center. Oscillations were induced by striking the end, and the natural frequency was measured to be 16.197 rad/sec. Standard beam vibration theory (Ref. 3) gives the theoretical expression for the first natural frequency as:

$$\omega_1 = \sqrt{\frac{EI_s}{m_s L^4}}$$

where m_s is mass per length of the shaft and L is its length. By this procedure a value of 7.634×10^5 lb–in^2 was calculated for EI_s.

The material of the shaft was still unknown, but since the drive shaft was magnetically active a hardened steel alloy was assumed. It was possible to check the validity of the assumption by first calculating the inner shaft radius from the following equation:

$$M_s = \pi\rho\,(R_0^2 - R_i^2)\,L$$

where ρ is the density of hardened steel, R_0 and R_i are, respectively, the outer and inner radii of the shaft (R_0 was measured to be .565 in.), L is the shaft length (measured to be 218.28 in.), and M_s is the shaft mass. The inner radius, R_i , was thereby inferred to be .388 in. The geometric cross sectional area moment of inertia for a hollow tube was calculated from the standard formula for a concentric annular area

$$I = \frac{\pi}{4}(R_0^4 - R_i^4)$$

By using this formula, the area moment of inertia was calculated to be .2644 in^4. With this value, and a typical value of Young's modulus for hardened steel of 29×10^6 lb/in^2, a value of 7.667×10^5 lb–in^2 was then found for EI_s ; this value agrees with the value found earlier. These geometric and material properties were then used in creating an appropriate finite element representation of the drive shaft assembly portion of the tail cone.

2.3 Description of Suspension Configurations

The tail cone was suspended in both cantilever and free–free configurations during the experimental static strain and dynamic frequency response tests. Four tests were performed in all:

1. Static strain test – cantilevered suspension (mounted to hard–back)
2. Frequency response – cantilevered suspension – horizontal shake
3. Frequency response – cantilevered suspension – oblique shake
4. Frequency response – free–free suspension – horizontal shake

For both the cantilevered suspension tests of the tail cone, the tail cone was bolted to the hard–back. Test no. 2 represented the first attempt at performing the dynamic shake–testing of the tail cone. This test was was performed with the tail rotor drive shaft assembly retained and with the excitation implemented by means of a horizontal tensile force (vibratory excitation force superimposed on a static tensile load) using a wire stinger bungee cord arrangement.

As a result of difficulties experienced in modeling the rubber bearing mounts accurately in the finite element analysis, the results for this configuration were used only as a guide to future tests. For all subsequent tests the drive shaft was removed in order to eliminate this item. The alternative would have required either considerable subjective engineering judgements to be made and/or the consumption of time and resources which was beyond the scope of this study. Also, in an attempt to provide more excitation of all modes (both vertical and horizontal) the second cantilevered suspension configuration (Test no. 3) was performed with a rigid (non–tensile) stinger mounted oblique to the horizontal. For the free–free suspension, the drive shaft was again removed and the tail cone was suspended from the overhead ceiling crane of the laboratory by two lengths of bungee cord bundles, each having five individual cords and attached respectively to the bearing mounts at frames 60.375 and 129.0 (see Fig. 4).

2.4 Loading Configurations

All loads, both static and dynamic, were applied at the free end of the tail cone by utilizing the hexagonal arrangement of studs attached to the magnesium casting at the free end (frame 212.0). A simple aluminum bar with an attached hook eye was fashioned and bolted to this stud arrangement. For static loadings a lateral load was applied to the hook eye and for dynamic loadings the load was applied directly at the end of the bar in series with a dynamic load cell (part of an impedance head).

All static loads were generated with a cable, (attached at one end to the hook eye) which underwent a right angle direction change (horizontal to vertical using a fixed pulley) to a weight platform attached to the other end (see Fig. 5). The weight platform allowed ten pound weights to be incrementally added to vary the tail cone lateral test load. In these tests a simple strain gage instrumented load cell was fashioned from a length of 3.870 in OD × 3.308 in ID aluminum cylindrical stock and used to verify the loadings. A detailed description of the design and fabrication of this load cell is given in Ref. 4.

For the initial shake–test configuration (cantilever mount, horizontal excitation) the shaker was attached to the aluminum bar (with intervening impedance head dynamic load cell) by means of a length of stainless steel piano wire in tension. The wire, which passed entirely through the hollow length of the shaker armature, was attached to the armature by means of a standard wire chuck. One end of the wire was thus attached to the dynamic load cell, the other end was attached to a set of bungee cords which were stretched to the load saturation point (point of negligible spring rate). The other end of the bungee cords were in turn attached to a bracket installed in a far wall in the Jonsson Engineering Center high–bay area.

For all subsequent shake–tests the excitations were either made oblique to the horizon (cantilever mount) or in a mode which could not accommodate a large tension force (the free–free configuration). For these configurations the vibratory shaker force was transmitted to the aluminum bar (and dynamic load cell) by means of a short length of 0.25 in OD hollow aluminum tubing without initial tension or compression.

2.5 Description of Instrumentation Hardware

Accelerometers and power units:

The accelerometers are compact units manufactured by PCB Piezotronics, Inc. and are of two types: PCB 303A and PCB 303A11 (high sensitivity). These accelerometers are of piezoelectric type and are structured with permanently polarized compression mode quartz elements and a microelectronic amplifier housed in a compact, light–weight metal case. The PCB model 303A has a nominal sensitivity of 10mV/g and the high sensitivity PCB model 303A11 has a nominal sensitivity of 100 mV/g. A PCB model 483A08 multi–channel rack power unit was used in conjunction with these accelerometers and load cell. This power unit has six channels, adjustable gain and buffered output capacity so that a maximum of five simultaneous response accelerations could be measured relative to the excitation load. In–depth descriptions of these and all other PCB instrumentation devices used are available in Ref. 5.

Accelerometer locations:

A number of locations wer reserved on the tail cone for accelerometer placement. As listed in Table 1, locations 1 through 20 are defined by blocks mounted on the sides of the tail cone and have vertical and horizontal threaded holes for mounting the accelerometers in the x– and y– directions (see Fig. 6). Additionally, the global coordinate directions of the accelerometer locations are also given below in Table 1. The coordinate directions for these accelerometers are described by a right–handed system wherein the positive z direction points aft towards the tailrotor (aft) end of the tail cone.

Table 1 – Accelerometer/load cell locations and corresponding finite element nodes

location no.	θ (deg)	z (in)	FEM node no.
1R	0	16.72	382
2R	0	25.64	435
3R	0	48.23	618
4R	0	60.08	702
5R	0	82.48	860
6R	0	94.52	942
7R	0	116.70	1040
8R	0	128.98	1088
9R	0	163.17	1160
10R	0	197.82	1208
*11R	0	213.23	1304
*12R	300	213.23	1308
1L	180	16.53	394
2L	180	25.33	447
3L	180	48.23	630
4L	180	60.02	714
5L	180	82.54	872
6L	180	94.15	954
7L	180	116.94	1052
8L	180	129.01	1100
9L	180	162.95	1172
10L	180	197.14	1220
11L	180	213.23	1316
12L	120	213.23	1320

* load cell locations (All other locations are for accelerometers.)
[Note: (R) refers to starboard side, (L) refers to port side]

Calibration Exciter:

Although all accelerometers come from the manufacturer with calibration sheets, on site checks of the calibration factors are still a good idea to ensure accuracy. One method of checking these calibration factors is with the use of a standard (vibratory) acceleration. Such a standard acceleration is available with the use of a precision calibration exciter. The calibration exciter used in this study is a Brüel & Kjaer Type 4294, as described in Ref. 6. This calibration exciter is a convenient hand–held unit which produces a reference acceleration level of 10 m/sec^2 at a frequency of 159.2 Hz (ω = 1000 rad/sec)

Dynamic load cell:

The dynamic loads at the point of vibratory load application was measured using a PCB model 288B02 mechanical impedance sensor. [In these tests the accelerometer output from this transducer was not used as that channel requires a special integrating amplifier which wasn't available.] Similar to the PCB accelerometers used the PCB model 288B02 is ruggedly constructed with rigid quartz stress elements operating in the compression mode and built–in microelectronic line drive amplifiers. The force sensor part of the PCB model 288B02 has a usable range of ± 50 lb and a nominal sensitivity of 100 mV/lb.

Electrodynamic shaker and power amplifier:

The electrodynamic shaker used is an MB Dynamics model 50A exciter. This shaker has a maximum rating of 50 pounds (peak) and a 1.0 inch total displacement when a 250 volt–ampere amplifier and the optional forced air cooling of the exciter is used. Cooling limitations reduce the rating to 25 pounds (peak) if forced air is not available. the frequency range available is from DC to 2000 HZ. This shaker was used in two modes of suspension: suspension using cables and simple placement on the floor, as shown in Figs. 7 and 9, respectively. Note the aluminun load application bar attached to the tail cone end in each of these figures. In the (horizontal) cable suspension mode (as shown in Fig. 7), the shaker was suspended from an angle iron assembly with adjustable cables whose lines of force approximate a coincidence with the shaker mass center. The angle iron assembly was in turn attached to a rectangular frame mounted to a massive iron base which rested on the floor. For shake–tests involving oblique excitations the suspension mode could not be used. However, the geometry of the tail cone free end relative to the floor and shaker dimensions readily allowed the use of a simple positioning of the shaker on the floor with a rigid sting, as shown in Fig. 8. This shaker was driven with the matching MB Dynamics model SS250 power amplifier. Specifications for this power amplifier are as follows:

a) single channel, high output power amplifier
b) output capability of 180 watts minimum into a 16 ohm load over a bandwidth of 1 Hz to 20kHz.
c) extremely low harmonic and intermodulation of distortion and low noise.

Dual–channel frequency spectrum analyzer:

A Hewlett–Packard 3562A Dynamic Signal Analyzer was used in acquiring the dynamic frequency response functions during the shake–tests. As described in detail in Ref. 7, this analyzer is a dual–channel fast–Fourier transform–based network, spectrum and waveform analyzer which provides analysis capabilities in both the time and frequency domains. The analyzer has a frequency range of from dc to 100 kHz, a measurement range of 150 dB and a dynamic range of 80 dB. The analyzer provides the basic excitation for the dynamic shakers in the alternate (user selectable) forms of random noise, burst random, sine chirp and burst chirp, as well as fixed sine and swept sine signals. The analyzer has a variety of built–in statistical dynamic analysis capabilities in the time, frequency and amplitude domains. For present purposes, the frequency response function analysis capability was used exclusively. To speed and simplify the documentation of results, direct control of plotters and disc drives is provided via an HP–IB bus. Anything displayed on the built–in CRT panel screen can be plotted or saved on floppy (3.5 in.) diskettes.

FM data tape recorder:

The HP 3562A frequency signal analyzer is of the standard two–channel variety and, consequently, it would not have been possible to utilize completely the availability of multiple (five) simultaneous response measurements from the accelerometers. Consequently, for the cantilevered configurations wherein the burst–chirp excitations were used, all the multiple response transients were recorded along with the common excitation force transient on FM video tape cassettes using an FM data tape recorder prior to input to the two–channel frequency analyzer (two channels at a time). A Kyowa RTP–650A Beta Format Video Cassette Instrumentation Data Recorder was used for this purpose (see Ref. 8). This recorder is a multi–function, multi–mode instrument which can record either in the FM mode or (with appropriate amplifier modules) in digital PCM mode for up to fourteen channels of input data. For the herein described tests the recorder was configured only for the FM mode as the necessary anti–aliasing filtering and digital conversions were performed within the two–channel frequency analyzer.

Strain gage instrumentation:

Strain gage type – Seventeen $0°-45°-90°$, single plane Micro–Measurements strain gage rosettes were applied to the tail cone. These rosettes have the following nominal specifications:

type:	CEA–13–125UR–350
resistance:	350 ohms
gage factor:	Leg 1: 2.120 ± 0.5%
	Leg 2: 2.145 ± 0.5%
	Leg 3: 2.120 ± 0.5%
minimal value:	2.13 ±1.5%
gage length:	0.125 in.

Rosette locations – The mounting locations of the rosettes were chosen to coincide with node locations in the finite element model of the tail cone. As stated above, these locations were only accurate to within ± 0.25 inches. The basis for this location accuracy estimate is is the accuracy obtainable in making actual physical measurements on the tail cone. All measurements had to be made using a tape measure on the outer skin. The principal measureable quantity was s, the arc length to the reference point of each rosette, as measured from the top (T) or (RH or LH) sides of the tail cone. Note that herein the following notation conventions are used:

T ≡ top, where $x = 0$ and $y = R$; RH ≡ right–hand side, where $x = -R$ and $y = 0$, and LH ≡ left–hand side where $x = R$ and $y = 0$. In the following table, the circumferential angle θ is defined by a conventional cylindrical coordinate system; z is taken along the longitudinal axis of the tail cone. This global cylindrical coordinate system is defined in Fig. 9 and the locations of all strain gages are given in the following table.

Table 2 — Strain gage locations and corresponding finite element nodes

	strain gage location			node location			
gage	s	θ	z	R	θ	z	FEM node no.
1	4.375,RH	195.0	12.1	17.133	195	12.124	365
2	4.375,RH	195.0	16.8	16.859	195	16.75	393
3	4.375,RH	195.0	21.4	16.586	195	21.375	418
4	11.375,T	126.8	1.6	17.741	123	1.75	166
5	11.375,T	127.0	3.9	17.608	123	4.0	224
6	11.375,T	127.3	6.2	17.475	123	6.25	266
7	0,T	90.0	1.6	17.741	90	1.75	129
8*	0,T	90.0	4.9	17.608	90	4.0	187
9*	0,T	90.0	6.2	17.475	90	6.25	244
10	4.13,T	105.2	31.6	15.977	105	31.625	555
11	3.88,T	104.5	54.2	14.65	105	54.125	663
12	16.76,T	345.8	145.9	9.221	346	146.0	1123
13*	30.63,T	311.0	88.5	12.619	315	88.5	891
14	30.63,T	330.0	71.6	13.614	315	71.625	807
15	9,T	60.0	1.6	17.741	60	1.75	135
16	9,T	60.0	4.0	17.608	60	4.0	193
17	9,T	60.0	6.2	17.475	60	6.25	246

* denotes an unusable (damaged) gage

The CEA series gages are universal general purpose strain gages suitable for both static and dynamic strain measurements. The Constantan grids are completely encapsulated in polyimide, with large, integral, copper coated terminals. The usable strain measurement range is ± 5%, or 50,000 micro inches per inch. All strain data were taken using the BLH Electronics Portable Model 1200B Digital Strain Indicator with a standard one quarter bridge circuit, as is typically described in Ref. 9. The strain is measured by relating a relative change in resistance, $\Delta R/R$, caused by strain within the gage through a calibrating constant, the gage factor, S_g, which is given by the manufacturer and for the gages used has a nominal value of 2.13. Thus, the strain, ϵ, is given by the following basic equation:

$$\epsilon = S_g \frac{\Delta R}{R}$$

Strain data quality

The quality of the measured strain data is affected by the following factors:

1. Gage location: The measurement of strain gage location on the tail cone is at best accurate to ± 0.25 inches, since the strain gage locations were measured on a conical surface using a flexible metal tape measure. Thus, the actual rosette locations were neither exactly in the center of a FEM element nor exactly at a FEM node. Within the accuracy of location measurement the gages thus ended up either occupying space shared by several contiguous elements or somewhere within (but not necessarily at the center of) one element. It should be noted that this is an issue with the assumed *location* of the measured strain and not with the measured strain reading itself.

2. Strain averaging: The measured strain is inherently an average over the finite area of the grid of each strain gage, rather than measurement of strain at a point. If there are steep strain gradients in the region being measured by the rosette, then these gradients will be inherently averaged. The small strain gages used on the tail cone were 0.125 inches in gage length by 0.060 inches in gage width. This size reduced the area over which the strains were measured, thereby reducing averaging errors in regions having steep strain gradients. Most of the rosettes were mounted near the cantilevered end of the tail cone, where the strains and strain gradients were expected to be greatest.

3. Wheatstone bridge nonlinearities: The strain measuring circuits used in the BLH Digital Strain Indicator exhibit nonlinearities of about 2% of the strain reading above measurements of 10,000 micro inches/inch. The strain measurements taken on the tail cone were no higher than 400 micro inches per inch. Thus nonlinear *circuit* effects were considered to be negligible.

4. Poisson's ratio mismatch, temperature change: Poisson's ratio mismatch and temperature changes in the test piece during testing can cause erroneous strain readings. However, the CEA series gages were temperature self–compensating and were designed to match the poisson's ratio of magnesium sheeting. All data were taken in a constant temperature environment.

5. Environmental noise: Electronic noise in the testing environment can cause erroneous strain readings. Although the test area is in an electronically noisy environment, it was free of any electronic noise accompanied with *audible* noise when data were taken.

6. Leadwire motion and length: The change in resistance of the leadwires, when moved, is picked up by the Wheatstone circuit as a perceived change in resistance of the foil gage. Leadwire motion was minimized but not eliminated since the loading of the tail cone did cause slight motion and vibration of the tail cone. The effects were minimized by waiting for one minute before data were taken so that the motion of the tail cone and loading eight platform would have time to stop vibrating. Leadwires were of equal length, cut as short as possible, and had a measured resistance of 0.2 ohms. This was negligible compared with the 500 ohms of resistance of each leg of each rosette.

2.6 Test Procedures

Calibration of accelerometers

All accelerometers were calibrated using the B & K Calibration Exciter described above. Each accelerometer was individually attached to the exciter and with the exciter operating the voltage output of the accelerometer was measured on a voltmeter. The expected voltage was calculated by multiplying the factory specified calibration in mV/g by the exciter acceleration. In all cases the two values of voltage were in agreement, indication proper acceleration functioning and calibration.

Calibration of load cell

The dynamic load cell was experimentally calibrated to determine if the output voltage per pound matched that of the manufacturer supplied specification sheet using the following procedure: A carefully weighed test mass (7.95 kg) was suspended adjacent to the shaker. A narrow rod was used to connect the shaker to the load cell, with the load cell then connected to the test mass. One of the accelerometers (S/N 16260) was attached to the opposite end of the test mass. The shaker was used to apply a force to the load cell which, in turn, would accelerate the test mass. The acceleration of the test mass was measured by

the accelerometer, and the applied load measured by the load cell. The output voltages of the accelerometer and load cell were directed to a bank of amplifiers, and then to the HP frequency analyzer in a manner similar to that used in the actual shake test. Knowing the mass of the test mass and the calibrated value of the accelerometer (as obtained by a separate calibration tool) the calibration constant of the load cell could be calculated. The frequency analyzer was also used to supply the excitation voltage to the shaker, using its burst chirp source setting at an amplitude of 1 volt and a frequency range of 10 to 110 Hz. Data from this test was also recorded on a FM data recorder at a tape speed of 2.4 cm/sec.

The frequency analyzer generated a transfer function of accelerometer output vs load cell input. It was found to have a steady value of -24.8 dB in the frequency range tested. This magnitude is equivalent to (acceleration/ force) times the ratio of calibration factors, or the inverse of the test mass times the ratio of the calibration factors. After substituting the known mass and accelerometer calibration factor, a load cell calibration factor of 108.8 mV/lb was found. The value given in the specification sheet is 104.57 mV/lb, showing that the load cell was therefore functioning normally.

Calibration of the FM data recorder

During calibrations of the instrumentation and the actual data acquistion during the shake–tests, all data were recorded on an FM data recorder. Therefore, if was necessary to check the calibration of this device. The data recorder is a 14 channel unit, but only a maximum of 6 channels were used at one time so only the first 6 channels were checked. All testing was carried out using a tape speed setting of 4.8 cm/sec and at frequencies of up to 100 Hz. The calibration check was therefore conducted under these conditions.

The HP frequency analyzer was used to generate a sinusoid signal of frequency 100 Hz and amplitude .200 V. This signal was directed into each of the first 6 channels and recorded at a variety of range settings. Range settings consist of voltage amplitudes which are expected by the data recorder. Each channel's range can be either set manually or automatically through data sampling by the recorder. When recording data on a certain channel, the voltage is scaled such that an input voltage equal to the range setting is recorded at a value of 5 volts, or:

$$V_{in} = V_{rec} \times (\text{Range}) / 5.0$$

It was therefore necessary to check the recording capability at a variety of range settings.

Shake–test procedure

The above described MB Dynamics model 50A electrodynamic shaker used was for all shake–tests. In the case of the cantilevered configurations the shaker was used either horizontally or obliquely (see Figs. 7 and 8 for the respective stinger attachments to the tail cone end). Accelerometers were positioned at intervals along the length of the tail cone side stiffeners (see Fig. 6); the accelerometers could thus measure accelerations in the vertical and lateral directions. As shown in Fig. 10, the HP dual–channel frequency analyzer was used not only to drive the shaker but to digitize the response data, and finally to spectrum analyze and record the digitized data. [Note that the general operational characteristics of the dual–channel frequency spectrum analyzer are given in an above section.] All load cell and accelerometer signals were amplified by the PCB model 483A08 multi–channel rack power unit and then input either to the FM data acquisition tape recorder and/or directly to the HP dual–channel frequency spectrum analyzer, as appropriate.

Cantilevered tail cone configurations – For all cantilevered tests the procedure for acquiring the data was first to define runs wherein a selected set of five accelerometer responses were recorded together with the force measurements from the load cell. Also, for these cantilevered configurations the high sensitivity accelerometers were used for the vertical acceleration sensing and for the lateral acceleration sensing near the base (hard–back end) portions of the tail cone where a much smaller response level was expected. All cantileverd configurations were excited using the burst chirp mode of input excitation signal to the shaker. For these burst chirp excitations the frequency range was from approximately 1 Hz to a maximum of 100Hz. Nine runs were required to measure the responses at all the selected accelerometer locations. This procedure thereby allowed for redundant measurements during each run for monitoring run consistency. Within any one run the load cell and accelerometer response at the tail cone (load application) end were also input to the HP dual–channel frequency spectrum analyzer to control the convergence of the statistical sampling algorithms built into the analyzer. For these runs the analyzer was set to provide ten averages (i.e., ten burst chirp excitations) which typically required a total duration of approximately two minutes per run.

For all data recorded with the FM data tape recorder the tape speed was selected and maintained at the 4.8 cm/sec setting. Later, after the actual shake–testing was completed, the FM recorder was then used to provide transient inputs to the HP dual–channel frequency spectrum analyzer to post–process the separate frequency response functions for each of the accelerometer locations (relative to the same force excitation). One advantage of this method of data acquisition is that it reduced the actual run time in the shake–testing operations. Also, although not utilized in this study, this technique should have the potential for maximizing the accuracy of measuring the response functions of *different accelerometer locations relative to each other* due to the same excitation. It is conjectured that in the future this type of frequency response function information will be needed for measuring higher level dynamic phenomena in the structure. Without the simultaneous recording of the several channels such relative frequency response functions would not be possible.

Simulated free–free configuration – The test procedure for the simulated free–free configuration had to be modified when it was found that the burst chirp mode of excitation did not produce consistent results and the inherently more accurate (but more time–consuming) sine sweep mode of excitation would be required. Unfortunately, because the swept sine mode of excitation does not have an inherently coherent "window" as does the burst chirp, it was not possible to run the FM data tape recorded results back into the HP to post–process the results. Therefore, all frequency response functions for this configuration had to be obtained separately for each selected accelerometer location. In all these cases the high sensitivity accelerometer was used throughout. For these cases the data was recorded directly on floppy diskettes in the form of digitized frequency response functions.

Data reduction of the experimental frequency response functions

As the primary goal of the present study was the correlation of test results with FEM analytical results, the reduction of the experimental results required an efficient way of being able to plot the experiemental results on the same graphs with the FEM predictions. Although the HP analyzer can generate quite adequate graphical plots of the experimental results separately, the digitized forms of these frequency response functions as available on floppy diskettes are not in a format compatible with the DOS ASCII results available from the FEM analysis. In order to make the digitized experimental results compatible with the FEM analytical results (so that both results could be merged in a graphics program), they

had to be post–processed further with a conversion to DOS ASCII format. This conversion was accomplished with special PC–based software provided by the Hewlett–Packard Company (Ref. 10).

3.0 FINITE ELEMENT MODELING AND CORRELATION PLAN

3.1 Basic Element Modeling

As described also in the previous chapter, the S–55 tail cone is a metal semimonocoque structure whose frames are made of Alclad 2024 and whose skins are made of magnesium. Its construction is generally typical of helicopters of moderate size. Although the donation of the tail cone to the RPI Aircraft Component Shake–Test Facility by its manufacturer, Sikorsky Division of United Technologies represents a valuable research asset, of equal importance to this research is the retrieval from the archives of the manufacturing engineering prints with the much–needed dimensions and material specifications. These shop prints were used to construct the finite element modeling described generally herein and in considerably more detail in Ref. 11.

The tail cone is constructed by wrapping magnesium skins around Alclad frame rings. All sheets of magnesium were riveted to the Alclad frames. Doublers and stiffeners were riveted to the magnesium skins. In order to obtain an efficient modeling of the tail cone, simplifying assumptions had to be made wherever two sheets of material were riveted together. Additionally, in order to keep the degrees of freedom within the proper limit, not all frames were modeled completely with shell elements, but instead were modeled either partially with shell elements and/or with three dimensional beam elements.

The tail cone geometry was reduced to finite element nodes whose location were determined by frame locations, frame rings, skin rings, and stiffeners. There are nine physical frame rings positioned along the length of the tail cone. On each frame ring, finite element nodes were placed at fifteen degree intervals along the circumference, except where additional nodes were needed to model special areas of the tail cone. These special areas are the bottom and side external stiffeners, the large doubler, and the external stiffeners at the $\theta = 0^{\circ}$, 180°, 255°, 270° and 285° degree positions around the circumference. Note that $\theta = 0$ corresponds to the starboard lateral direction (+ x direction). Additionally, there are two internal stiffeners with variable circumferential locations starting at approximately 225° and 315°, respectively, at frame 7.5 and transitioning to approximately 265° and 275°, respectively, at frame 94.0 where they terminate. These stiffeners consist of channel sections and were modeled as equivalently increased skin thicknesses for the shell elements at these locations.

Skins:

The "skins" or sheets of magnesium which are wrapped around the Alclad frames were modeled with the following assumptions with respect to material properties:

(1) At all frame stations where there are shell elements representing the sum of the thicknesses for magnesium skins riveted to Alclad frames, such shell elements were modeled using Alclad material properties.

(2) Between the 197.875 and 212.856 frames, the skins were modeled with double thickness of Alclad, rather than magnesium. The end of the tail cone was double wrapped and the material properties of Alclad were used since the properties were not known and the assumption was made that these skins are reinforcements for the end of the tail cone.

Doublers:

In between frame 0 and frame 7.5, exist one larger doubler and one smaller doubler. Both of these doublers were modeled as shell elements with the sum of the thickness of the magnesium skin and the doubler, using the magnesium skin material properties.

Frames:

The detailed modeling assumptions used to model the frames are as follows:

Frame 0.0 – This frame contains the bolt holes for attaching the tail cone to the main portion of the helicopter frame. The magnesium skin is riveted to the frame. In the finite element model, the thickness of the magnesium skin and the thickness of the Alclad frame were modeled as a shell element with the sum of both thicknesses but the material properties of the magnesium skins. The remaining flange of the Alclad frame was modeled with shell elements using the Alclad material properties. The rivet strips were modeled as shell elements with the sum of the flange and rivet strip thicknesses. The bolt hole tabs were modeled as shell elements with the sum of the flange and bolt hole tab thicknesses.

Frame 7.5 – At this frame, two magnesium skins overlap each other and are riveted to the frame ring. This overlapping region was modeled with shell elements that have the thickness of the sum of the two magnesium skins and the Alclad frame. The material properties used for this overlapping region are the material properties of the Alclad frame. The remaining two sections of the frame ring were modeled as Alclad shell elements.

Frame 26.0 At this frame, an Alclad frame is riveted to the magnesium skin wrapped around the tail cone. The overlapping region was modeled with shell elements whose thickness equals the thickness of the magnesium skin and the thickness of the Alclad flange. The material properties of Alclad was used for these shell elements. The remaining two sections of the frame ring were modeled as Alclad shell elements.

Frame 60.375 – At this frame, an Alclad frame is riveted to the magnesium skin wrapped around the tail cone. The overlapping region was modeled with shell elements whose thickness equals the thickness of the magnesium skin and the thickness of the Alclad flange. The material properties of Alclad was used for these shell elements. The remaining two sections of the frame ring were modeled as Alclad shell elements.

Frame 94.0 – At this frame, an Alclad frame is riveted to the magnesium skin wrapped around the tail cone. The overlapping region was modeled with shell elements whose thickness equals the thickness of the magnesium skin and the thickness of the Alclad flange. The material properties of magnesium was used for these shell elements. The remaining two sections of the frame ring were modeled as Alclad shell elements.

Frame 129.0 – At this frame, two magnesium skins overlap each other and are riveted to the frame ring. The overlapping region was modeled with shell elements that have the thickness of the sum of the two magnesium skins and the Alclad frame. The material properties used for this overlapping region are the material properties of the magnesium skins. The remaining two sections of the frame ring were modeled as Alclad unsymmetric beam elements.

Frame 163.0 – At this frame, an Alclad frame is riveted to the magnesium skin wrapped around the tail cone. The overlapping region was modeled with shell elements whose thickness equals the thickness of the magnesium skin and the thickness of the Alclad flange. The material properties of magnesium was used for these shell elements. The remaining two sections of the frame ring were modeled as Alclad unsymmetric beam elements.

Frame 197.0 – At this frame, an Alclad frame is riveted to the magnesium skin wrapped around the tail cone. The overlapping region was modeled with shell elements whose thickness equals the thickness of the magnesium skin and the thickness of the Alclad flange. The material properties of Alclad was used for these shell elements. The remaining two sections of the frame ring were modeled as Alclad unsymmetric beam elements.

Frame 212.0 – At this frame, which is the end of tail cone, a thick magnesium casting is riveted to the magnesium skins. An additional magnesium skin overlaps the top 180 degrees of the tail cone so that there are two magnesium skins overlapping the magnesium casting. The top portion of the skin of the tail cone where there are two magnesium skins, is modeled as double thickness magnesium shell elements. The magnesium casting is modeled as a unsymmetric beam element with magnesium casting material properties.

Stiffeners:

The tail cone is stiffened with sets of both internal and external longitudinally oriented stiffeners. Two internal stiffeners are located in the lower portions of the tail cone between frames 7.5 and 94.0 with variable circumferential location, joining each other at the 270° (bottom) position at frame 94.0 . External stiffeners exist at the $\theta = 0°$, 180°, 255° , 270° and 285° circumferential locations. Those at 0° and 180° constitute the "side " stiffeners and extend the entire length of the tail cone. The stiffener located at the 270° position extend from the frame 0 to a point aft of frame 129.0 . This stiffener constitutes the bottom "keel" of the tail cone. The external stiffeners located at the $\theta = 255°$ and 285° locations extend from frame 94.0 to the end of the tail cone (frame 212.0). All of the external stiffeners were modeled using unsymmetric three–dimensional beam elements with Alclad material properties.

A detailed description of all the selected finite elements and the connectivity is beyond the intent of this report. Correspondingly, all elements (by type and appropriate properties) and node numbers used in the model are contained in Ref. 11.

3.2 Element Connectivity

The S–55 tail cone, by virtue of its basically symmetrical design (circular frames, skins, doublers and stiffeners), lent itself to a straightforward element connectivity scheme. Because of the regular locations of the stiffeners at circumferencial positions of 0°, 180°, 255°, 285° and 270°, the basic guiding strategy was to place nodes every 15 degrees around the circumferences of each of the frames. The nodes were numbered in ascending order starting at the top of the tail cone at the y–axis and progressing initially in the y direction (to starboard). This numbering scheme was also followed for the elements. Generally, the numbering of the nodes and elements also proceeds in ascending order going from the base end (hard–back attachment end) to the free (aft) end. A detailed description of the element connectivity is beyond the scope of this report, but is available in Ref. 11.

3.3 Material Property Determination

Determination of end casing material:

Although the material specifications given in the shop prints were mainly quite detailed some deficiencies were encounterd. One deficiency was the material specification for the end casing between fuselage stations 197.0 and 212.0 . Accurate determination of it's composition was desired so that proper material properties could be used in the finite element model. To accomplish this, a scanning microscope analysis was carried out by the RPI Materials Research Center. A small shaving was carved out of the end casing using a deburring too. The surface had to be gouged out below a surface layer of what was found to be aluminum. A shaving of the primary material was then delivered for analysis. A JEOL JSM–840 high magnification scanning electron microscope was used examine an area of 100 microns by 100 microns on the shaving, which was set on a carbon background to provide a neutral background. From Fig. 11 it was deduced that the primary component is magnesium, with trace amounts of zinc and aluminum.

Summary of material properties:

From the engineering prints and the results of the scanning microscope analysis all the fabrication materials were thereby identified. Much effort was then made to ascertain the proper stiffness and density properties for each material used in the tail cone. A summary of the material properties subsequently used for the shell and beam elements are the following:

Material set no. 1: (Alclad frames – Ref. 12)

modulus of elasticity, E: 10.6×10^6 lb/in^2
Poisson's ratio, ν: 0.33

density, ρ: 0.10035 lb$_w$/in^3, (2.588×10^{-4}lb.sec^2/in^4)

Material set no. 2: (magnesium skins /alloy QQ–M–44, Condition H – Refs. 13 & 14)

modulus of elasticity, E: 6.5×10^6 lb/in^2
Poisson's ratio, ν: 0.35

density, ρ: 0.064 lb$_w$/in^3, (1.656×10^{-4} lb.sec^2/in^4)

Material set no. 3: (magnesium casting)

modulus of elasticity, E: 6.5×10^6 lb/in^2
Poisson's ratio, ν: 0.35

density, ρ: 0.064 lb$_w$/in^3, (1.656×10^{-4} lb.sec^2/in^4)

Material set no. 4: (steel, drive shaft – Ref. 15)

modulus of elasticity, E: 29.0×10^6 lb/in^2
Poisson's ratio, ν: 0.33

density, ρ: 0.286 lb$_w$/in^3, (7.402×10^{-4} lb.sec^2/in^4)

Material set no. 5: (rubber surrounding drive shaft bearings)

[Properties considered to be indeterminant.]

Material set number 6: (polyethylene filler in 0°, 180°, 270°, 255°, and 285° stiffeners – Ref. 16)

modulus of elasticity, E: 110,200 lb/in^2

Poisson's ratio, ν: (neglected)

density, ρ: 0.03468 lb_w/in^3, (0.8975×10^{-4} $lb.sec^2/in^4$)

3.4 Mass Modeling

In addition to the primary correlational results, i.e., static strains and frequency response functions a fundamental correlational result bearing on all the dynamic results is the modeling of the correct weight. This task was especially crucial as it directly related to achieving a proper mass modeling and was not straightforward because of the detailed investigation of many parts called out on the shop prints. Additions had to be made to the initial mass modeling to account for a total weight discrepancy of more than 20 pounds. The tail cone was initially modeled in a basic skeletal way wherein the structure consisted solely of only elastic members: skins, doublers, frames and stiffeners. Additional attention had to paid to the details to identify mass which would increase the finite element predicted weight of the tail cone to the measured value of 130 lb_w. The following additional (nonstructural) details were gleaned from the engineering prints.

1. drive shaft bearing weight of 1 lb each, 7 bearings along the drive shaft
2. polyethylene filler in 0°, 180°, 255°, 285° and 270° stiffeners
3. twenty (20) accelerometer blocks and frame 212.856 driving point bar
4. steel cable running inside length of tail cone
5. double panels of Alclad between frames 197.000 and 212.856
6. mass of bolts used on drive shaft brackets and magnesium casting at frame 212.856
7. magnesium casting at frame 212.856
8. mass of rivets (approximation)
9. frame 7.5 enlarged to conform with specifications of the shop printst
10. cross beams to frames 163.5, 197.875, and 212.856.
11. double thickness for frame reinforcements on all frames in the tail cone
12. double thickness for drive shaft brackets to account for weight of bracket riveted to tail cone frames

With the inclusion of these details the calculated weight of the tail cone came to 136 lb_w, as compared with the value of 130 lb_w measured before mounting the tail cone to the hard–back structure.

3.5 Suspension Configurations

The boundary conditions imposed on the model to approximate the cantilevered and free–free suspension conditions were the following:

Cantilevered: Frame 0, or nodes 1 throught 128, were constrained by specifying all six components of displacement of those nodes to be zero.

Free–free: Six springs were used to model the free–free condition. The spring configuration consisted of x– and y– direction translational springs attached to the drive shaft bearing support bracket points atop frames 60.375 and 129.0 (finite elements nodes of 3005 and 3009, respectively). In addition, a translational spring in the z direction and a rotational spring about the z–axis were both attached to node 8029. A spring constant of 0.001 lb/in was selected for all translational springs and a constant of 0.001 in–lb/rad was selected for the rotational spring.

3.6 Correlation Plan

The correlation study was to be performed by first matching measured strains produced by static load conditions. This first step was intended to validate the stiffness model before correlations with the dynamic (frequency response function) properties were attempted. For the static correlation, the predicted static strains were calculated indirectly from the finite element model displacements and calculated stresses, and from standard stress–strain relationships for shell elements. The results of comparing the experimentally determined strains with the calculated strains are shown in graphical form in Section 4.3.

For the second phase of the correlation study measured frequency response functions produced by shaker excitation were to be compared to those respective quantities predicted by the COSMOS/M finite element analysis. For dynamic correlation results, i.e., the comparison of the experimentally determined frequency response functions the finite element predicted frequency response functions are shown in Section 6.4. Also, an additional check on the mass modeling was to be achieved by comparing the calculated mass (and weight) with that determined by actually weighing the tail cone.

It is to be expected that the present study is the first step in achieving a truly accurate modeling of this tail cone. In further studies, the modeling can and should be improved from the results of this comparison and with bringing to bear new analytical techniques and even more extensive frequency response shake–testing. More detailed recommendations on this topic are contained in a later chapter.

4.0 STATIC STRAIN CHARACTERISTICS

4.1 Basic Considerations

Gage installation

The installation of strain gages for the purposes of this study were in fact limited by a number of operational constraints. First, the number of gages which could be used were limited by cost, time and the availability of support instrumentation. Although a new data logging system was obtained, its performance in the RPI Airframe Shake–Test Facility was deemed to be unsatisfactory and a more primative but also more reliable (single channel) strain gage instrumentation was subsequently used. A second constraint which impacted on this study was the inablility to strain gage both inner and outer surfaces of the tail cone skin. The first reason for not strain gaging the inner surface was that most of the interior of the tail cone presents insufficient room for human occupation, especially to enable one to go through the tedious process of applying strain gages. Second, once the tail cone was installed on the hard–back structure it was not removed until much later in the program in order to obtain the free–free dynamic tests. The installation of the tail cone on the hard–back structure is a labor intensive chore and the decision was made to not disturb the structure unnecessarily. The result is that, as described in an earlier chapter, only the outside of the tail cone skin was instrumented. This instrumentation consisted of seventeen (17) three–leg strain gage rosettes; this number of rosettes was selected in order to obtain as complete a strain description as possible. The rosette locations are given in Table 2 and as approximately shown in Fig. 12.

Loading conditions

The tail cone was loaded with a horizontal bending load applied at the free end, in the positive x direction to impart the same type of loading that would occur during typical operation of the S–55 helicopter, i.e., that due to the anti–main rotor torque tail rotor thrust loading. The strain gages were loaded individually with end loads ranging from 0 to 300 pounds force, in increments of 50 pounds. This loading schedule was applied identically for each individual leg of each rosette, three separate times each. The average of these three data sets was then used for comparison with the finite element predicted strains. Fig. 5 illustrates the method and direction of loading the tail cone.

Static test correlation variables

In order to obtain *strain* predictions from the finite element model, the measured strain results from the rosettes first had to be reduced to the local element coordinates of the output from the COSMOS/M finite element analysis. This analysis, however, gives only local *stress* calculations at the nodes. Consequently, these stresses must then be transformed to strain with Hooke's stress–strain transformation equations. This procedure affords a comparison between the experimental and finite element *strains* without having to introduce the modulus of elasticity (to transform the experimental strains to stresses) into the experimental data reduction. A description of the necessary transformation equations is given in the next section.

4.2 Transformation equations relating rosette strain to local element displacements

The finite element modeling of the ring frames and skins of the tail cone was accomplished, for the most part, using triangular and quadrilateral shell elements, i.e., COSMOS/M SHELL3 and SHELL4 elements, respectively. Additionally, the longitudinal stiffeners on the tail cone are modeled using unsymmetric and symmetric three–dimensional beam elements, i.e., COSMOS/M BEAM3D–UNSYMMETRIC and BEAM3D-SYMMETRIC elements, respectively. COSMOS/M will allow specification of stress in either local or global coordinates at the nodes. Since all rosettes were mounted directly on the skins of the tail cone, and not on any stiffeners, the only finite element models that need to be considered herein are the SHELL3 and SHELL4 elements. Descriptions of the local coordinates for SHELL3 and SHELL4 elements follow.

The local directions of all rosettes are labeled by the numbers 1, 2, and 3. These local rosette strains must be transformed from the 1, 2, 3 rosette directions to normal and shear strains in the SHELL3 and SHELL4 element local x' and y' directions. Since the modeling of the tail cone is based on the presence of node rings, as shown in Fig. 12, the element numbering scheme was taken in a circumferential direction around these node rings. The numbering scheme at each node ring started at the top of the ring ($x = 0$, $y = R$) and proceeded initially in the (x) direction (in the starboard direction). As a result of this numbering scheme the shell element (x') direction is defined by a line that connects node $a^{(i)}$ to node $a^{(i+1)}$. In other words, the (x') direction is tangent to the node rings. [Note

that this direction is therefore in the negative (s) direction, as defined in Fig. 9.] The (x′) direction is tangential to the node rings and is herein referred to as the *circumferential direction.* Similarly, since the shell element local (y′) direction is defined as perpendicular to the shell element (x′) direction, the (y′) direction is perpendicular to the node rings. The local (y′) direction is along the length of the skin of the tail cone in the aft direction (i.e., along a generatrix of the tail cone's conical surface, positive in the direction toward the apex). This direction is herein referred to as the *longitudinal direction.* The transformation equations relating the measured strains in the rosette 1, 2, and 3 directions, ϵ_1, ϵ_2, and ϵ_3 , respectively, to the ϵ_x and ϵ_y normal strains (as calculated in the local SHELL3 and SHELL4 element circumferential (x′) and longitudinal (y′) directions, respectively), and the shearing strain, γ_{xy}, are given in matrix form (see Ref. 9) as follows:

$$\begin{Bmatrix} \epsilon_1 \\ \epsilon_2 \\ \epsilon_3 \end{Bmatrix} = \begin{bmatrix} \cos^2\theta_1 & \sin^2\theta_1 & \sin\theta_1\cos\theta_1 \\ \cos^2\theta_2 & \sin^2\theta_2 & \sin\theta_2\cos\theta_2 \\ \cos^2\theta_3 & \sin^2\theta_3 & \sin\theta_3\cos\theta_3 \end{bmatrix} \begin{Bmatrix} \epsilon_x \\ \epsilon_y \\ \gamma_{xy} \end{Bmatrix}$$

Diagrams of the specific mounting orientations of the various rosettes are given in Figs. 13a thru 13d. The positive x′ direction follows the direction of the numbering of the ring nodes. Nodes are numbered starting from the y′–axis going towards the x′–axis. The positive (y′) direction is perpendicular to the x′–axis and points in the direction of the next node ring. The shearing strain occurs in the (x′–y′) plane and positive shearing strain is denoted as positive when the angle between the x′– and y′– axes of the element decrease. Note that the equations relating the local rosette strain directions to the finite element local coordinate system strains are given, as appropriate in each figure. Rosettes 1, 2, 3, 10, and 11 were mounted as shown in Fig. 13a. Rosettes 4, 5, 6, 7, and 9 were mounted as shown in Fig. 13b. Rosettes 12, 13, and 14 were mounted as shown in Fig. 13c. And, finally, rosettes 15, 16, and 17 were mounted as shown in Fig. 13d.

4.3 Static Tests and Summary of Results

There were seventeen strain gage rosettes mounted on the tail cone and fourteen yielded acceptable experimental results. The finite element predicted and experimentally determined strains at representative rosette location are compared in Figs. 14a–j. In all of these figures a certain degree of averaging is inherent with both the experimental results and analytical predictions. The reasons for averaging in each of these cases is developed in sections to follow. The locations of the rosettes were determined on the basis of providing information "clusters" which would provide results representing different types of modeling assumptions. Seven basically different regions were selected. The unique results obtained in each of these regions are discussed in turn. In the discussion of correlation of the strain results, it is important to keep the following issues in mind:

Experimental strain data averaging and quality

For each rosette the tail cone was loaded three separate times and the results for each leg were averaged and plotted as shown in the correlation figures, Figs. 14a thru 16j. To determine the linearity of the experimental data, a curve fit was applied to the strain data points and a correlation coefficient was calculated. Out of the fourteen rosettes actually used to measure strain, only two rosette legs out of the total of forty–two had correlation coefficients below 0.9. Upon inspection these two legs were found to be measuring strains within the noise band of the measuring equipment. The noise band on the measuring equipment includes any strain measured within 0 to 5 microstrains. The accuracy of the experimental data is taken to be within ± 5%. This level of accuracy is based on prior experiments with this strain measuring equipment wherein the actual displacements and strains on a test article were known and compared to the strains measured by strain gages. The results from rosettes numbers 8, 9 and 12 were neglected because of the grossly unrealistic values produced.

4.4 Finite Element Analysis Results

Prediction of static stresses

The predicted stresses in any one FEM element are specified in Ref. 1 to be given in the center of the each element and at each node of the element. The stresses at each node and center of element were specified in the finite element static analysis to be given in local element coordinates. In order to compare experimental strains against finite element predicted strains, the finite element local predicted stresses at each node were first transformed into local element strain by the standard stress–strain relationships given below:

$$\epsilon_x = (\sigma_x - \nu \sigma_y)/E$$
$$\epsilon_y = (\sigma_y - \nu \sigma_x)/E$$
$$\gamma_{xy} = \tau_{xy}/G$$

Material properties used to transform stress to strain

Once all analytical stresses were recorded, the stresses were transformed to strains using the modulus of elasticity and Poisson's ratio of the magnesium skins of the finite element model. The exception was rosette 6, wherein elements 286, 321, and 322 were modeled with Alclad properties. All data collected from the static analysis and their resulting transformations are given in Ref. 17. The material properties for magnesium used with the above equation for stress to strain conversion are as follows:

$$E = 6.5 \times 10^6, \ \nu = 0.35, \ G = 2.4 \times 10^6$$

Averaged element strain predictions versus strains at nodes

The finite element results presented were calculated in 3 steps:

1. Each node corresponding to a rosette location is inherently a member to contibuting to the definitions of at least three and in many cases five elements. Within any

element COSMOS/M calculates the stresses at all three or four nodes corresponding to that element. This means that for a node which is connected to four elements, there will be four separate stress calculations at that *node*. In addition, there is one calculation for stress at (typically, the center of) each *element* . Step one therefore consists of collecting the COSMOS/M stress calculations for all elements that are connected to each node corresponding to a rosette mounting location.

2. The stresses are transformed into finite element axis orientated strains with the strain transformation equations given above.

3. For each node, n, corresponding to a rosette measurement location there are at least three to four predictions for the strain at that particular node (resulting from all the contiguous elements). Thus, for node n, the three to four strain predictions are averaged together as one number for the predicted strain at that node location. This is the basis of the "averaged" strains which are presented in Figs. 14a thru 14j.

Finite element predicted stress data quality

The only non–modeling related factor which has some bearing on the correlation between the experimental and analytical strains is of course, whether or not the experimental and analytical locations chosen are accurately located relative to each other. In this study the finite element nodes picked for correlation with the rosette locations were within 0.3 inches of their respective mounted rosettes. Where there were steep strain gradients the physical locations of the rosettes and the finite element node locations could be critical to the correlation process. The steepest strain gradients typically occurred at the cantilevered (inboard) end of the tail cone, corresponding to rosettes 1 thru 7 and 15 thru 17. Although the actual locations of most gages were chosen to be as close as possible to finite element node locations in some cases rosettes were positioned inconsistently with the finite element nodes, due either to modifications and/or corrections to the finite element model which occurred after the rosettes were applied, or to errors in measurement. In particular, rosettes 4, 5, 6, 15, 16 and 17 were mounted in locations which were circumferentially displaced by approximately 1.5 in. from their designated finite element node locations. The mismatch of these rosette locations with the nodal locations would be expected to be a source of error between the analytical and experimentally determined strains.

4.5 Envelope of Uncertainty for Experimental Data and Finite Element Strain Predictions

In comparing the experimental and COSMOS/M predicted strains, we need to consider the envelope of uncertainty for the measured data. The finite element model predicted strains are compared with the measured strains and each set of data is recorded with a set of assumptions about it's ability to represent reality accurately. For experimental data, we shall adopt a term, called the *experimental envelope* which serves the purpose of telling us "how close is close" when evaluating the results.

Experimental data:

For the experimental data the following considerations must be made:

1. The rosettes were mounted only approximately at the corresponding node location on the model of the helicopter tail cone.

2. The rosettes inherently sense an average strain over a finite area, which becomes a source of strain approximation in areas of high strain gradients, such as near the cantilevered end of the tail cone.

3. The experimental strain data provided in the figures are averages of results obtained from three seperate loadings of the tail cone, and in some cases the three seperate strain data sets varied by as much as 30% from one load schedule to the next.

Each of the above considerations will contribute in some measure to the size of the experimental envelope of uncertainty. Thus, it appears reasonable that if the predicted strains fall within 20 to 30% of the experimental strains, the comparison is considered to be very good in that region and to be modeled accurately. The envelope of experimental uncertainty shall, in some cases hereinafter, be referred to simply as the "experimental envelope".

Analytical results:

For the finite element model there are assumptions made that are not identical to the loading conditions actually performed in the laboratory. These assumptions are as follows:

1. The cantilever mount boundary condition at the inboard end, as implemented in the finite element model, has all degrees of freedom on frame 0.0 constrained to zero rotation and displacement. In the actual test piece the tail cone is actually mounted to the hard back adapter ring with fourteen bolt holes . The actual test piece may have some strain relief from not being perfectly attached for zero rotation and displacement.

2. The selected material properties are "handbook" values, which can reasonably expected to be only average values for the material.

3. The riveted locations were modeled in all cases as a single sheet of material with the thickness of all the pieces of sheet metal riveted together. The rivets actually provide for some strain relief that are beyond the present modeling capabilities of the finite element analysis.

4. For the averaged finite element model results for nodal predicted stress (or strain) at the node, the "predicted" nodal strains are actually averages of four separate predictions. The separate predictions result from each of the elements for which that node is a member. What this means is that for the correlation, if the element was attached to four elements and two of these were very stiff and the other two were less stiff, then the "*averaged* predicted nodal strain" results presented in the figures would show the predicted strain to fall somewhere in the middle of the two extremes. In most cases the predicted results plotted for each individual element situated around the selected node point strain fell quite close to the experimental strains. But in several cases, especially in the high strain gradient regions, two elements to the left of the selected node stretched more than the next two elements to the right of that node. Thus, the "averaged predicted nodal strain" line was found to be collinear with the experimental line. Additionally, in another case, the predicted strain for the four elements attached to that node exhibited slopes which are all progressively steeper than the experimentally determined slopes. When all four of these predictions at the node are averaged, then in some cases it appears that the "averaged predicted nodal strain" is considerably "stiffer" or "more pliable" than the experimental strain.

Strain regions and physical characteristics of each region

As was stated earlier, The rosettes were clustered into general regions of the tailcone for the purpose of each cluster representing different types of modeling assumptions. Seven basically different regions can be defined:

Region 1: Rosettes 1, 2, and 3, are located on the port side of the tail cone in the third quadrant ($180^\circ < \theta \leq 270^\circ$) between frames 7.5 and 26.0. In this region there are moderate strain gradients, especially in the longitudinal direction, since the general location of this region is near the forward end of the tail cone where the cantilevered boundary condition is invoked.

Region 2: Rosettes 4, 5, and 6 are located on the port side of the tail cone in the second quadrant ($90^\circ < \theta \leq 180^\circ$) between frames 0.0 and 7.5. In this region, very high strain gradients arise again because of the proximity of the cantilevered boundard conditions, and because of the presence of riveted strips for the frames located on either side of the rosettes.

Region 3: Rosettes 7, 8 and 9 are located exactly on the top of the tailcone ($\theta = 90^\circ$). In this region, on the top of the tailcone, the only normal strains which would result would be those longitudinal strains due to vertical bending of the tail cone. Circumferential normal strains experienced in that area would be expected to be small, and shear strains would be attributable to the lateral load at the aft end of the tail cone.

Region 4: Rosettes 10 and 11 are located between frames 26.0 and 60.375 again in the second quadrant. In this region, the strain area is confined to a single thickness skin and relatively removed from abrupt built–up areas and can thus be characterized as having only moderate strain gradients.

Region 5: Rosettes 13 and 14 are located on the starboard side of the tailcone between frames 94.75 and 60.375 in the fourth quadrant ($270^\circ < \theta \leq 360^\circ$). Although the loading level would be expected to be different, this region would be expected to have the same gradient characteristics as Region 6.

Region 6: Rosette 12 is located on the starboard side betwen frames 163.5 and 129.125. This area should also be characterized as having only moderate strain gradients. The loading type would be similar to Region 5, but the loading level would be expected to be lower.

Region 7: Rosettes 15, 16 and 17 are located on the starboard side of the tail cone in the first quadrant ($0^\circ < \theta < 90^\circ$) between frames 0 and 7.5. This area is charactertized by very high strain gradients and riveted strips for the frames located on either side of the rosettes and would be expected to have similar characteristics as Region 2.

4.6 Discussion of Correlation Results

The experimentally measured strains and analytical predictions comprising the strain correlation results are compared in Figures 14a thru 14j for representative rosette locations. Each of the figures consists of the three components of strain results: circumferential and longitudinal normal strains, ϵ_x and ϵ_y, respectively, and the complementary shear strain, γ_{xy}. While not provided herein, the detailed slopes for each experimental and analytical data line were calculated and compared in Ref. 17. In this reference detailed compilations of the percent differences between the analytical and the experimental data, have been made and tabulated. Much has been learned from the static strain study and a complete description of the findings is beyond the scope of this report. The material to follow is an abridgement of the material given in Ref. 17. The discussion to follow will deal in turn with the normal and shear strain results.

Normal strain results

After the results are reviewed with a perspective to each of the regions discussed above, some patterns emerge. As shown in Figures 14a, thru 14e, representative results for Regions 1, 4, and 6 (rosettes 1 and 2, 10 and 11, and 12, respectively) show the finite element model to approximate the experimentally determined results quite accurately. Figure 14f, which presents the only results representative of Region 5 (rosette 14), shows the analytical stiffness properties to be higher than those experimentally determined. Regions 2, (rosettes 4, 5 and 6) and Region 7 (rosettes 15, 16 and 17) were found to tell exactly the same story. As represented by Region 2, Figures 14g, 14h and 14i show that

the model is not accurately assessing the stiffness properties in these complex regions. Figure 14j, which presents the only results for Region 3 (rosette 7), shows the analytic model to be relatively stiff longitudinally. A more detailed discussion of the results follows:

Region 1: In this region (encompassing rosettes 1, 2, and 3, as shown in Figs. 14a, 14b and 14c, respectively), the finite element model accurately represents the physical charactertistics of the tail cone. This region of the tail cone is comprised of single sheets of magnesium sheeting and does not include any reinforcing panels, such as the doubler located on the fourth quadrant of the port side of the tail cone. From the results of rosettes 1 and 2 it can be seen that the predicted circumferential and longitudinal normal strains are well modeled within the experimental envelope. The exception is the circumferential strain prediction of rosette 1 wherein the relatively low level circumferential normal strain, ϵ_x, is overpredicted.

Regions 4 and 6: In these regions, as shown in Figures 14c and 14d, and 14e, the model approximates the stiffness properties determined by the experimental strain results reasonably well. For these regions the elements are modeled exactly as the engineeing prints require. The correlation task defined for this case is for strains of a simple area with no reinforcing panels nor rivets. This simplification therefore eliminates the complexities that have made modeling difficult in the other regions.

The results for Region 1 suggest that the 3rd quadrant for the forward port side of the tail cone is modeled well. When compared with the results for Regions 4 and 6, which also correlate well, it appears that the results for the circumferential predictions in Region 1 are inexplicable. As is discussed below, because of inherent modeling problems in Regions 2 and 3, it would be expected that modeling difficulties in Regions 2 and 3, due to the longitudinal direction proximity of locally complex built–up regions, could also affect the predictions in rosette 1.

Region 5: As can be seen in Figure 14f, the predicted circumferential and longitudinal normal strains show the model to be modeled too stiff. But the circumferential and longitudinal strains are only 35% and 25% , respectively, different from the experimentally determined strains. This level of error is close to the 30% experimental envelope, which indicates that the modeling is close, although not within the experimental envelope.

Regions 2, and 7: Figures 14g, 14h and 14i tell exactly the same story for both Regions 2 and 7. Despite relatively close proximity of these regions to Region 1, which demonstrated good correlation, the correlations for these regions aren't nearly as good. As typified by Regions 2, the finite elements to the left of rosette 4 (and rosette 17) and to the right of rosette 6 (and rosette 15) are modeled with the sum of the thicknesses for the frames and magnesium skins riveted together in these areas. The area betweeen rosettes 6 and 4, however, are modeled as the engineering prints prescribe: with single thickness magnesium skin properties.

Rosettes 6 and 15 produced exactly the same results, as they are both located at the same (z) location on the tailcone (refer to the Table 2, listing the rosette locations and Figure 12, giving a schematic depiction of their locations). Rosettes 5 and 16 tell the same story, as they are also located on the same (z) location on the tailcone but at a different theta angle. And rosettes 4 and 17 likewise tell the same story since they too are located at the same (z) location on the tail cone, but at "mirror image" circumferential angles (i.e., equal and opposite to each other, as measured from the top–most part of the tail cone). For rosettes 5 and 16, (node locations 224 and 193) there are no riveted areas and therefore the shell elements were modeled with single thickness magnesium properties.

Therefore, as a suggestion for future modeling changes, the most obvious change in this simple region would be to change the modulus of elasticity by a small amount, such as 5%. This region was modeled with "bottom" skin thicknesses, with magnesium properties, which is exactly as the engineering prints prescribe. This implies that perhaps a case can be made for an adjustment in the magnesium modulus of elasticity and a subsequent recheck on the correlation.

Region 3: As shown in Figure 14j, the correlational results for this region are uniformly poor. Although this region is likewise in a part of the structure with local complexity, the levels of strain are generally quite low. Thus, as an indicator of strain correlation at least with respect to lateral static loads. This region would not be expected to yield good correlational results.

A summary of the normal strain findings for these regions is as follows: For rosettes 4 and 17, and 6 and 15, the circumferrential stiffness of the model is too high (too stiff) and the longitudinal stiffness of the model is too low (too soft). Note that for rosette 4, the analytical longitudinal strains are close to those experimentally determined and that for rosette 5, the circumferential strains are within the experimental envelope; thus these results are still consistent with the general pattern. It would appear then that although the elements to the left of rosettes 4 and 17 and to the right of 6 and 15 were modeled with the sum of the thickness for the attached magnesium skins and frames, additional changes would have to be made to the modeling for the longitudinal stiffnesses. It may well be that the rivets cause a certain amount of slipping to occur under loading thereby causing reduction from the strains which would be manifested by a continuous sheet of metal. Changing the modeling assumptions of the riveted areas wherein the sum of the thicknesses is used, would greatly affect the longitudinal predictions of even the neighboring areas under rosettes 5 and 16 where the model is seen to be longitudinally too stiff.

In addressing the circumferential strains, wherein the model was found to be too stiff relative to the measured strain, i.e. the riveted areas (frame locations), it may be that these contributing complexities cannot be practically modeled within the scope of the available FEM analysis. In this regard, however, recourse might be possible to using some form of a *rivet scale factor* for adjusting the effective thickness of the model in the riveted regions. Such a scheme might enable a more complete study of the effects of rivets on the effective stiffness properties.

Shear strain results

The results of the correlations with respect to *shear* strains predominantly show the finite element model to be weak in its ability to predict this type of strain accurately. There doesn't appear to be much of a general pattern which can be determined from the results, in contrast to the case with the normal strains. Indeed, except for rosettes 1, 11 and 12, the effective analytical shearing moduli are seen to be stiffer than those resulting from the experimental data. As is developed above, Regions 2 and 7 are complex regions to model and it could be expected that the resulting experimental and analytical stiffnesses in these regions would differ. For rosette 12, whose strain results are seen to correlate very well with regard to *normal* strains, it is an unexpected result that the analytical and experimental shearing strains differ so markedly, as is shown in Figure 14d. Furthermore, although rosettes 12 and 14 were both located in regions not very dissimilar from each

other and produced similar normal strain results, the shear strain results from these two rosettes are seen to be completely dissimilar. Finally, even for rosette 1 wherein the longitudinal strains compared well with the experimental strains, the circumferential ones did not. The shearing strain may be a further indication there is some modeling requirements not taken into account at this location.

General summary

The only location wherein the analytic shearing strain correlated well with the experimental was at rosette location 11, as shown in Fig. 14d. Note that the correlation for this rosette is outstandingly excellent for both normal and shear strains. Thus, the shear strain modeling capability of the FEM analysis is seen to be inconclusive. One overall conclusion, for the longitudinal and cirumferential normal strains, however, is that very good correlation was achieved. Although in Regions 2 and 7, the results did not correlate to the experimental, the results were consistent in regions 2 and 7, showing that the model and the experimental data themselves were not imbedded with major analytical and experimental inconsistencies. The areas to be concentrated on in further studies would be regions 2 and 7. As will be seen in the following sections, it is believed that the changes in the stiffness will bring to bear a better correlation to the frequency responses results.

5.0 ANAYTICAL PREDICTIONS OF MODAL CHARACTERISTICS

5.1 Use of the Finite Element Eigenvalue Analysis

After the finite element analysis was adjusted to incorporate any discrepancies identified by the static strain correlation and the calculation of tail cone mass, the eigenvalue calculation capability of the COSMOS/M FEM analysis was activated. It should be noted that the ultimate use of the dynamic analysis features of the FEM analysis was to be the calculation of the frequency response functions. To this end the COSMOS/M FEM analysis directly uses the results of the eigenvalue analysis to generate these response functions. Thus, the calculated modal characteristics play a critical role in obtaining accurate correlation results.

Initially, a "first pass" model was analyzed which consisted of the entire tail cone assembly (i.e., including the drive shaft) mounted in the cantilevered configuration. Examination of these results, however, identified two basic problems: First, the resulting natural frequencies and, more importantly, the mode shapes, were quite sensitive to the modeling of the drive shaft. Second, the weight calculated by the analysis (from the masses of the structural elements) was considerably less than the actual measured weight of the tail cone.

An attempt was made to model the details of the drive shaft and the support bearing assemblies (see Fig. 3). However, the details of the bearing mounts were found to not be amenable to simple, yet accurate, modeling techniques. It was therefore decided to remove the drive shaft and thereby simplify the structure to a configuration which could be modeled with confidence. These initial calculations also served to identify idiosyncrasies of the eigenvalue solution calculations of the COSMOS/M analysis, wherein such a large number of degrees of freedom are used. Also, as a result of these initial calculations, a thorough inventory of nonstructural mass was made. The additional masses found were included in the model and the modeling was then frozen to include only the updated elements for the two support configurations, but without the drive shaft. The remainder of this chapter presents the results of the eigenvalue analyses of the two principal configurations: cantilevered and free–free.

5.2 Cantilevered Configuration

The COSMOS/M eigenvalue analysis of the cantilevered configuration (without drive shaft) was implemented to yield a frequency range within the frequency response test range of up to 100 rad/sec. This calculation yielded the natural frequencies and mode descriptions given in Table 3:

Table 3 – Calculated natural frequencies, cantilevered (no drive shaft) configuration

mode	frequency (Hz)	mode description
1	18.060	1st vertical bending
2	19.506	1st lateral bending
3	79.610	frame 7.5, 1st local mode
4	83.133	2nd vertical bending
5	86.364	2nd lateral bending
6	90.770	frame 7.5, 2nd local mode
7	91.344	frame 7.5, 3rd local mode
8	103.589	skin breathing/bending mode

Note that modes 3, 6 and 7 are local modes involving essentially rigid body – like motions of internal frame 7.5 relative to the rest of the tail cone. Thus, pictorial representations of these modes would be impractical and are omitted from the graphical depictions of the mode shapes presented in Figs. 15a thru 15e. Figures 15a and 15b present the two first cantilevered "beam bending" modes wherein mode 1 is that associated with vertical bending and mode 2 (the higher frequency mode) is that associated with lateral bending. This relative correlation of mode with frequency is consistent with the greater stiffness in the lateral direction resulting from the side mounted stiffeners and the doubler of the port side. Similarly, the respective second "beam bending"–*like* modes in the vertical and lateral directions are presented in Figs 15c and 15d, respectively. Again, the side stiffeners and the port side doubler result in a higher frequency for the lateral mode. Note that these two modes mark a transition from beam–like modes to modes with significant local deformation features. Figure 15c shows significant ovalization of the cross–sections near the midpoint of the tail cone. Fig. 15e presents a graphical depection of a true non–beam, three dimensional mode, which can be termed the "skin breathing" local bending mode.

5.3 Simulated Free–Free Configuration

The modeling of a pure free–free structure cannot be accomplished with the COSMOS/M analysis since such a structure necessarily yields a nonpositive–definite stiffness matrix and the analysis will terminate without any useful results. Thus, it became necessary to simulate the free–free condition using a system of six (fictitious) springs to stabilize the structure. In reality, the free–free configuration actually tested was not a pure free–free condition in that the bungee cords provided vertical (plunge), pitching and yawing motion stiffnesses and gravitational/pendular motion effects provided the fore and aft, lateral and rolling motion stiffnesses. In order to accommodate these effective stiffnesses, artificial stiffnesses were introduced in the analysis with very low values in order to keep the resulting rigid body mode frequencies to values in the order of magnitude of 1 Hz. The introduction of these low frequencies, however, increased the complexity of the analysis enough so that a broad spectrum of natural frequencies could be obtained. Indeed, the Lanczos eigenvalue extraction method implemented in the analysis repeatedly predicted "false" modes which could not be adequately controlled because of the size of the problem. Consequently, only a total of eight frequencies could be predicted which, unfortunately, necessitated the inclusion of the six "rigid body" modes. Thus, predictions of only two elastic modes could be obtained. A summary of the COSMOS/M eigenvalue analysis of the simulated free–free configuration is given in Table 4 and graphically in Figures 16a and 16b.

Table 4 – Calculated natural frequencies, free–free (no drive shaft) configuration

mode	frequency (Hz)	mode description
1	0.831	rigid body
2	0.833	rigid body
3	1.086	rigid body
4	1.224	rigid body
5	1.334	rigid body
6	1.346	rigid body
7	70.442	1st vertical bending
8	74.683	1st lateral bending

A comparison of Figs 16a and 16b again reveals that the lateral bending mode is more greatly stiffened than is the vertical mode resulting principally from the side stiffeners. The stiffening due to the port side doubler would be expected to contribute relatively less to the lateral mode stiffening because of the reduced strain state at the root end of the tail cone in the free–free configuration. Note that is each of these modes evidence of large amplitude motion of frame 7.5 can be detected.

The inability of the eigenvalue analysis (Lanczos method) within COSMOS/M to obtain more than eight natural modes (six of which were the rigid–body modes) was especially disappointing since the 386 technology version of the analysis used was specified to have the capability to handle many more times the numbers of degrees of freedom, nodes and elements than was used for the modeling of the S–55 tail cone. For the S–55 tail cone (with the free–free configuration constraints) 8,136 degrees of freedom , 1,898 nodes and 1,898 elements were used; the (386 version) COSMOS/M analysis is specified to be capable of handling 25,000 degrees of freedom, 10,000 nodes and 10,000 elements.

Direct measurement of the modal frequencies and mode shapes was not practical in this study for a number of reasons. First, however, it should be kept in mind that "modal characteristics" are essentially mathematical abstractions resulting from a simplified mathematical modeling. Here, the simplifications include the assumption of linearity and the absence of any form of damping. To be sure, there are modal analyses which, when taken together with several measured frequency response functions, can *infer* "effective" natural frequencies, damping ratios and mode shapes. Also, techniques exist, such as the ITD method (Ref. 18), which can extract out effective natural frequencies, (viscous) damping ratios and mode shapes from transient "ring–down" responses following an impulsive (shock) to the structure. However, shock excitations at levels needed to produce sufficient transient responses are potentially damaging to aircraft type structures. Such ring–down analyses also require a multiplicity of transient responses from different locations on the structure.

Neither the use of the modal analysis of frequency response functions nor the ITD method were practical in this study, however, since both approaches would have required many more spacial simultaneous measurements than were practical within either the availability of experimental resuorces or the scope of the present study. There is an additional aspect of the rotorcraft vibration problem which impacts on this issue. The rotorcraft vibration problem deals not only with the resonance conditions, which are only

what modal representations of the structure address, but of equal importance, with the *anti*resonance conditions, where well–designed rotorcraft should operate. These conditions are not typically addressed with such modal analyses as are presently available. To be sure, the future development of such special purpose modal analyses, which would include the definition of antiresonance conditions, would be justified on the basis of the advantageous use which could be made in the rotorcraft problem. In summary, for all of these reasons it was concluded that, within the context of the present study, meaningful comparisons between the theoretical and experimental dynamic characteristics of the tail cone were best made using frequency response functions solely. The following chapter addresses this correlational task.

6.0 CORRELATION OF FREQUENCY RESPONSE FUNCTIONS

6.1 Modeling Considerations

To a certain extent preliminary shake–test results were used as a guide to the extent of detail to be used in the finite element modeling. For instance, since the hard–back structure was known to have its first natural frequency at a value of approximately 108 Hz, the potential existed for some interaction of the hard–back with the tail cone. Indeed, a set of COSMOS/M input data was compiled for the hard–back structure (using a previously compiled FESDEC finite element modeling). However, the preliminary shake–tests confirmed that the responses of the hard–back structure were indeed so small as to be in the noise level. Consequently, the basic modeling of the cantilevered mount configuration was simplified to be one of a *rigid* attachment.

In comparing the frequency response plots, some modes predicted by the finite element model, such as the local frame modes, were not picked up in the frequency sweeps made during the preliminary shake–testing phase of the project. Additionally, drive shaft modes were not be picked up by the accelerometers during the preliminary shake–tests. This was due to the fact that the accelerometers were placed only along the horizontal stiffeners on the tail cone and not on the frames or skins or drive shaft of the tail cone. For this reason, and those relating to the complexities of modeling the drive shaft, this subcomponent was physically removed from the tail cone and from further FEM considerations.

6.2 Finite Element Analysis

The validation of the finite element modeling, as provided by the static strain correlations, actually verified only the stiffness matrix portion of the finite element modeling. For the dynamic analysis portions of the study the mass properties are of equal importance. Unfortunately, detailed direct verifications of the mass modeling is not generally possible, as it is with the stiffness modeling. To a degree, the accurate elastic modeling of structural elements often implies accurate modeling of the mass modeling. This would be expected to be true in the case of such simple structural elements as beams, plates and shells. In the case of such elements a verification of the mass element modeling

must come indirectly using the results of suitable dynamic responses, such as the frequency response functions. However, some mass modeling comes from portions of the structure which are not necessarily elastic. In the case of such elements the only tool for verification are the calculations of total structure weight and inertia. The following section deals with the correlation of total tail cone weight.

Weight of tail cone

Although the tail cone was weighed before installation on the hard–back structure, measurements of the inertias, which would have proved useful, were not made. With the tail rotor drive shaft still installed the tail cone weighed 130 lb. As was the case with preliminary shake–tests, preliminary finite element (eigenvalue) calculations were made to ascertain the frequencies of the primary modes. Although these calculations produced reasonably accurate static strain predictions, significant discrepancies were detected not only in the natural frequencies, but in the weight calculations. Consequently, a detailed accounting of the nonstructural masses was made; included were such items as rivets, polyethelene filler in the stiffeners, etc. As a result of these investigations the calculated weight of the tail cone was brought in line with the experimentally measured value, as shown in the following table:

Table 5 – Weight correlation

Configuration	Predicted Weight (lb)	Measured Weight (lb)	% Difference
with drive shaft	136.	130 (± 5)	5.0
w/o drive shaft	112.47	107 (± 5)	5.0

Calculation of frequency response functions

Within the COSMOS/M analysis the frequency response functions are generated indirectly from the modal characteristics (natural frequencies and mode shapes) and from the values of viscous equivalent structural damping ascribed to each of the various natural modes included in the calculation. [Note that direct calculation of the frequency response

functions using only the mass, damping and stiffness matrices is not an available capability with the COSMOS/M analysis.] For present purposes the frequency response functions for the tail cone were generated with an assumed value of viscous structural equivalent damping (for all modes selected) of 0.005. This value was arbitrarily selected as being representative of full–scale metal semimonocoque structures. Unfortunately, resources were not available to this research program to enable a modal analysis of the frequency response function measurements. Furthermore, this procedure was consistent with the scope of the program since the finite element model was a strictly linear one and, therefore, could not take into account any of the nonlinear damping characteristics of the tail cone. [Such considerations must await further more specialized research programs with this equipment.]

6.3 Shake Tests

A mechanical shaker was used to excite the tail cone laterally, and accelerometers positioned at intervals along the tail cone were used to measure the response in both the vertical and lateral directions. The applied sinusoidal force was measured by a load cell connected in series with the shaker. Aluminum mounts were attached to the tail cone at each accelerometer station, as well as the load cell station. These mounts had vertical and horizontal threaded holes which allowed each accelerometer to be firmly secured.

The shaker was suspended from a frame adjacent to the load cell position. Piano wire connected the shaker to the load cell. A bungee cord attached to the wire at the opposite end of the shaker was stretched and secured to a wall mount so as to keep the piano wire in tension. Five accelerometers were used during each run of the shake test, with 9 runs required to measure the response at every location. This allowed for redundant measurements during each run to monitor run consistency. Accelerometer placement was chosen such that high sensitivity accelerometers were used at the rear and vertical mounts, where a much smaller response was expected. The shaker and load cell remained at the same position throughout all tests.

As shown in Fig. 10, excitation voltage was supplied to the shaker by the HP frequency analyzer, using its burst chirp source option at a frequency range of 0 to 100 Hz. This source signal was amplified and then input to the shaker. During each run, output from the load cell and five accelerometers were amplified by a 6–channel amplifier bank,

and then recorded on the first six channels of an FM data recorder. Load cell and accelerometer output for each run were taped on a Betamax tape cassette with a sufficiently long enough period for the frequency analyzer to create a transfer function of input load and output acceleration, with its averaging option set to ten averages (approximately 2 minutes).

The frequency response functions were measured and calculated at various of the accelerometer locations defined in Table 1. Mostly, responses were measured in the (x) and/or (y) directions at these locations. The extent of measurements made was greatest for the cantilevered mount configuration and, because of the time required to make the measurements, to a lesser extent for the free–free mount configuration. Since some of the results turned out to be redundant for different locations, correlational results are presented for both right (R) and left (L) sides of the tail cone only for locations 2, 4, 6, 8, 9, (as defined in Table 1) and for either one side or the other for locations 10, 11 and 12. These locations were selected by virtue of the results being representative of results from other intermediary locations and of there being a more complete body of data at these locations for both the cantileved and free–free configurations.

6.4 Correlational Results Configuration no. 1 – Cantilevered Mount

The frequency response function correlation results for this configuration are presented in Figures 17a thru 17n. Generally, these figures show response results for locations starting at the cantilevered end of the tail cone and generally proceeding progressively toward the aft end. The FEM node numbers are thus monotonically increasing and correspond to the physical dimensions given in Table 1. Also, each figure presents, where possible, lateral (x – direction) responses together with the simultaneous vertical (y – direction) responses. Note that, for this configuration, the excitation force has a greater activity in the vertical direction than the lateral by virtue of the 60° inclination of the shaker sting relative to the floor (see Fig. 8). The principal results which are of principal interest relate to the responses clustered about the first mode resonances at frequencies about 22 Hz and those clustered about resonance response activity in the frequency range of from 75 Hz to about 90 Hz. With this distinction in mind a discussion of the correlation results follows. The results are addressed with respect to longitudinal location (by increasing aft location) and similarity of construction.

General observations:

The responses for the cantilevered configuration generally show many random spikes in the low frequency band of the test frequency spectrum (i.e., that portion below the first bending mode frequencies); this result can be considered to be an inherent source of noise, attributable to the fact that during the test, a burst chirp signal was used, as opposed to the sine sweep dwell signal. Figures 17a through 17n all demonstrate that there are some significant local modes at the higher frequencies, in particular, above 75 Hz.

The finite element model predicts two modes near 20 Hz, which are the first lateral and first bending modes and two modes near 84 Hz, which are the second lateral and vertical bending modes. It should be noted that the finite element model was computed to weigh about six pounds more than the actual measured weight of the tail cone. This discrepancy could be expected to result in the first two measured bending modes having higher resonance frequencies than the coresponding first two predicted bending mode resonant frequencies.

Additionally, the finite element model predicts two local modes for frame 7.5 at approximately 91 Hz, and a breathing mode near 103 Hz. Since this study did not include a modal analysis and mode shape animation of the measure results, uncertainty exists in the higher frequency results as to which modes were observed, either local or bending modes. But it is believed that most of the higher frequency resonance peaks are indicative of some local mode action at the measured locations since the finite element model does demonstrate local skin breathing modes and frame flexure modes.

In the finite element model frames 0, 7.5, 26, 60.375, and 94.75 were modeled entirely with shell elements, but for the remainder of the frames further aft the flange portions of the frames were modeled using 3D beam elements. Frame 7.5 had the largest flange width, so the finite element model was able to pick up this frame's local modes. Frame 7.5 was predicted to resonante first in a diaphram motion, that is to say, the flanges flexed forward and backward, at 79.6 Hz, and then in two seperate assymetric modes, at 91 Hz. Thus, if the finite element model were modeled in more detail with respect to the frames, the local modes induced by the frames and frame appendages could possibly be picked up . It appears from the results, overall, that there are generally four modal resonances occurring in the higher frequencies. It is interesting to note that in the finite element model predictions for the normal modes, there are five predicted modes between 79 and 100 Hz,

and one more mode at 103.6 Hz. Three of those five modes are local modes involving frame 7.5 .

It is instructive to note that several modeling discrepancies exist which can be expected to impact on the frequency response results. Specific issues relating to accuracy which can be identified are as follows:

1. The tail cone has many relatively small appendages attached to the frames; these appendages were modeled as point masses.

2. The tail cone has many riveted points where the skins are riveted to frames, reinforcing panels are riveted to the skins, and in several instances, the skins are overlapping from two different regions and riveted together on top of the frames.

3. The accelerometer blocks are mounted on the longitudinal stiffeners, which are modeled as 3–D beam elements (3–node uniaxial beams with six degrees of freedom per end node plus a third node for orientation). If modeled with shell elements, the some local mode activity may be predicted by the finite element model. Furthermore, the discrete mass loading of the aluminum mounting blocks could be contributing to some local mode activity picked up by the measurements.

Detailed observations:

The *general* trends for all figures, 17a thru 17n, show remarkably good correlation beteen the measured and predicted frequency response functions, since the two first bending modal resonances and the two second bending modal resonances are clearly in evidence as the general shape and magnitude of the broad band antiresonance portions of the response functions are well–predicted. There are, furthermore, some local trends which are well captured by the FEM analysis.

In the following discussions, the correlation results are discussed around the observation that there are peaks in the higher frequency portions of the response which are assumed to be contributions from local modes in the frequency range of interest. The correlation is considered to be sucessful if the general shapes match for both the measured and predicted response.

Locations no. 2 (z = 25.64) and no. 6 (z = 94.15):

Modeling assumptions: At locations 2 and 6, the frames are both modeled with shell elements and no beam modeling takes place except for the longitudinal stiffeners, on which the accelerometer blocks are mounted.

Correlation of major resonances and antiresonances: As shown in Figures 17a & 17b, and in 17c & 17d, the lateral responses for the left (doubler reinforced side of the tailcone) are remarkably similar. For the (x) motion responses for node 435 and 942, we note that the first two bending modes are closely correlated, and up to a frequency of approximately 83 Hz, it can be seen that the FEM results and the measured responses follow each other quite closely.

Correlation of left side responses vs. right side responses:

Lateral motion: In Figures 17a & 17b and 17c & 17d, the lateral, i.e. (x) motion, responses for the right (R), or starboard sides of locations 2 and 6 are seen to be identical in general shape, even though the antiresonances are not at the same frequency. The lateral responses for the left (L), or port side responses for locations 2 and 6 are seen to have the same shape, but for location 6 the responses have a higher level of magnitude for all the measured resonance peaks. However, the right and left responses at the same location, for instance location no. 2, do not match. This is an expected result since the port side of the tailcone is modeled differently than the starboard side. It is not apparent, however, what kind of activity is being represented by the various resonant peaks shown in the figures.

Vertical motion: For the vertical, i.e. y motion, responses, both the right and left vertical measured and predicted responses correlate well. But again, the vertical response signature on the port side of the tailcone is different than that for the starboard side of the tail cone. But the response signature for the port sides for locations 2 and 6 are almost identical to each other, and similarly, the response for the starboard sides of the the tail cone for locations 2 and 6 are also almost identical to each other.

Locations no. 4 (z = 60.08) and no. 8 (z = 128.98):

Modeling assumptions: The correlation results for these longitudinal locations are similar by virtue of the similarity of the actual construction details and, as a result, the required

modeling assumptions taken at these locations. The results for these locations are shown in Figures 17e thru 17h. At both of these longitudinal locations, (corresponding to frame 60.376 and 128.98, respectively) the construction consists of overlapping skins riveted to a frame. At frame 60.376 the finite element model is modeled such that the node ring consists of shell elements. The section of the frame that has the two magnesium skins overlapping the frame is modeled as one thickness equaling the sum of the two skins plus the thickness of the frame, rather than either three seperate skins, or a more special modeling of three discrete sheets of metal riveted together. At location 8, or frame 129.125, the three riveted sheets of metal are modeled as a combination of a shell element with the sum of the three thicknesses, and the flange portion of the frame is modeled using unsymmetric 3–D beam elements.

Correlation of major resonances and antiresonances: From the figures it can be seen that the FEM results closely follow the measured responses, for both the left lateral (L–x) responses. For the right lateral (R–x) responses, Figure 17f does show that the finite element model calculates an antiresonance frequency near 78 Hz for the frame that was modeled with all shell elements. However, as shown in Figure 17h, for the frame that was modeled with beam elements, the finite element model does not predict the antiresonance point, although the resonance peaks match very well at about 88 Hz. This discepancy could be due to the constraining effect of 3–D beam modeling of the further aft frames. As well as the fact that the longitudinal stiffeners were also modeled as 3–D beam elements. The measured and predicted responses in the vertical direction, as are also shown in Figures 17e thru 17h, are seen to be extremely well–correlated, especially at the low frequency portion of the frequency spectrum. Again, the additional resonance peaks in the higher frequencies may be due to the longitudinal stiffener and frame local mode activity not adequately represented by the finite element model.

Correlation of left side responses vs. right side responses:

Lateral motion: As can be seen by comparing Figures 17e with 17g and 17f with 17h, the measured responses for the left and right sides of the tail cone, at the same location, differ. In particular, as shown in comparing Figures 17f and 17h for the lateral responses, the right hand or starboard side of location 4 (4L) (which is not as heavily reinforced as the left or port side of the tail cone) show more measured resonances than the port side of the tail cone. This is most likely due to the fact that the starboard side of the tail cone is not reinforced as well as the port side of the tail cone, is less stiff and, hence, capable of lower

frequency local resonances. For location 8, it also seen that the port side of the tail cone of the tail cone is experiencing a response that is slightly different than the starboard side of the tail cone.

Vertical motion: Above, 70 Hz, the vertical responses for the port side of the tail cone at location 4, node 714(y), is experiencing four resonance peaks in its response bandwidth whereas the starboard side of the tail cone is experiencing three large, well–separated peaks. For location 8, the response pattern is identical to location 4 for the left and right frequency response results, respectively. This can be attributed to the fact that the tailcone is physically constructed in the same fashion at both of these locations, with two overlapping magnesium skins riveted onto a frame.

By way of a brief intermediary summary, the results for location sections 2, 4, 6, and 8 seem to point to the conclusion that the locations which are modeled with the shell elements for the frames, correlate well with the measured antiresonces, excepting for, of course, the local modes in the frames and longitudinal stiffeners.

Locations no. 9 (z = 162.95) and no. 10 (z = 197.14):

Modeling assumptions: At both Locations 9 and 10, the modeling consists of shell elements for the skins and beam elements for the flanges of the frames. The frequency response functions for these locations are shown in Figures 17i thru 17l.

Correlation of major resonances and antiresonances: For location 9, the major resonance peaks and the general shape of the frequency response functions correlate quite well. Again, there are still the additional higher frequency resonance peaks which are yet unexplained as to the particular motion to which these peaks can be attributed. For location 10, only the lateral response was measured and the correlation follows smoothly except for the two resonance peaks between 75 and 85 Hz. A comparison between the right and left responses at the same location follows:

Correlation of left side responses vs. right side responses:

Lateral motion: For location 9 (frame 163), again the left and right side responses are slightly different; however, the response levels are the same. This is to be expected since frame 163 is nearer to the end of the tail cone, and the end of the tail cone should behave

more like a beam than would those portions in the center. For location 10, (frame 197), the lateral respsonses on the left and the right sides are identical, in response level and shape, indicating that the tail cone, near the end, is pretty much behaving as a beam with a concentrated mass.

Vertical responses: The vertical response on the right and left of frame 163 correlate very well, and are practically identical except that the starboard side of the tail cone response level is about 10 db higher.

(Driving point) location no. 12 (z = 213.23):

At the driving point location at the end of the tail cone, the shapes of the response curves for right and left sides are almost identical. As shown in Figure 17m, there is a FEM calculated resonance at about 68 Hz, and a resonance at about 65 Hz for the measured response. The four peaks present in all the other response locations are still present at the end of the tailcone as well. This would appear to indicate local mode activity with the longitudinal stiffeners.

6.5 Correlational Results, Configuration no. 2 – Free–free Support

General observations:

In all figures for this configuration, Figures 18a thru 18i, the correlation for response amplitude and shape are seen to have correlated very well. In the free–free configuration both ends of the tail cone are negligibly strained in contrast to the highly strained cantilevered boundary condition inherent in the cantilevered configuration. The high degree of correlation obtained with the free–free configuration in both the vertical and lateral directions would argue that those stiffness and mass properties which are actually active in this configuration are generally modeled well. Detailed observations of the results follow:

Location no. 2 (z = 25.64) :

For location no. 2 (frame 25.64), measurements were made for the right lateral, right vertical and left lateral responses of the tailcone. As can be seen from Figures 18a and 18b, the major peaks are predicted by the finite element model for the lateral and vertial directions. The vertical response is telling us that the lateral bending mode has some component of vertical as well as lateral motion.

Locations no. 4 (z = 60.08) and no. 8 (z = 128.98):

In Figures 18c, 18d and 18e, we see that the lateral (x–direction) responses for location no. 4 (frame 60.08) and location no. 8 (frame 128.98), especially the lateral bending mode resonance frequency of about 75 Hz, are all similar and well–correlated. The vertical response at frame 60.08 also shows that the lateral bending resonance mode at this frequency has a significant vertical component, such as was found for the responses at location no. 2.

Locations no. 9 (z = 162.95) and no. 10 (z = 197.14):

In Figures 18f and 18g, the correlation for location 9 is seen to be excellent; not only are the vertical and lateral resonances again seen to occcur at about 75 Hz but the emergence of a significant antiresonance frequency near 90 Hz is now evident in both the experimental and analytical results. Figure 18f indicates that this frame has significant vertical and lateral motion components at this resonance point. As shown in Figure 18f, the lateral response indicates a resonance at 75 Hz, but the vertical response indicates resonances at about 68 and 76 Hz, indicating that the 75 Hz peak is actually a double peak comprised of the lateral and vertical motion components at this frame.

Comparing Figures 18f with 18h shows the results to be remarkably well–correlated in that not only are antiresonances accurately predicted for these two locations, but the general character of the resonance vs antiresonance frequency placements are correctly predicted. This result also runs true for the vertical motion (coupled) results although the analyatical vertical motion responses at the lower frequency resonance condition are indicating less damping (less attenuation) than was measured. Note that the correlation results for location 10 are actually better than for location 9.

(Driving point) location no. 11 (z = 213.23):

At this location, the measured and predicted responses are clearly correlating well with regard to the fundamental resonance at about 75 Hz present in all the measured responses for the free free configuration, and the antiresonance frequency at about 53 Hz. Note that the results for this location are very similar to those for location 10. A comparison of Figures 18f thru 18i clearly shows the antiresonance frequency to be location dependent and the predicted variation of this frequency with location is also well–correlated.

In brief summary, it appears that overall, the tailcone's stiffness and mass properties in the free–free configuration, are in good correlation with each other. Not only are the resonance and discrete antiresonance frequencies well–correlated, but the general antiresonance trends over all the lower bandwidth (below the first resonances) results and for most of the higher bandwidth are also quite well–correlated. It would appear that it is in those configuration/locations, wherein the tail cone is more highly stressed that accurate modeling of the details is most crucial to a good correlation.

7.0 CONCLUSIONS

7.1 Elastic Modeling

In the elastic modeling, the static results seemed to point towards more detailed modeling of the area between frames 0 and 7.5. This is a highly complex area to model as there are riveted overlapping magnesium skins. It appears that accurate modeling of these riveted joints impact on the correlation to a large degree in this region. Careful consideration for modeling the "effective thickness" may be embarked upon in future studies to learn how to accurately model areas such as these – it would especialy be useful information for the aircraft industry as a whole.

In all areas that were not characterized by abrupt changes in stiffness and mass properites, the correlation turned out very well. This further confirms the importance of learning how to model the riveted fastening of the skins and frames in athe modeling of helicopter fuselage structural components.

7.2 Dynamic Modeling

For purposes of evaluating the degree of correlation achieved and the requirements of further study three levels of correlation can be defined:

Level I. Correct identification of fundamental resonance and antiresonance frequencies, and duplication of basic nonresonance trends. This degree of correlation can be defined using only the amplitudes of the frequency response functions.

Level II. Correct identification of secondary resonances and antiresonances (local modes) and correct prediction of damping in fundamental resonances and antiresonances. This degree of correlation would require both amplitude and phase angle frequency response function results.

Level III. Correct identification of damping in both secondary resonances and antiresonances. Again, this degree of correlation would require both amplitude and phase angle frequency response function results.

7.3 General Conclusions

As was demonstrated especially for the free–free configuration, the overall modeling of the tail cone was sufficient to predict the major modes of vibration, namely, the first and second bending modes of the tail cone in the cantilevered configuration and the first bending modes for the free–free configuration. The particular problems seemed to be encountered in the high frequency end of the response spectrum. In this range, there were consistently four resonance peaks in the lateral direction (two well–separated modes and two coupled modes) and three resonance peaks in the vertical direction (all very well separated and defined). For the free–free configuration the finite element model could only predict at most two of these peaks. It is felt that the modeling deficiencies include modeling the riveted joints correctly, as well as the longitudinal stiffeners. It may well be that the detailed distribution of the added point masses, as described in Ref. 17, may need to be redistributed in a different manner. But there certainly seems to be a few modes that aren't predicted at all by the finite element analysis. It was noted previously, however, that the finite element model is capable of predicting local modes and does so when the detail is improved.

This study points to the fact that perhaps, since the accelerometers were mounted only to the 0 and 180 degree longitudinal stiffeners and the comparison is based on only the responses at these locations, then the accurate modeling of these stiffeners is crucial to picking up the local bending or breathing modes of the longitudinal stiffeners. If responses at different locations were measured (by mounting the measurement tranducers directly to skin panels or by using laser vibrometry techniques, e.g.), then perhaps the lumped modeling of the 0 and 180 degree stiffeners as beam elements might not be an unreasonable approximation to these components.

7.4 Specific Conclusions

Specific conclusions reached on the basis of the results achieved are as follows:

1. Although identifiable deficiencies exist in the finite element modeling, excellent Level I correlation was achieved. Not only were the static strain results well–correlated, except in areas of high strain gradients, but the dynamic frequency response results were uniformly well–correlated within the lower frequency band ($f \leq$ 25 to 40 Hz) typical of blade passage frequencies for helicopters of moderate size.

2. Relatively poor Level II correlation was achieved and an evaluation of Level III correlation is inappropriate for this first study. Correlation of detailed static strains typical of regions near the cantilevered end of the tail cone where abrupt changes in the stiffness occur (due the to heavy amount of rivet fastening and reinforcements in these areas) showed the finite element modeling to be insufficient. This insufficiency affected both the static correlation and the high frequncy end of the response spection for the dynamic correlation. Because the meshing in these areas was quite extensive, one probable cause of the lack of all–over correlation can attributed to the lack of detail in the basic element library of the finite element analysis. Indeed, the results define a need for a specific *riveted overlapping skin shell element* to be developed for general finite element modeling.

3. The finite element analysis was more able to predict local modes occurring at the frames which were more accurately modeled (i.e., frames 0 to 94.75 where the frames were modeled completely using shell elements).

4. In the areas where the frames were modeled using beam elements for the flange components, the finite element modeling had insufficient detail in the vicinities of the mounting locations of the accelerometers. This insufficiency might be rectified by remodeling the 0 and 180 degree stiffeners using shell elements, since these locations are the actual measurement locations. This may also provide the basis for improved Level II correlation by allowing prediction of the missing resonances and antiresonances experimentally observed in the higher frequency range.

5. The value of viscous equivalent structural damping critical damping ratio was arbitrarily selected at a level of .005 for all modes used (based on previous experience). To first order approximation this level of modal damping was generally accurate, based on the correlation of the peak resonance response peaks of the frequency response functions.

6. The RPI Airframe Component Shake–Test Facility has matured to the point where more advanced dynamic resarch can be accomplished. The COSMOS/M data base achieved for the Sikorsky S–55 tail cone as a result of this study is a viable resource upon which future studies can be profitably based.

8.0 RECOMMENDATIONS FOR FUTURE RESEARCH

All recommendations for future research are based on achieving greatly improved Level II and III correlation. Two major general thrusts should be pursued: improved analytical modeling and further, more extensive and detailed testing. Detailed recommendation in each of these two areas are identified and discussed in the following sections.

8.1 Improved COSMOS/M Finite Element Modeling

1. Since the total numbers of elements and nodes used for the COSMOS/M modeling of the S–55 tail cone is far below the (advertised) maximum numbers, increased modeling resolution should be attempted. Specific areas for recommended increased modeling resolution are:

    a. removal of beam elements for flanges on the aft located frames.
    b. incorporate shell element modeling on the side longitudinal stiffneners.
    c. include the FEM modeling of the hard–back structure in the implementation of the cantilever mount configuration
    d. include more detailed modeling of the internal appendages.

2. Since the COSMOS/M version used for this study has been superceded by at least one more extensive version, the most up–to–date version of the code should be aquired for future research. In particular, difficulties were experienced with the Lanczos method eigenvalue analysis; these difficulties should be lessened with more advanced versions of the code. Additionally, since the developers of this code, Structural Research and Analysis Corporation, have adopted the policy of providing direct assistance only to holders of valid service contracts, such a service contract should be acquired along with the most advanced version of the code.

3. In the modeling of inboard end regions 2 and 7, separate elastic properties be should be developed for each of the distinct component skin configurations.

4. Alternate boundary conditions defining the cantilever mount configuration should be tried (translational motion restrained, angular motion unrestrained, e.g.).

5. As related to the aircraft finite element modeling in general, attempt to model the properties of the two OH–58A tail cones (one metal semimonocoque, one composite) acquired by the RPI Airframe Component Shake–Test Facility.

8.2 Improved General Finite Element Modeling Techniques

1. Develop new finite element models for general inclusion in *any* finite element modeling analysis (code) for the following elements:

   a a riveted, overlapping skin joint.
   b. modifications of existing elements to include complex stiffnesses (reflecting damping loss factors).
   c. double thickness skins with zero mutual relative shear stresses at the skin interface.

2. Develop methods for efficient implementation of frequency response functions without resorting to modal decomposition. i.e., work directly with mass and stiffness matrices.

3. Implement newly developed methods for structural identification and synthesis (Refs. 19 and 20) in the solution flow.

8.3 Retests of Static Stiffness Characteristics

The S–55 tail cone should be reinstrumented with appropriate strain gage (rosettes) and retested to accomplish the following objectives:

1. Reinstall strain gages at region 2 and 7 locations on both the inside and outside skins at the same locations with improved accuracy in rosette location.

2. Retest with static loads in both the horizontal and vertical directions of greatly increased magnitudes (near the design load of 1000 lbf).

3. Instrument the side stiffeners and appropriate internal members.

8.4 New Dynamic Shake–Tests

A variety of new shake–tests should be attempted in order to resolve uncertainties defined in the present study. Elements of these test should include various combinations of the following items:

1. Make careful weight, c.g. location and complete inertia measurements of the S–55 tail cone.

2. Employ the use of multiple shakers and/or alternate shaker load application locations. This task may require use of special attachment brackets.

3. Make use of accelerometer loactions directly on skin panels. This would require the use of special attachment schemes.

4. Measure the z–components of acceleration in addition to the x– and y–components treated in the present study.

5. Use an advanced form of vibration sensing, such as the use of a laser vibrometer. Such a form of instrumentation would allow the acquisition of many more spacial locations of data. The increased volume of data would define a need for the use of a computer automated data acquisition scheme.

6. Make use of an appropriate modal analysis program package to identify local modes and effective modal damping values for improved Level II correlation.

9.0 REFERENCES

1. "COSMOS/M Finite Element System – User's Manual, Vols. I & II," Structural Research and Analysis Corporation, Santa Monica, CA, 1988.

2. Gordis, J., "A Helicopter Airframe Structural Dynamics Test Facility – Design, Analysis and Experimental Verification," Master's Thesis, Rensselaer Polytechnic Institute, December 1987.

3. Rivello, R. M., *Theory and Analysis of Flight Structures*, McGraw–Hill Book Company, New York, 1969.

4. Jacobsen, M., "Design and Material Verification of an Aluminum Load Cell," Rensselaer Polytechnic Institute Department of Mechanical Engineering, Aeronautical Engineering & Mechanics, Independent Research Report, February 1989.

5. "Quartz Sensors," PCB Piezoelectronics, Inc., Depew, NY, 1984.

6. "Calibration Exciter Type 4292 – Instruction Manual," Brüel & Kjaer Instruments, Inc., Denmark, 1985.

7. "Model 3562A Dynamic Signal Analyzer – Operation Manual," Manual Part no. 03562–9000, Hewlett–Packard Co., Everett, WA, 1985.

8. "Model RTP–650A Instrumentation Video Cassette Data Recorder – Operation Manual," Kyowa Electronic Instruments Co., Ltd. Tokyo, 1986.

9. Dally, J. W. and Riley, W. F., *Experimental Stress Analysis*, McGraw–Hill Book Company, New York, 1978.

10. "HP PC File Utilities," Documentation Part No. 5959–5736, Hewlett–Packard Co., Everett, WA, 1989.

11. Hefner, R. E. and Gordis, J., "Detailed Description of S–55 Helicopter Tail Cone Finite Element Modeling," RPI Rotorcraft Technology Center Report no. D–91–2, 1991.

12. "Product Reference Guide," general catalog, Edgecomb Metals, Inc., So. Portland, Maine, (latest version, circe 1991).

13. "Stocks & Services – Steel, Aluminum, Plastics, Machinery, processing Services", general catalog, Joseph T. Ryerson & Son, Inc., Jersey City, N.J., 1976.

14. Baumeister, T. and Marker, L. S. (eds.), *Standard Handbook for Mechanical Engineers*, Seventh Edition, McGraw Hill Book Company, New York, 1967.

15. Beer, F. P., and Johnston, E. R., *Mechanics of Materials*, McGraw–Hill Book Company, New York, 1981.

16. Tapley, B. D. and Poston, T. R., (eds), *Esbach's Handbook of Engineering Fundamentals*, Fourth Edition, John Wiley and Sons, New York, 1990.

17. Hefner, R. E., "Experimental and Analytical Correlation Study of the Static Strain and Dynamic Frequency Response Characteristics of a Metal Semimonocoque Helicopter Tail Cone", Masters Thesis, Rensselaer Polytechnic Institute, 1991.

18. Ibrahim, S. R. & Mikulcik, E. C., "A Method for the Direct Identification of Vibration Parameters from the Free Response," *Shock and Vibration Bulletin*, no. 51, Part 3, 1981.

19. Gordis, J. H., "On Structural Syntheses and Identification in the Frequency Domain," Doctoral dissertation, Rensselaer Polytechnic Institute, Troy New York, August, 1990.

20. Gordis, J. H., "A Frequency Domain theory for Structural Identification," Lichten Award paper, Proceedings of the 46th Annual Forum, American Helicopter Society, Washington D.C., May 1990.

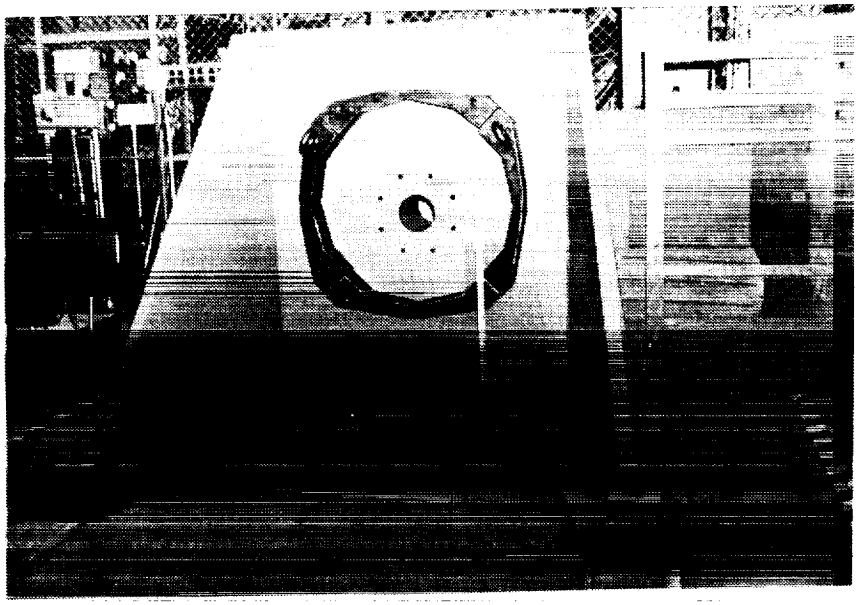

Figure 1. View of hardback structure mounted to vibration pad in the RPI Airframe Component Shake–Test Facility

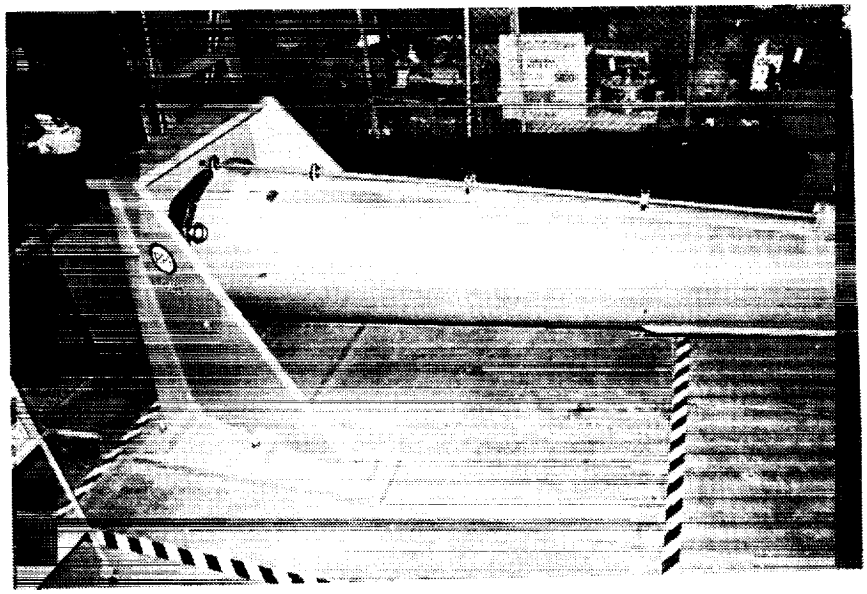

Figure 2. View of S–55 tail cone installed on hard–back structure

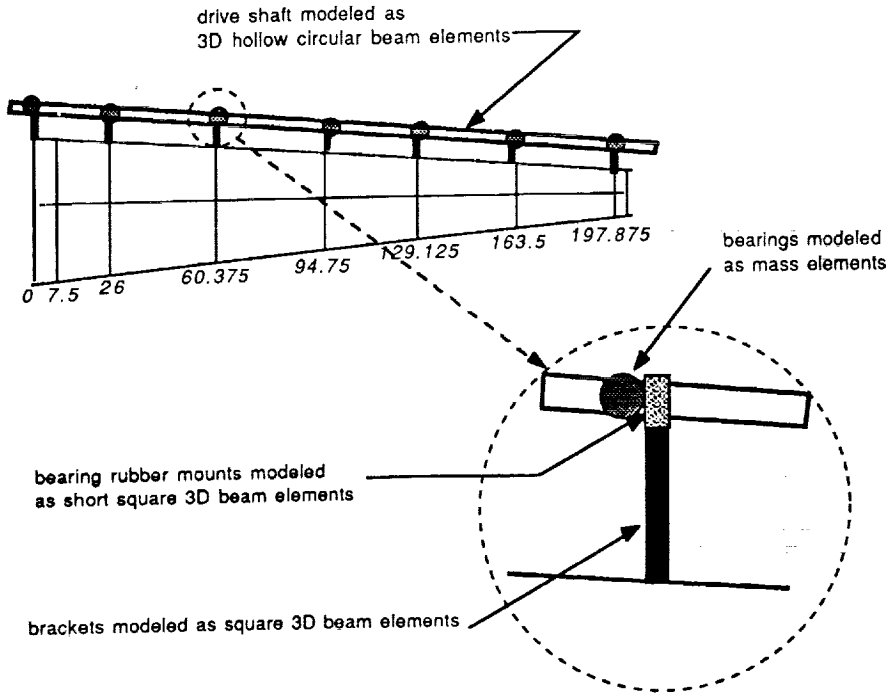

Figure 3. Pictorial representation of the S–55 tail rotor drive shaft

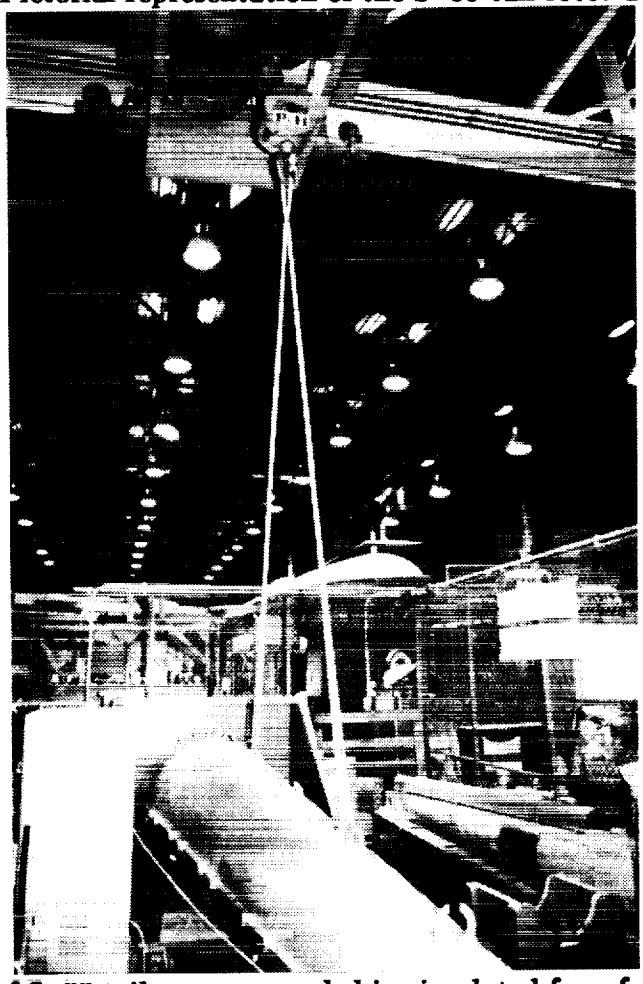

Figure 4. View of S–55 tail cone suspended in simulated free–free configuration

ORIGINAL PAGE
BLACK AND WHITE PHOTOGRAPH

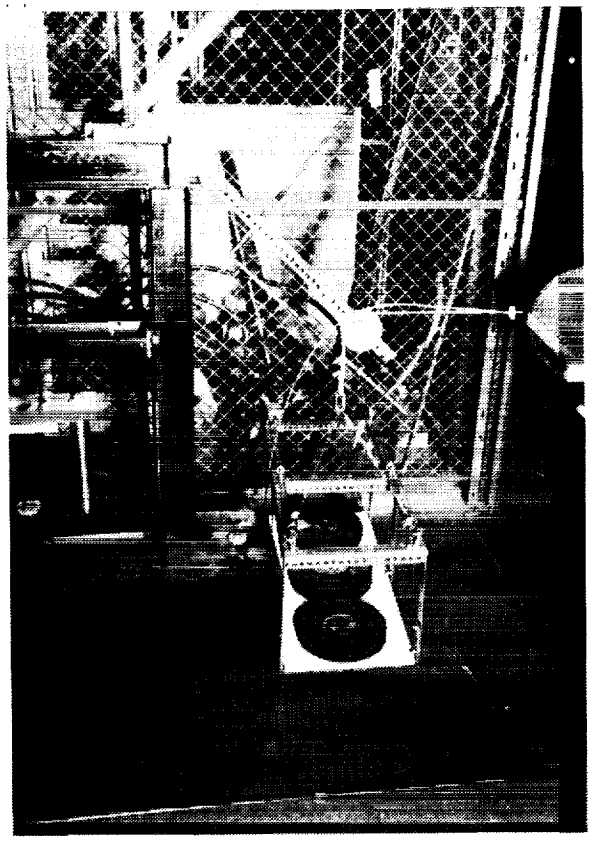

Figure 5. Static load application weight platform

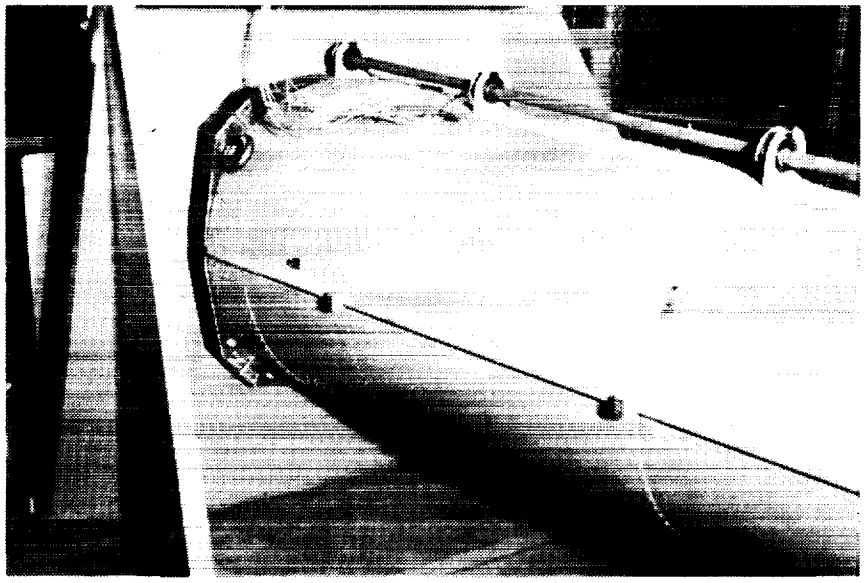

Figure 6. View of strain gage installation and typical accelerometer mounting blocks attached to lateral stiffener

Figure 8. View of floor shaker location and rigid oblique stinger assembly

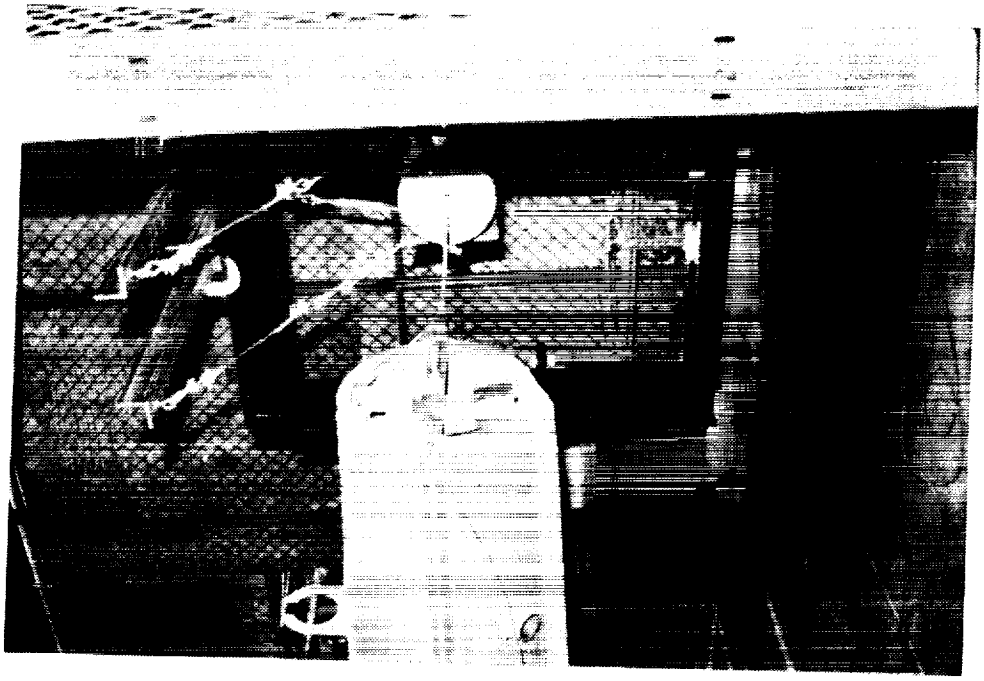

Figure 7. View of horizontal shaker mounting and tension stinger assembly

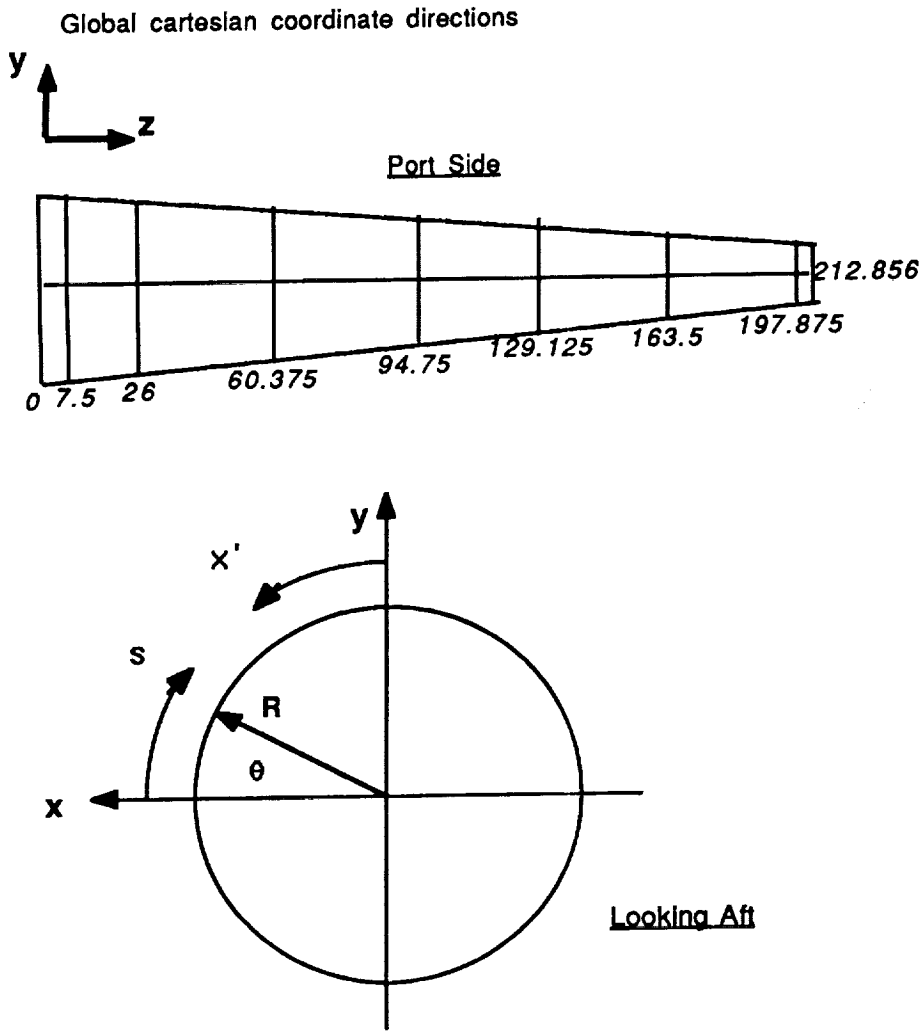

Figure 9. Definitions of global cartesean and cylindrical coordinate systems

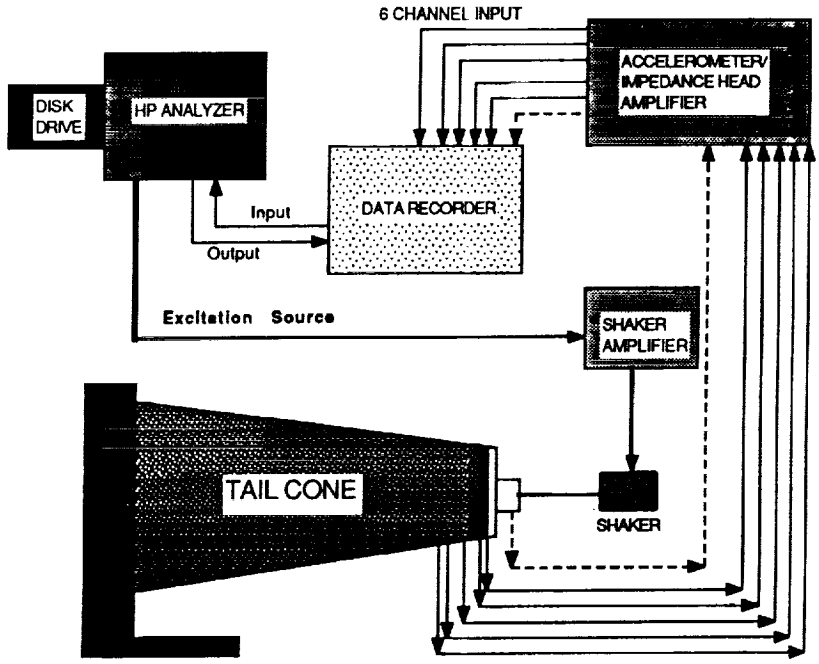

Figure 10 Schematic of instrumentation set–up used for shake–tests

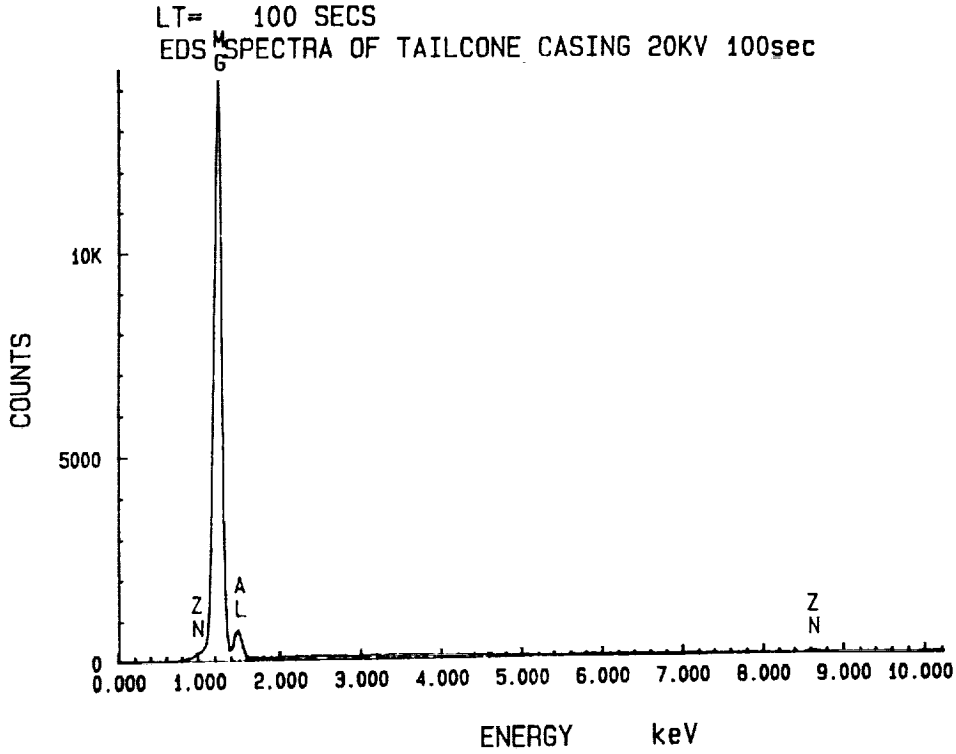

Figure 11. Scanning microscope spectrum analysis of end casing material

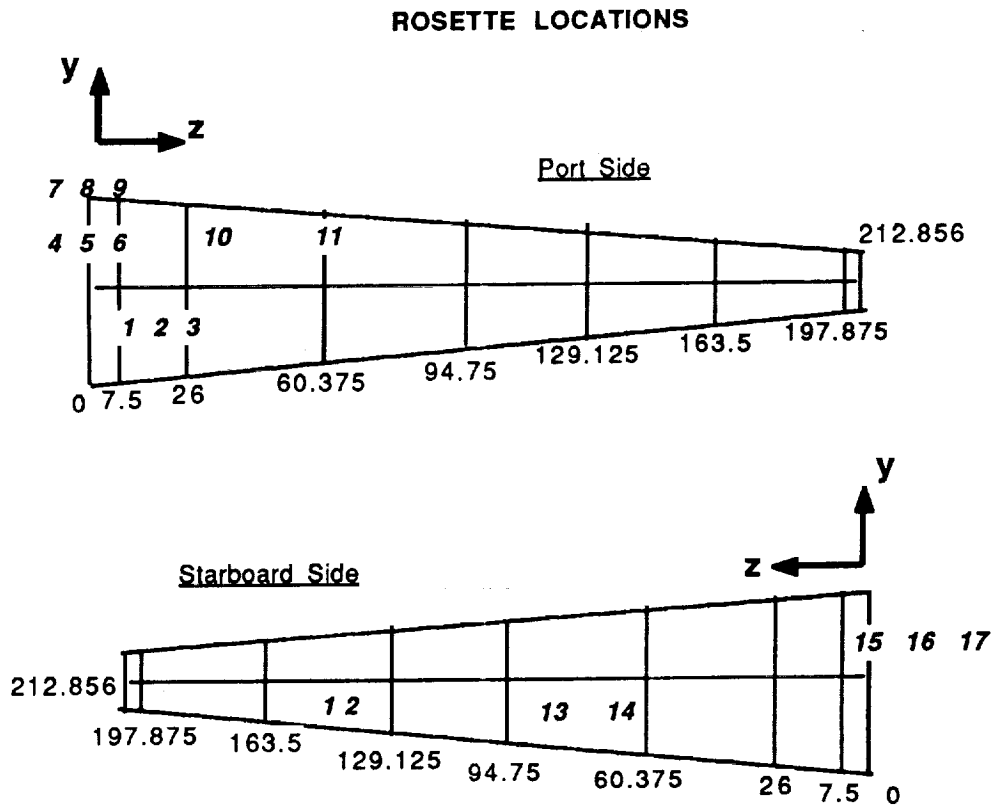

Figure 12. Pictorial views of strain gage locations

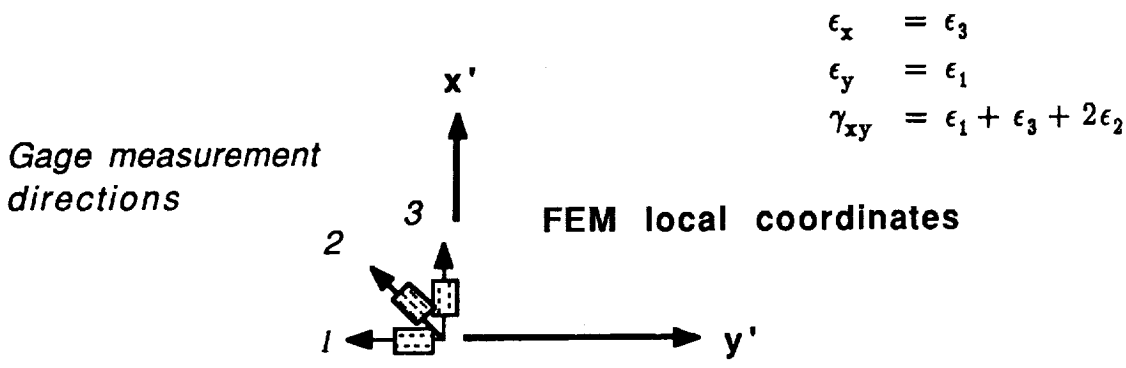

Figure 13a. Mounting orientations of rosette strain gage numbers 1–3, 10 & 11

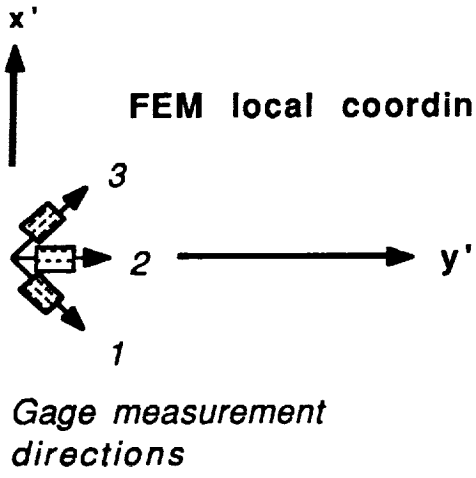

$$\epsilon_x = \epsilon_1 + \epsilon_3 - \epsilon_2$$
$$\epsilon_y = \epsilon_2$$
$$\gamma_{xy} = \epsilon_3 - \epsilon_1$$

Figure 13b. Mounting orientations of rosette strain gage numbers 4–7 & 9

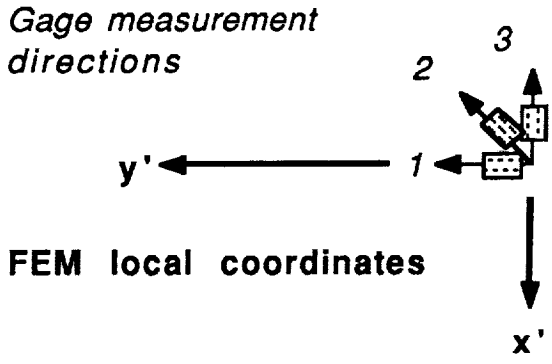

$$\epsilon_x = \epsilon_3$$
$$\epsilon_y = \epsilon_1$$
$$\gamma_{xy} = \epsilon_1 + \epsilon_3 + 2\epsilon_2$$

Figure 13c. Mounting orientations of rosette strain gage numbers 12, 13 & 14

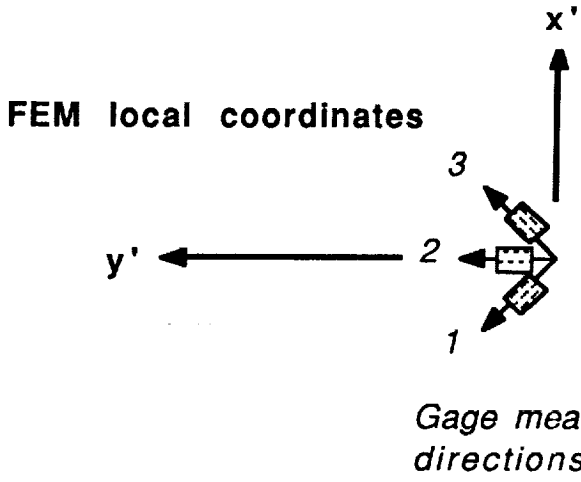

$$\epsilon_x = \epsilon_1 + \epsilon_3 - \epsilon_2$$
$$\epsilon_y = \epsilon_2$$
$$\gamma_{xy} = \epsilon_3 - \epsilon_1$$

Figure 13d. Mounting orientations of rosette strain gage numbers 15–17

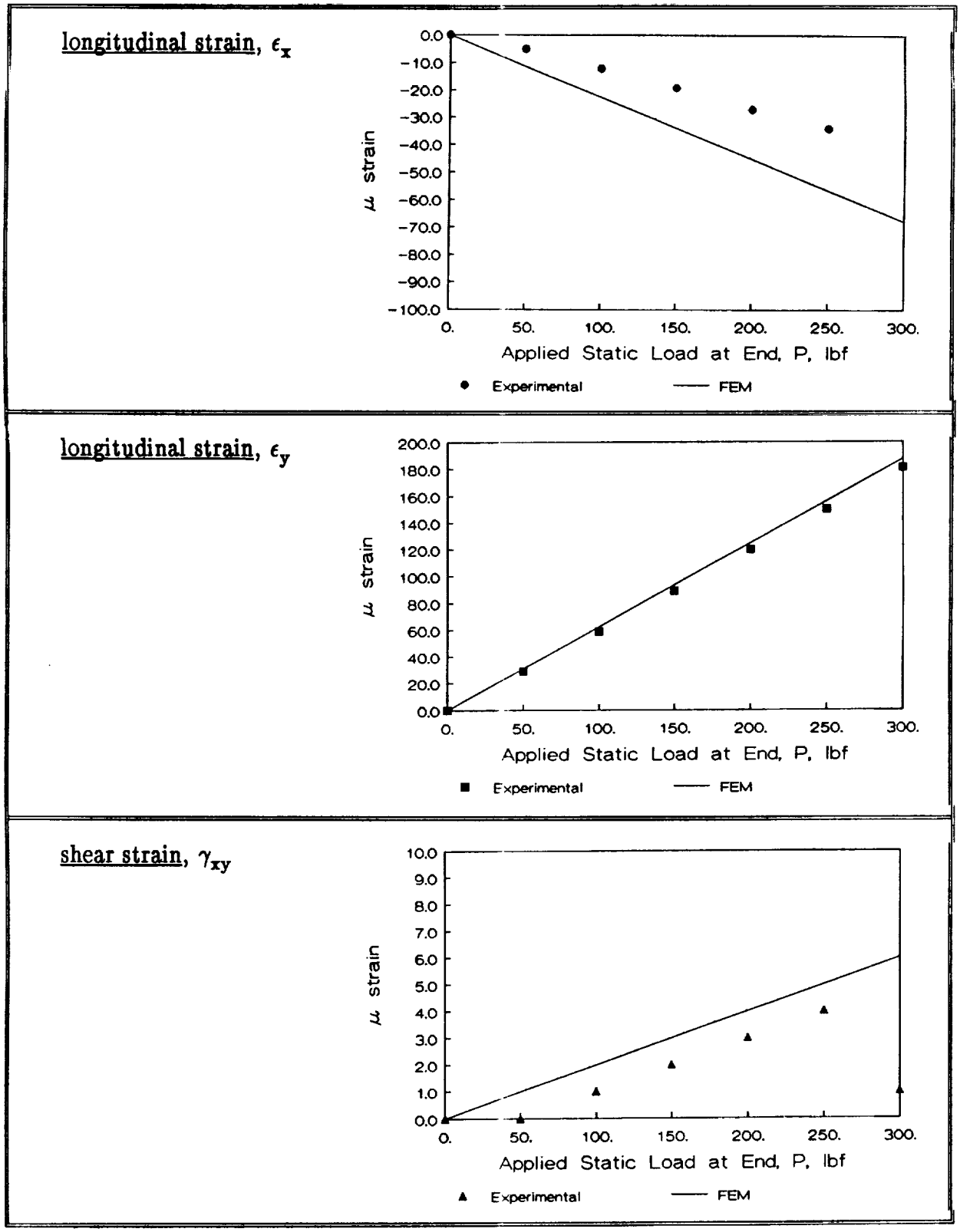

Figure 14a. Comparison of experimental and analytic strains due to static lateral load, rosette location no. 1

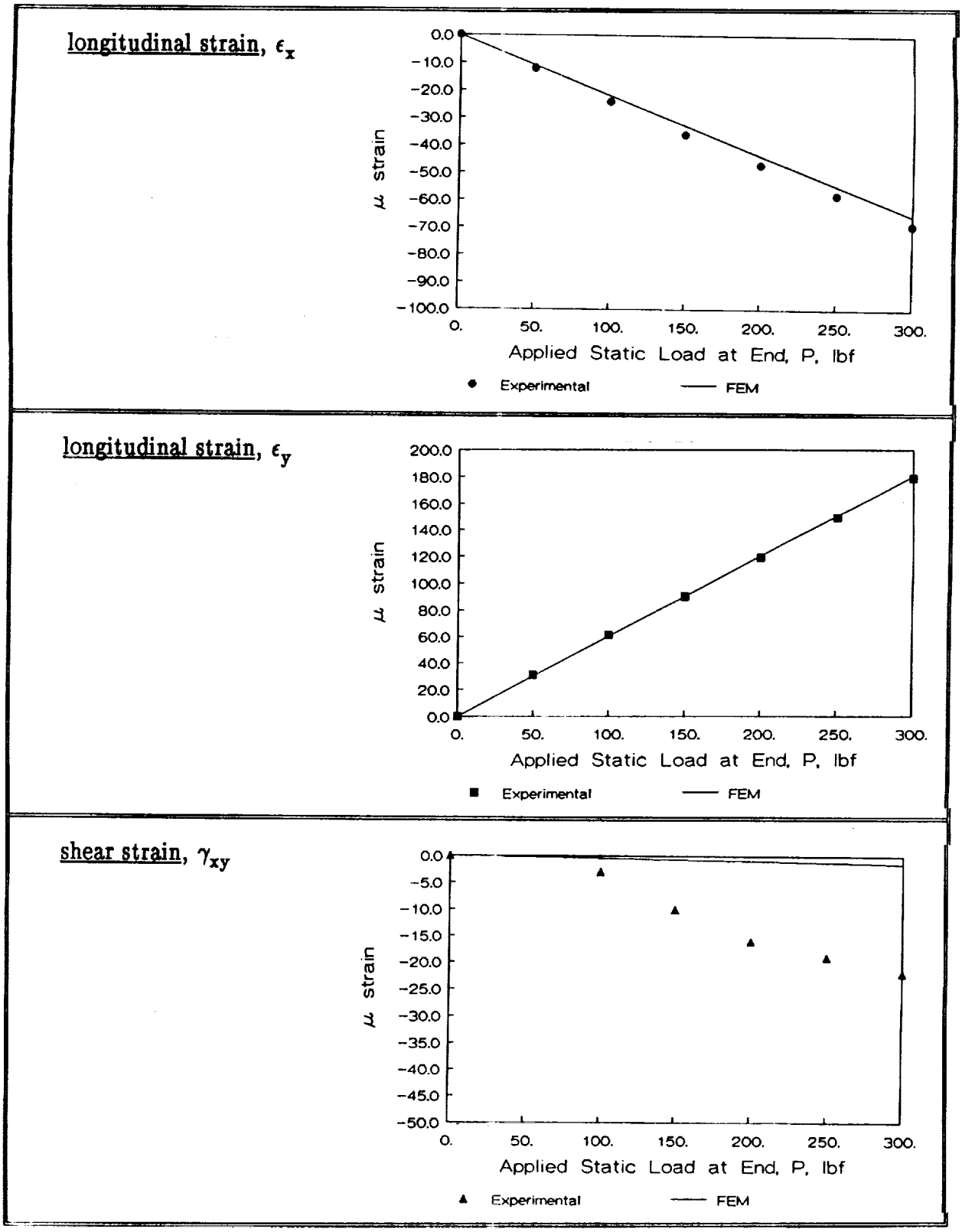

Figure 14b. Comparison of experimental and analytic strains due to static lateral load, rosette location no. 2

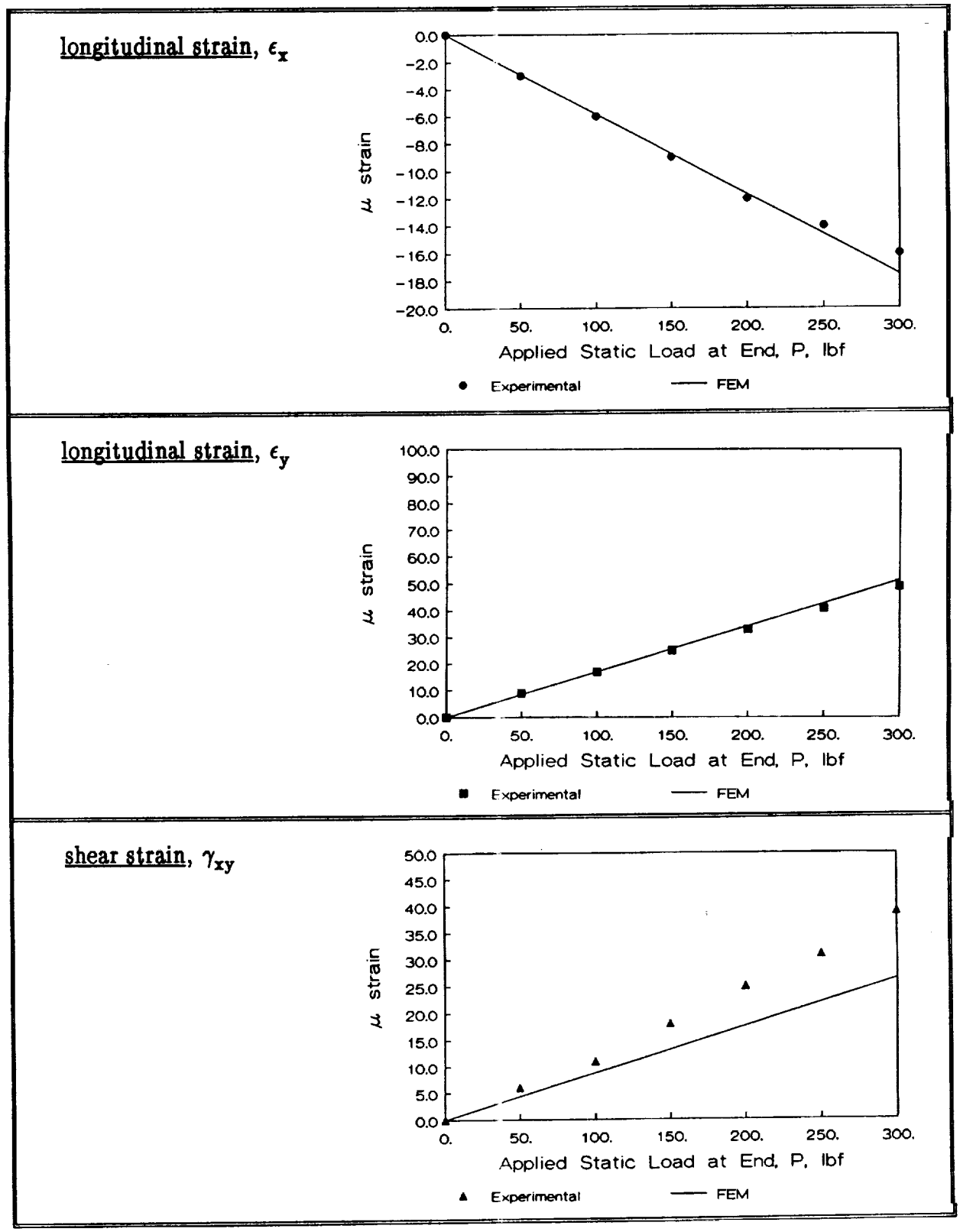

Figure 14c. Comparison of experimental and analytic strains due to static lateral load, rosette location no. 10

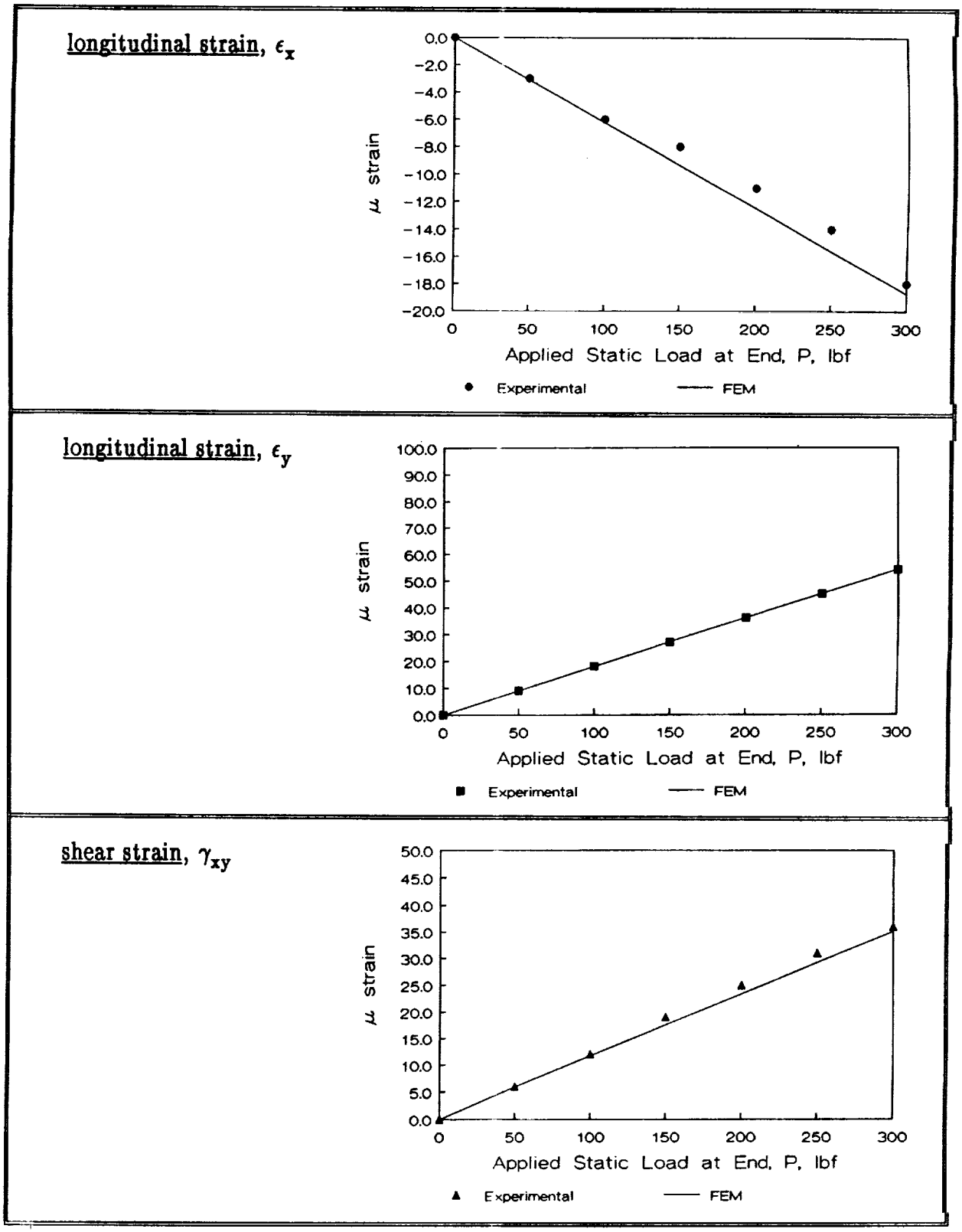

Figure 14d. Comparison of experimental and analytic strains due to static lateral load, rosette location no. 11

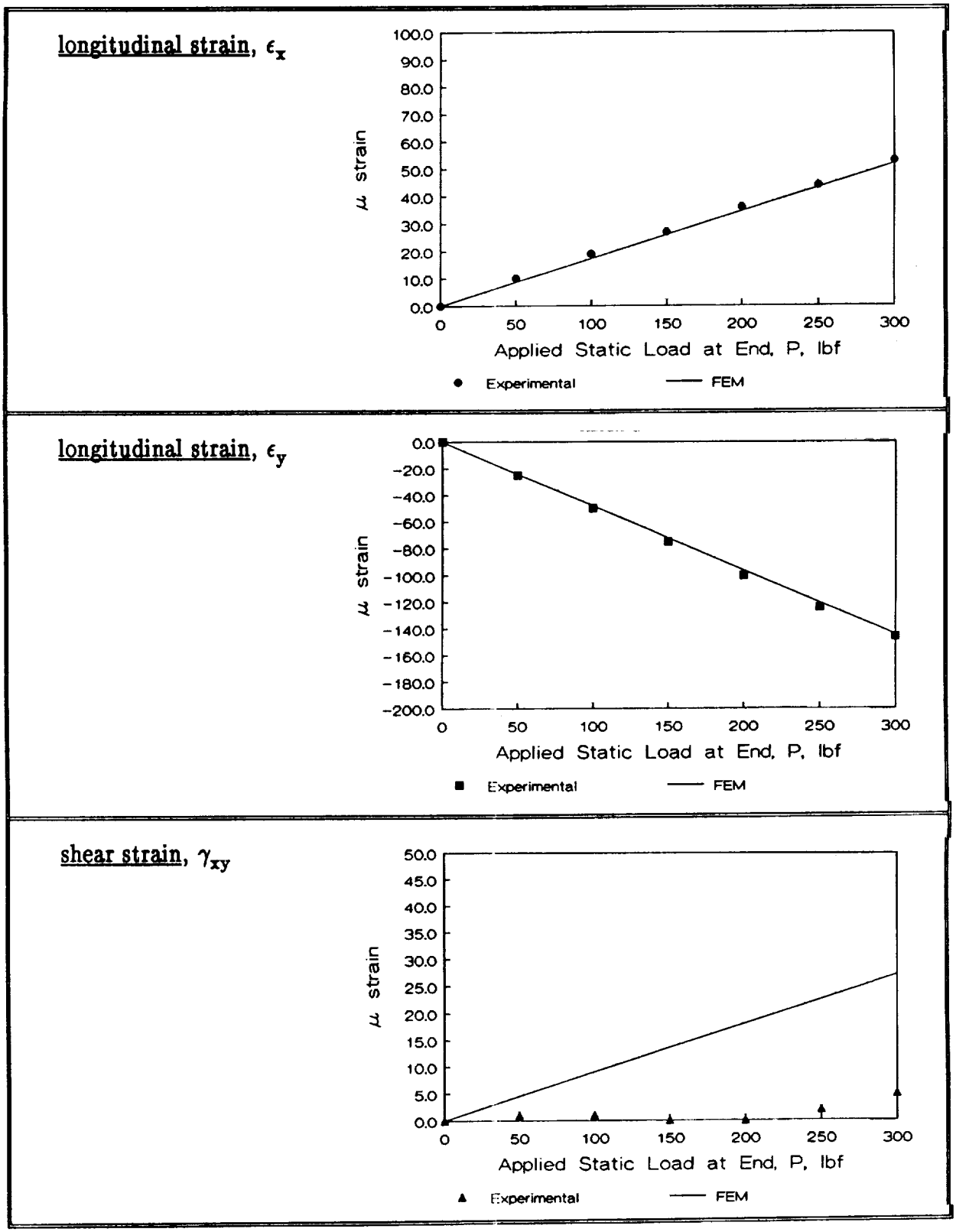

Figure 14e. Comparison of experimental and analytic strains due to static lateral load, rosette location no. 12

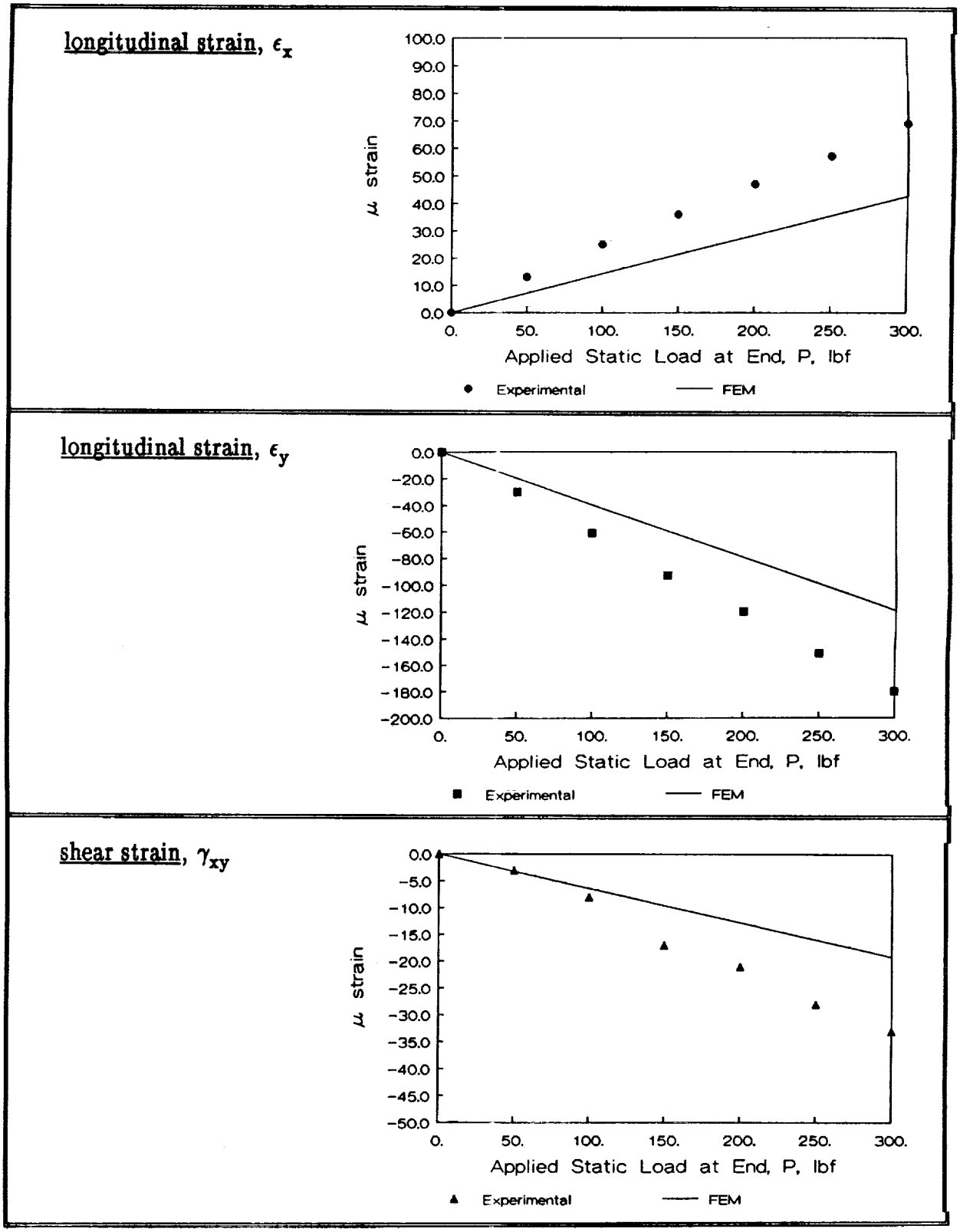

Figure 14f. Comparison of experimental and analytic strains due to static lateral load, rosette location no. 14

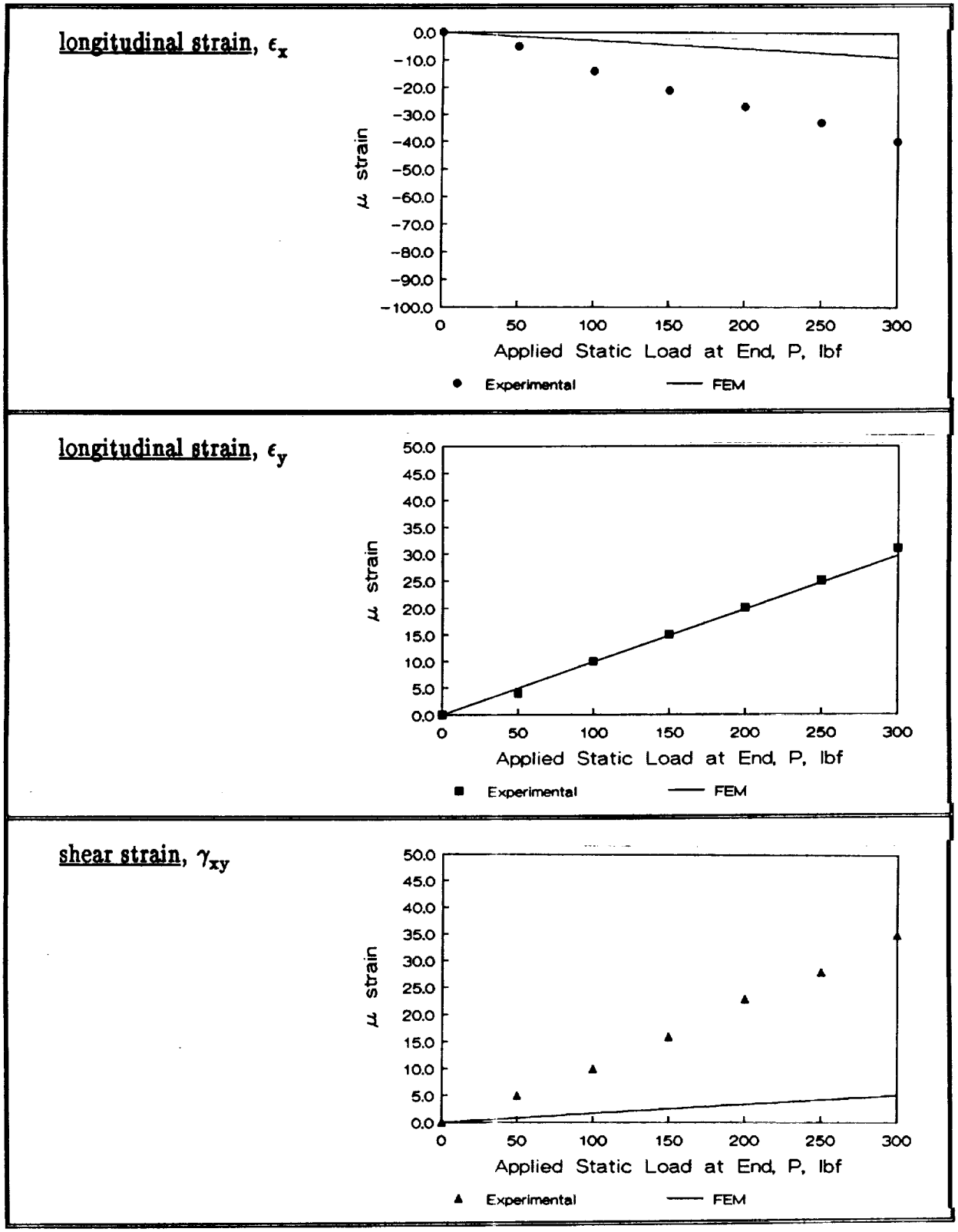

Figure 14g. Comparison of experimental and analytic strains due to static lateral load, rosette location no. 4

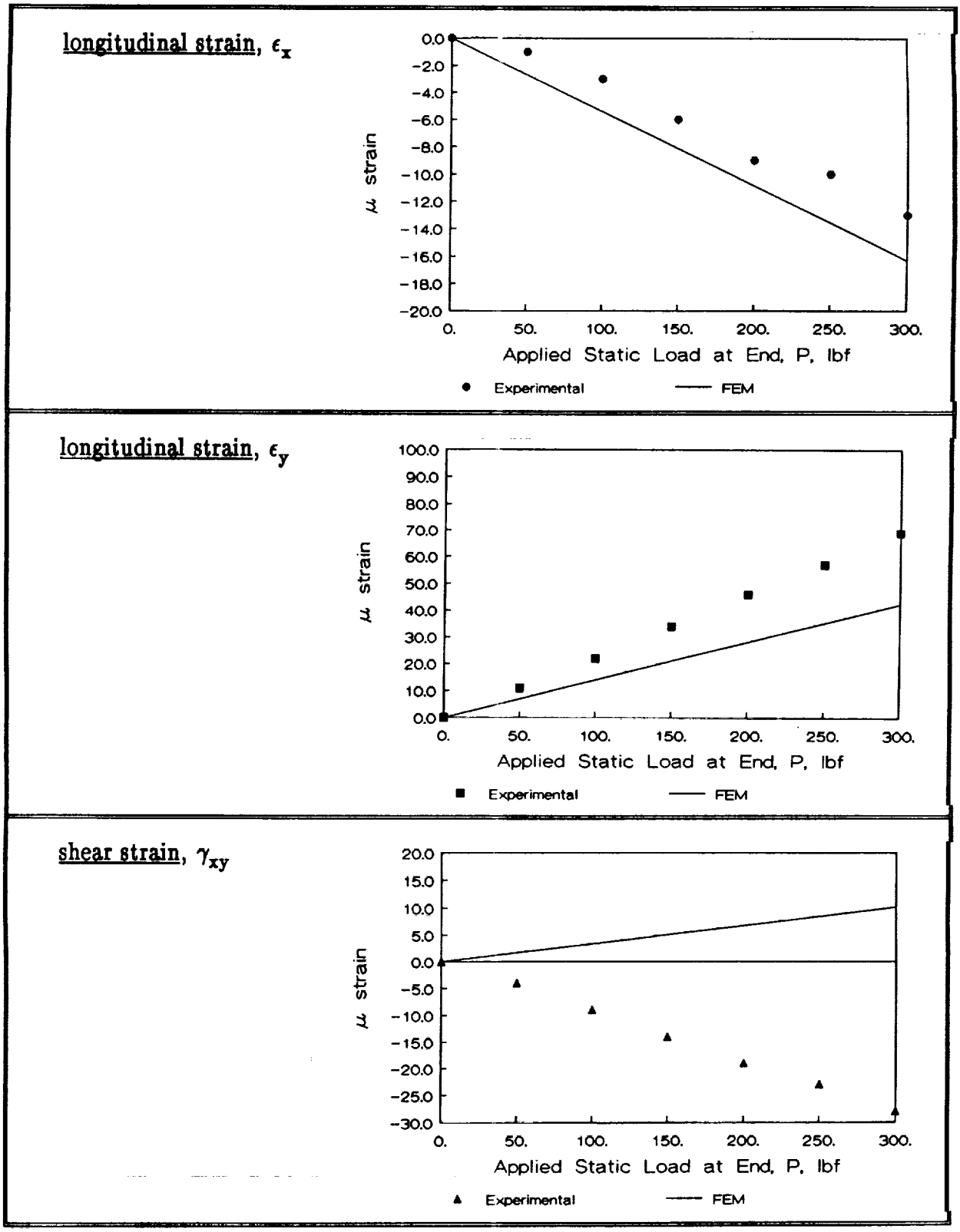

Figure 14h. Comparison of experimental and analytic strains due to static lateral load, rosette location no. 5

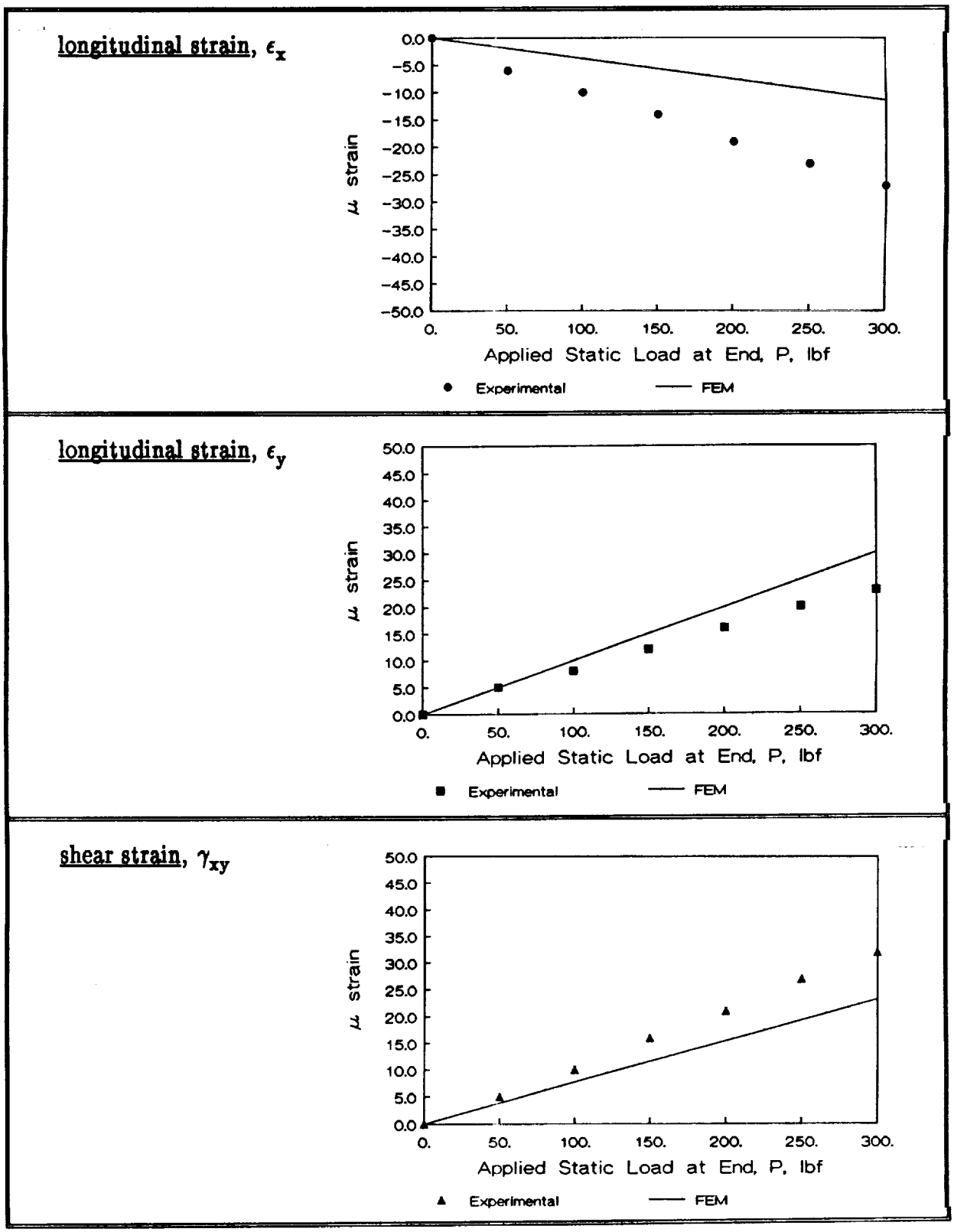

Figure 14i. Comparison of experimental and analytic strains due to static lateral load, rosette location no. 6

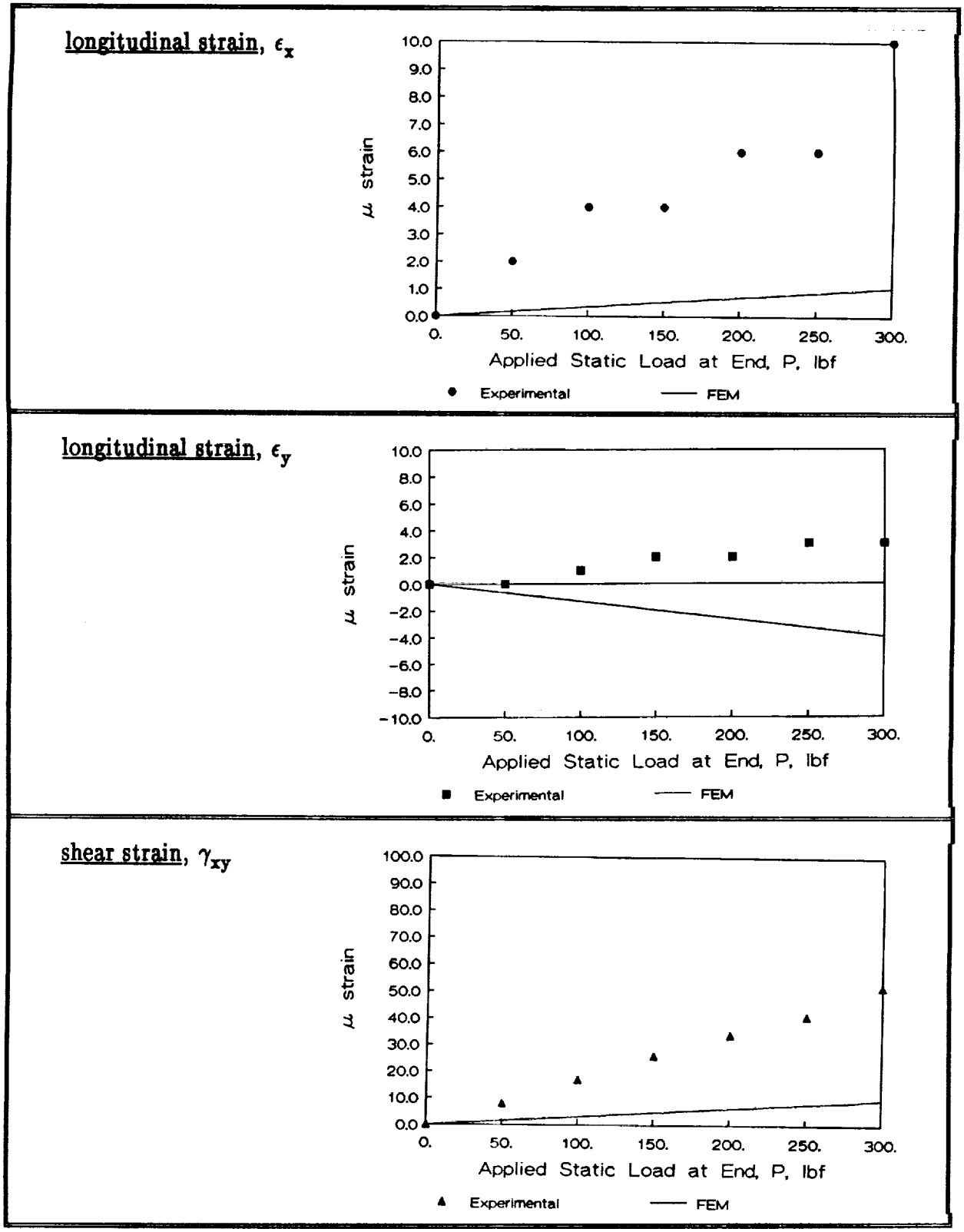

Figure 14j. Comparison of experimental and analytic strains due to static lateral load, rosette location no. 7

C-2

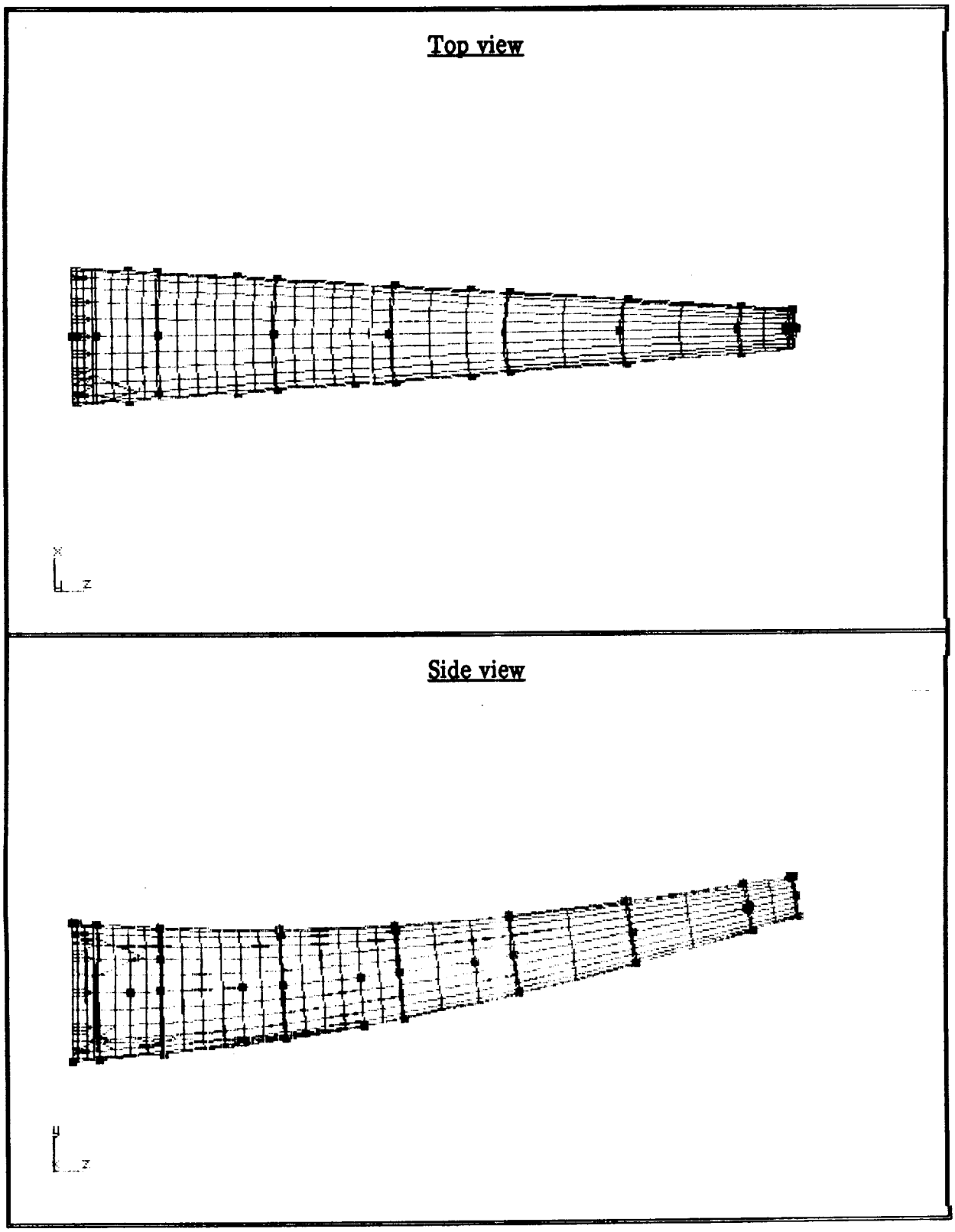

Figure 15a. Graphical depiction of analytical normal mode no. 1 (f_1 = 18.060 Hz), cantilevered (no drive shaft) configuration

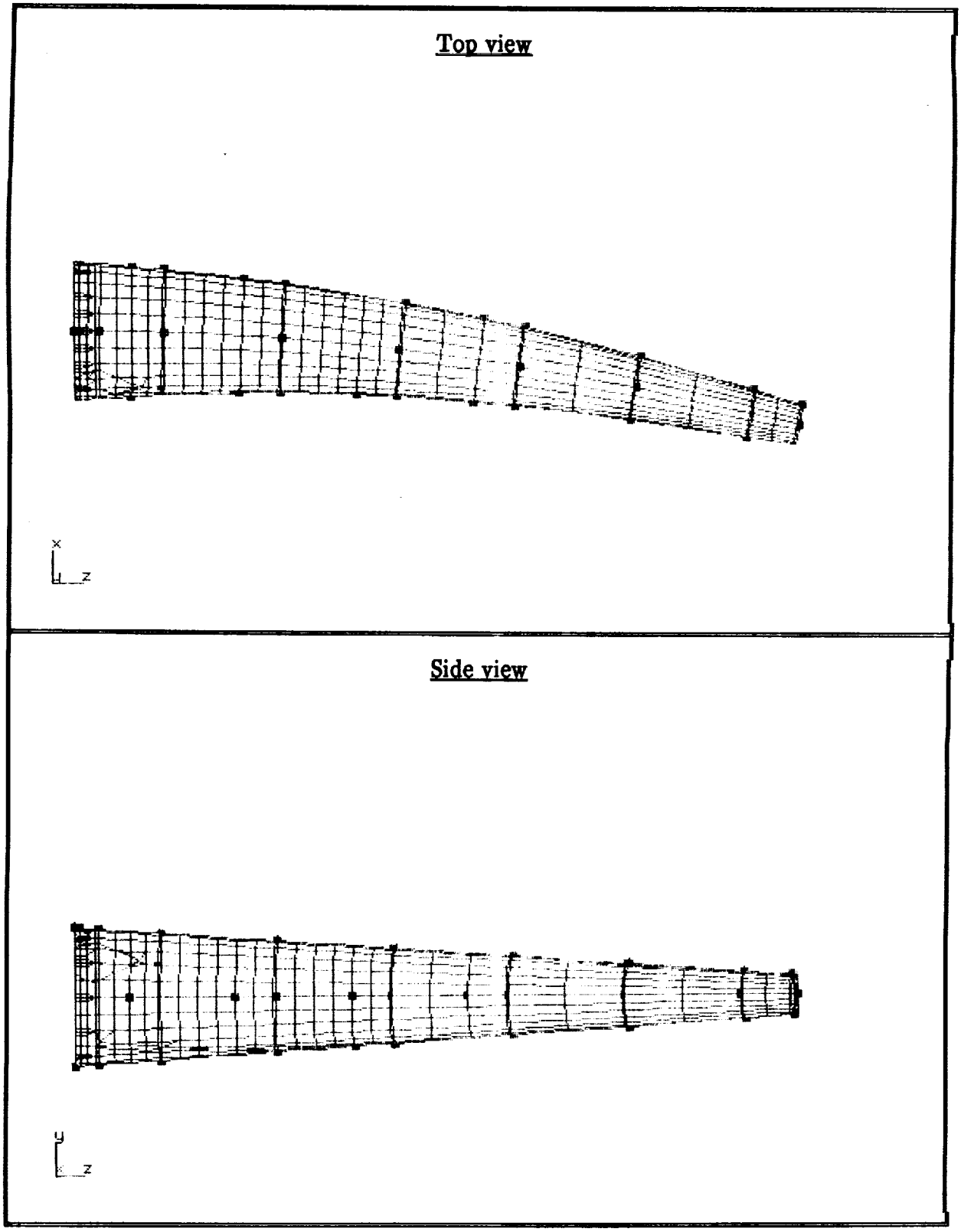

Figure 15b. Graphical depiction of analytical normal mode no. 2 ($f_2 = 19.506$ Hz), cantilevered (no drive shaft) configuration

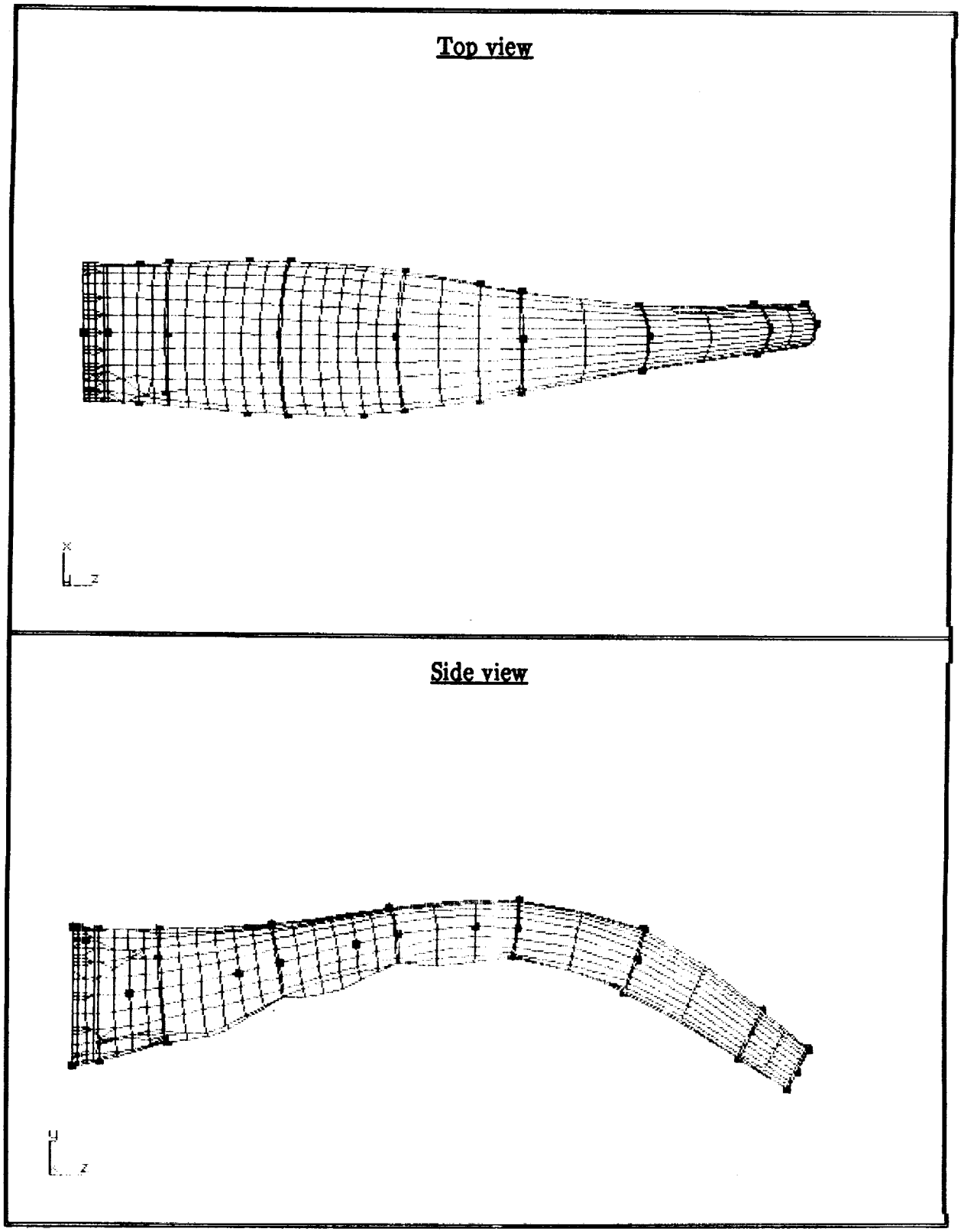

Figure 15c. Graphical depiction of analytical normal mode no. 4 ($f_4 = 83.133$ Hz), cantilevered (no drive shaft) configuration

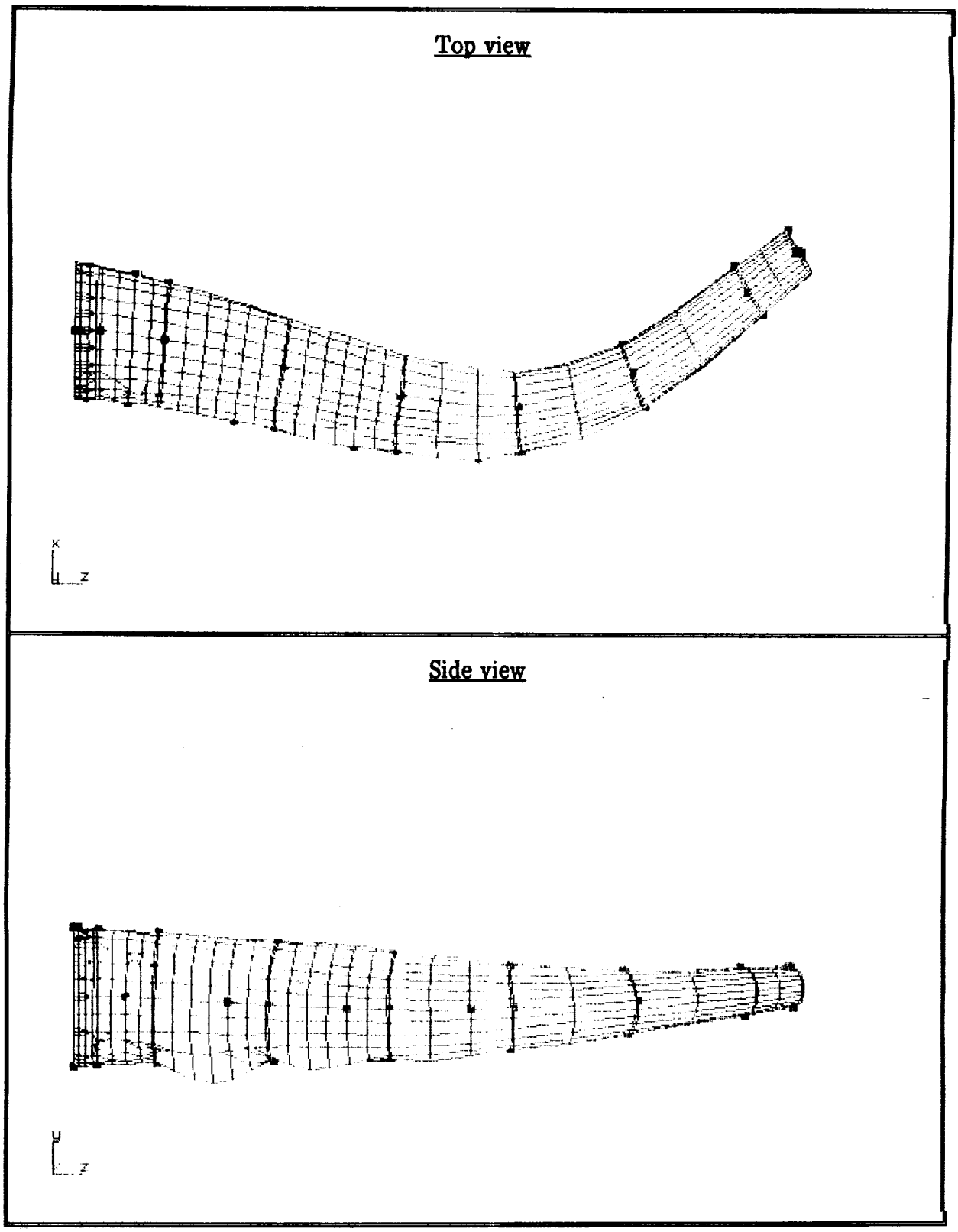

Figure 15d. Graphical depiction of analytical normal mode no. 5 ($f_5 = 86.364$ Hz), cantilevered (no drive shaft) configuration

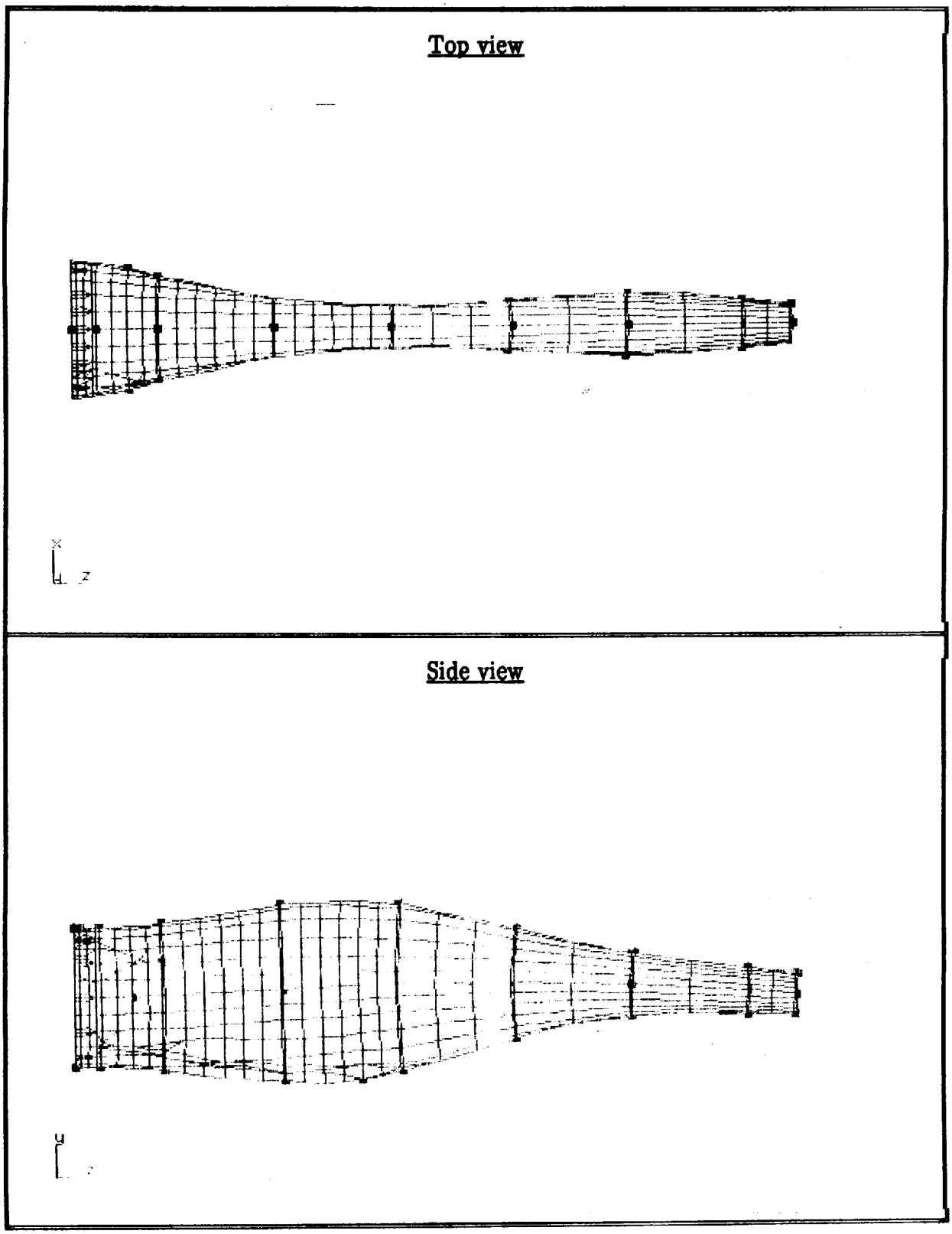

Figure 15e. Graphical depiction of analytical normal mode no. 8 (f_8 = 103.589 Hz), cantilevered (no drive shaft) configuration

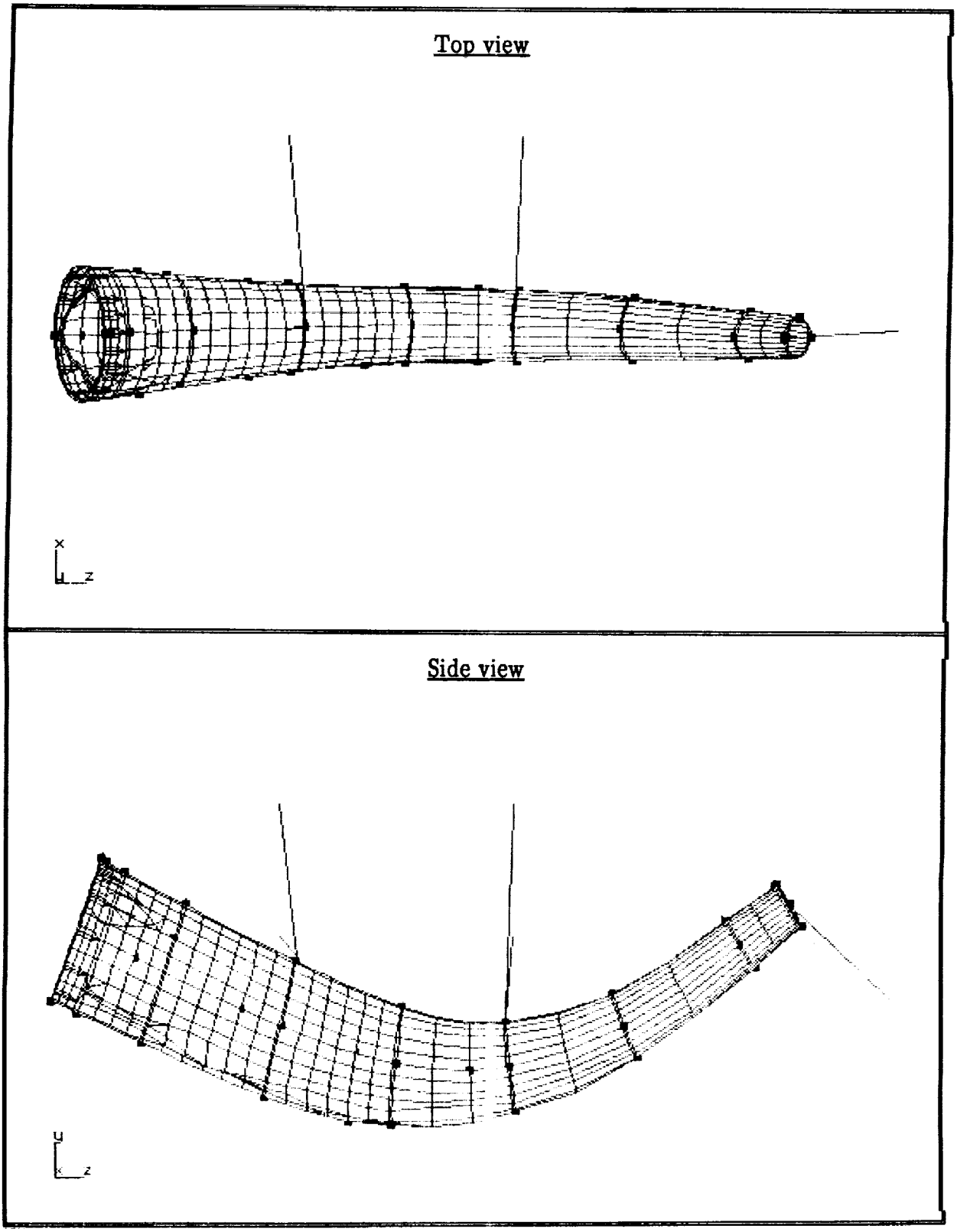

Figure 16a. Graphical depiction of analytical normal mode no. 7 ($f_7 = 70.442$ Hz), simulated free–free configuration

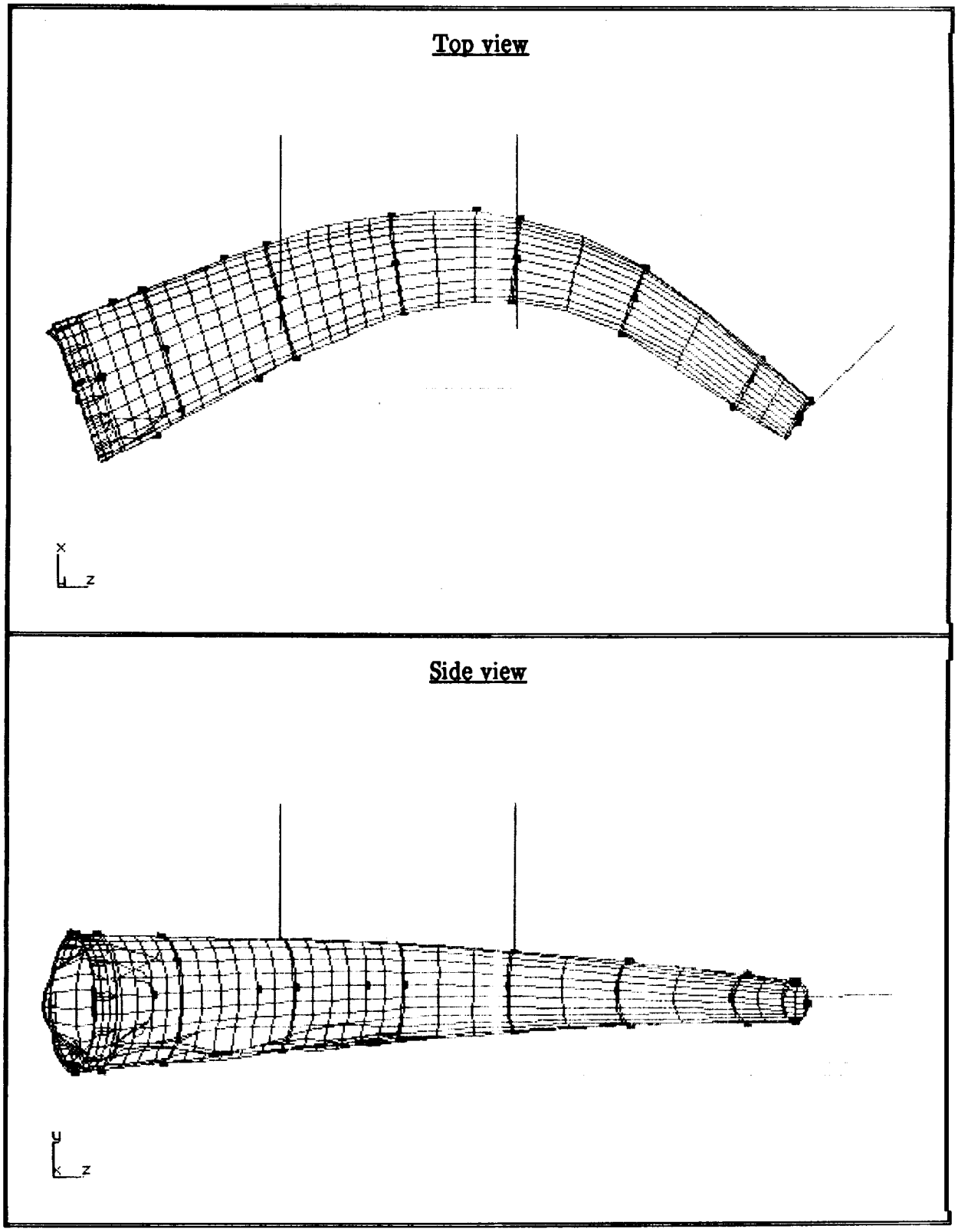

Figure 16b. Graphical depiction of analytical normal mode no. 8 (f_8 = 74.683 Hz), simulated free–free configuration

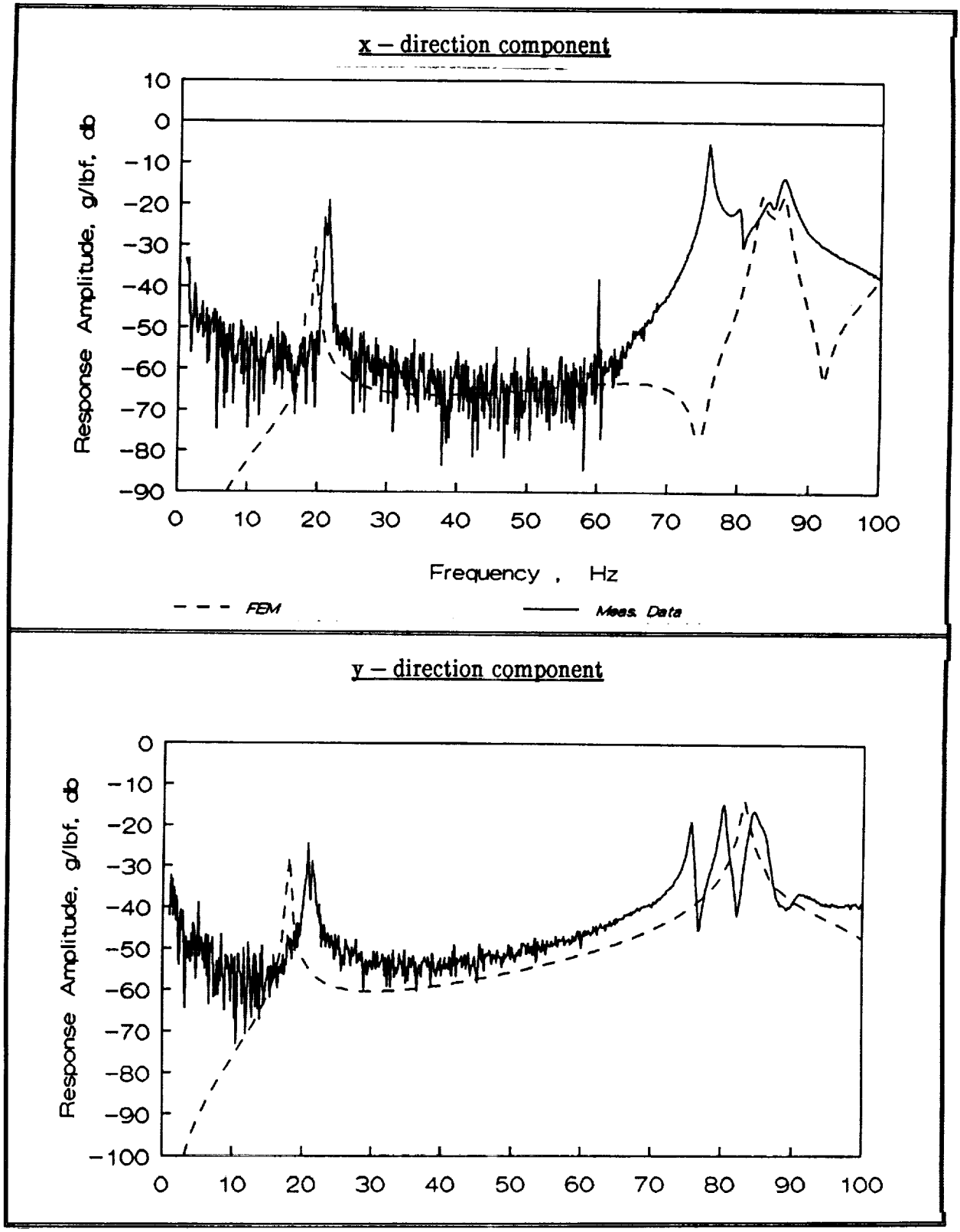

Figure 17a. Comparison of experimental and analytical frequency response functions, cantilevered (no shaft) configuration, accelerometer location 2R

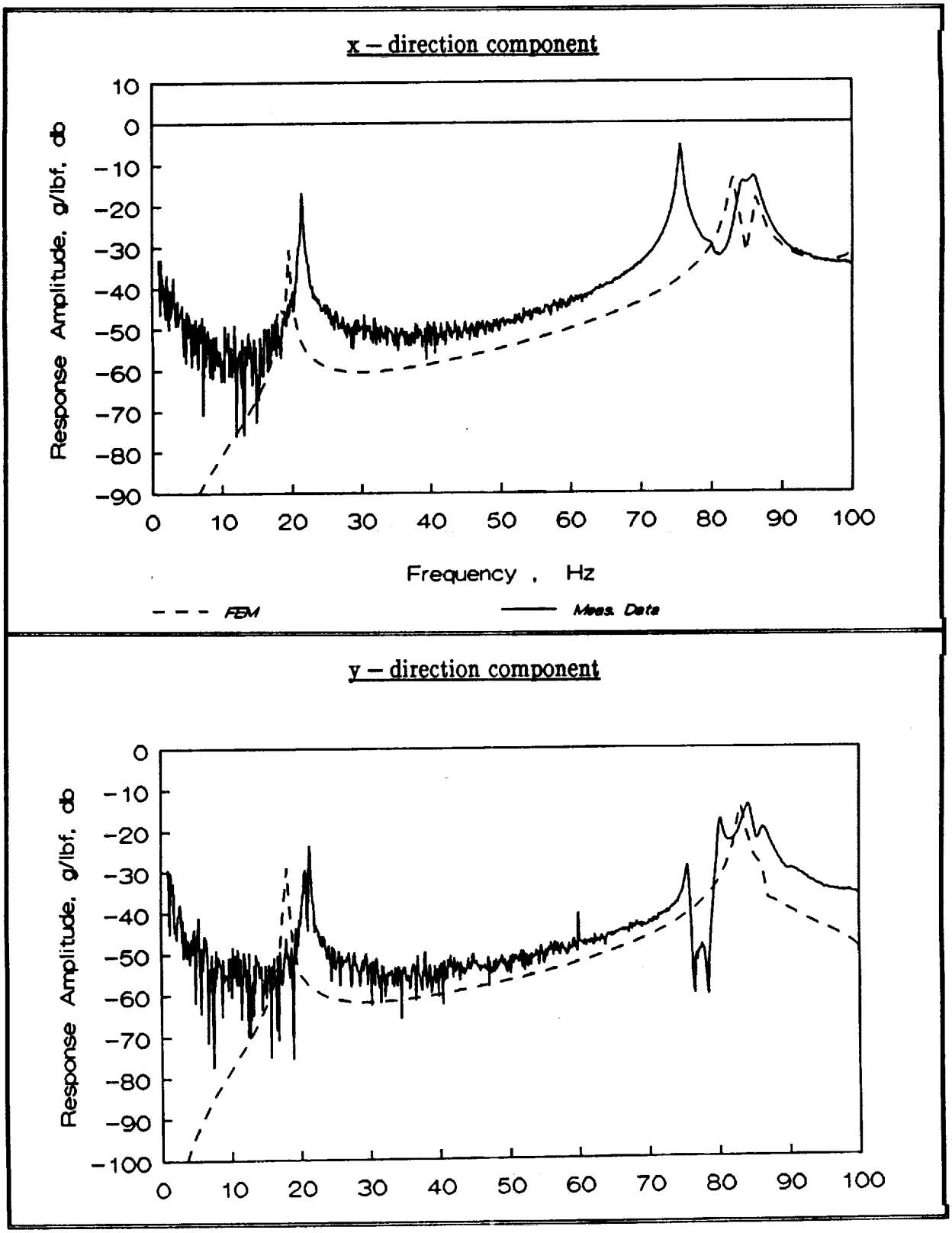

Figure 17b. Comparison of experimental and analytical frequency response functions, cantilevered (no shaft) configuration, accelerometer location 2L

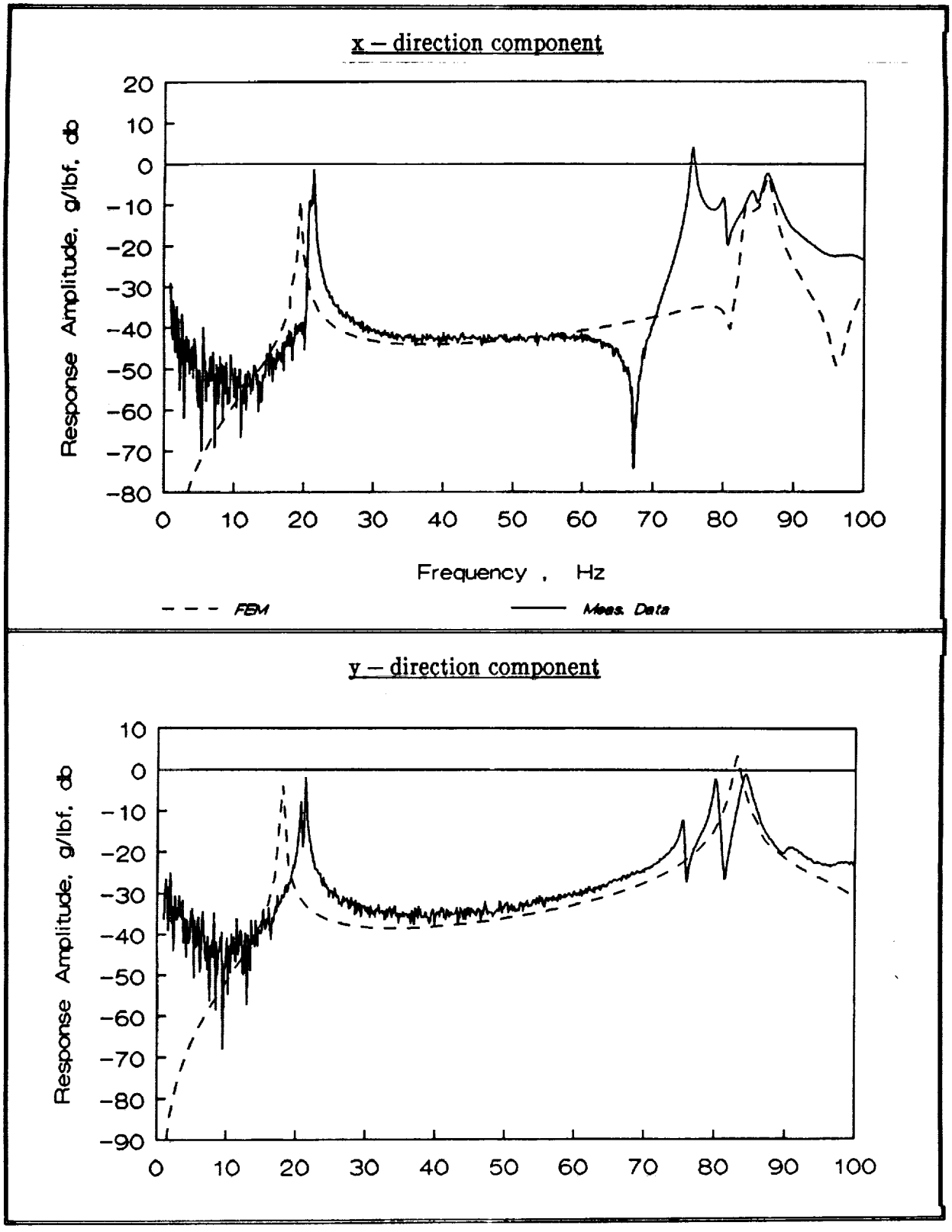

Figure 17c. Comparison of experimental and analytical frequency response functions, cantilevered (no shaft) configuration, accelerometer location 6R

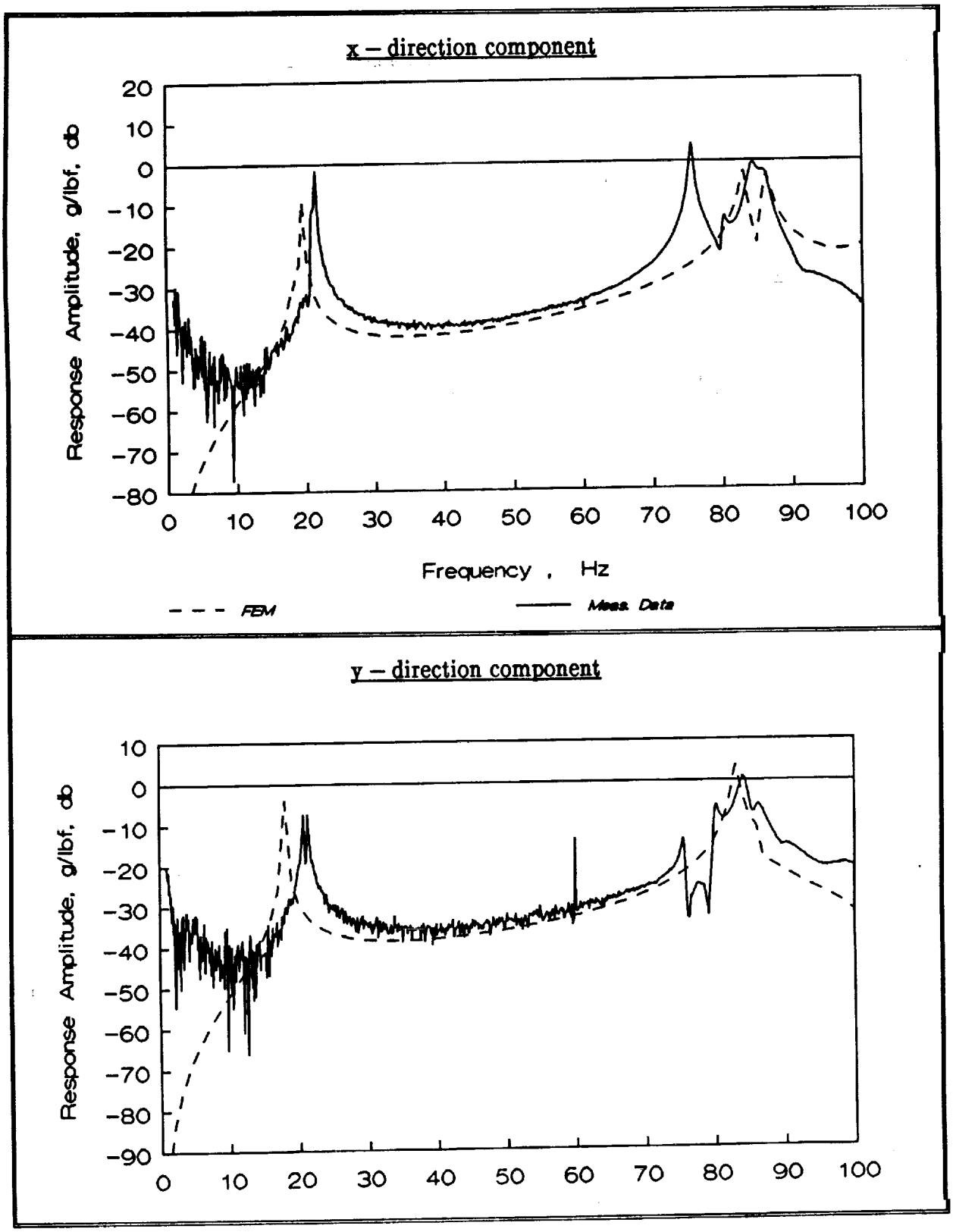

Figure 17d. Comparison of experimental and analytical frequency response functions, cantilevered (no shaft) configuration, accelerometer location 6L

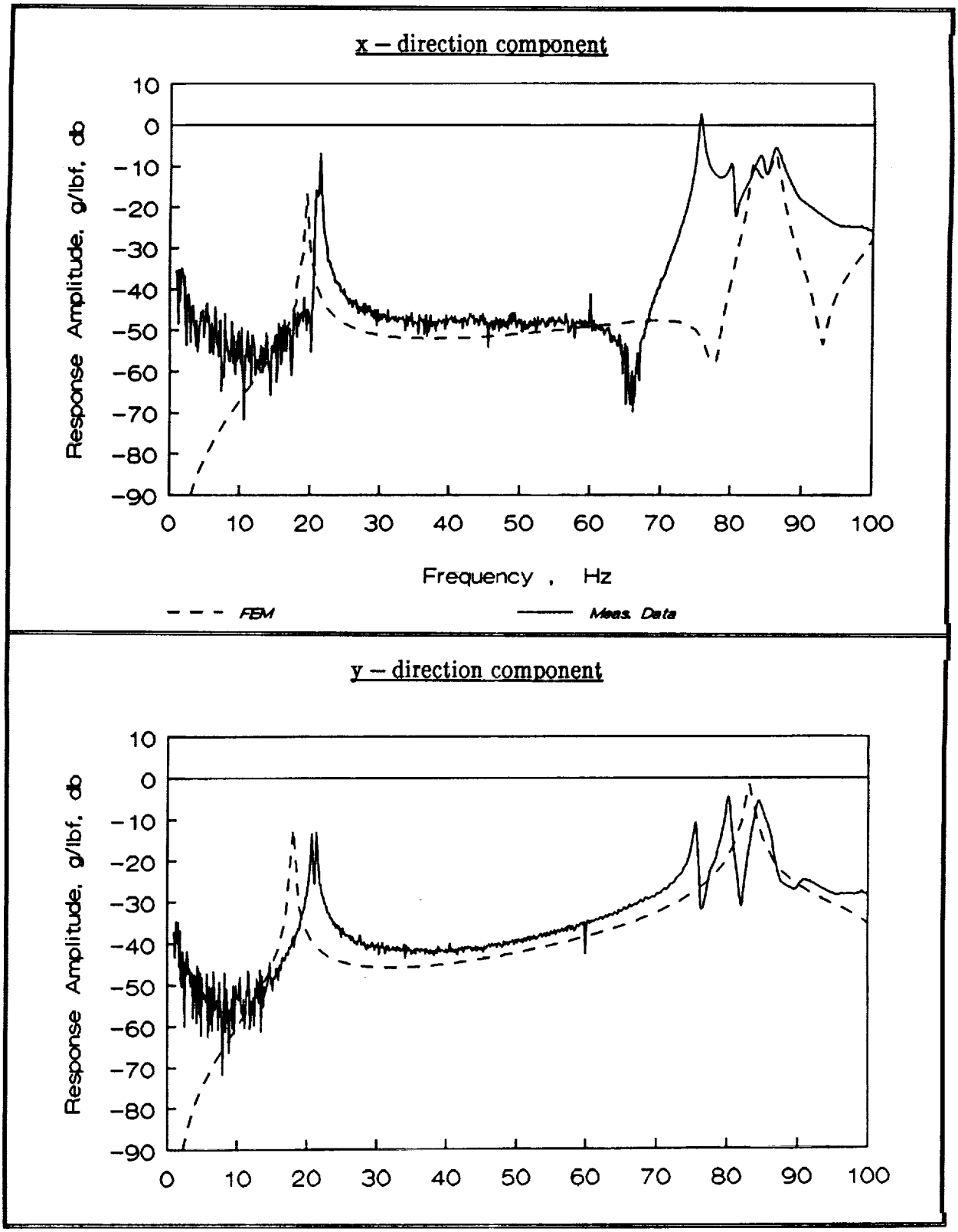

Figure 17e. Comparison of experimental and analytical frequency response functions, cantilevered (no shaft) configuration, accelerometer location 4R

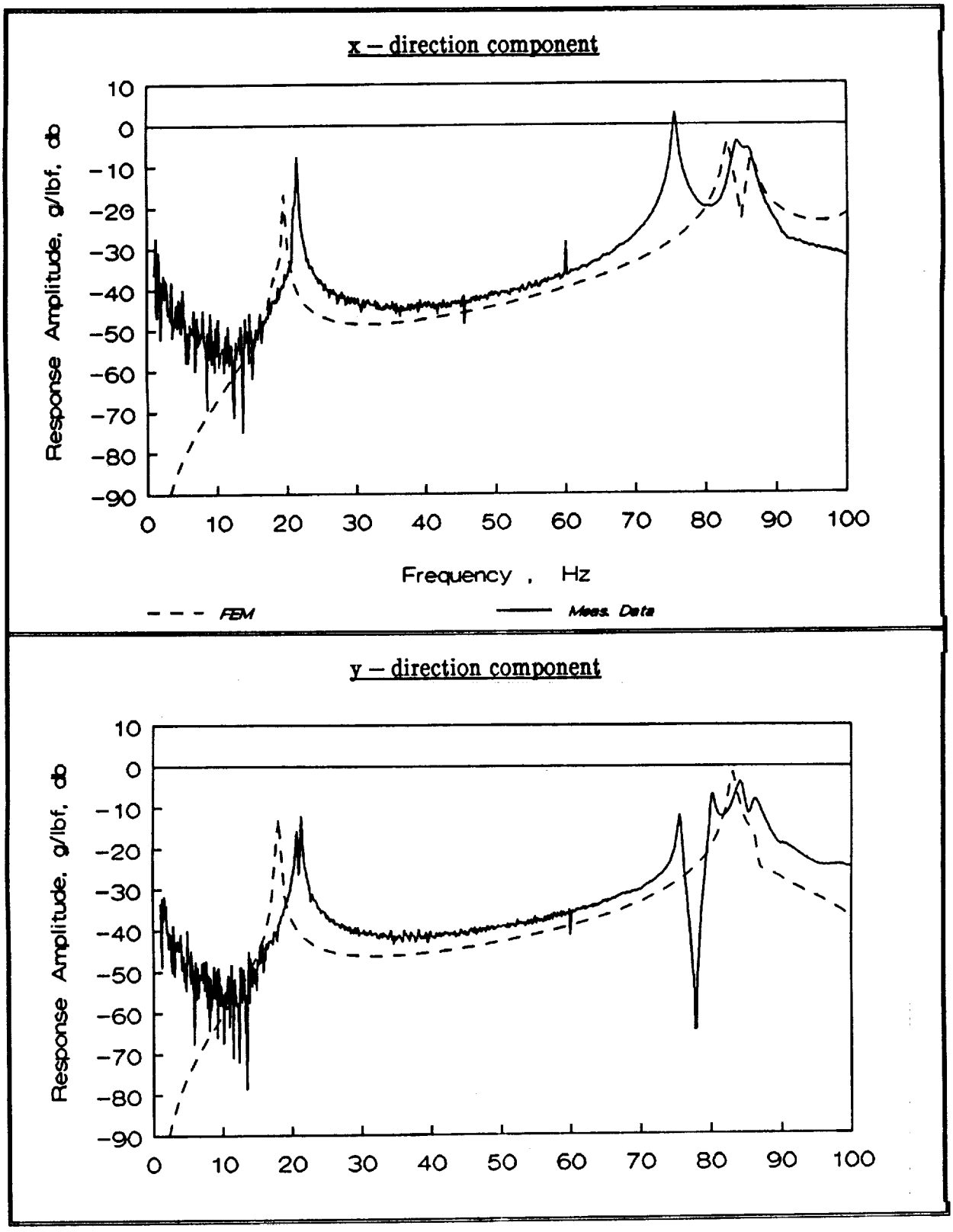

Figure 17f. Comparison of experimental and analytical frequency response functions, cantilevered (no shaft) configuration, accelerometer location 4L

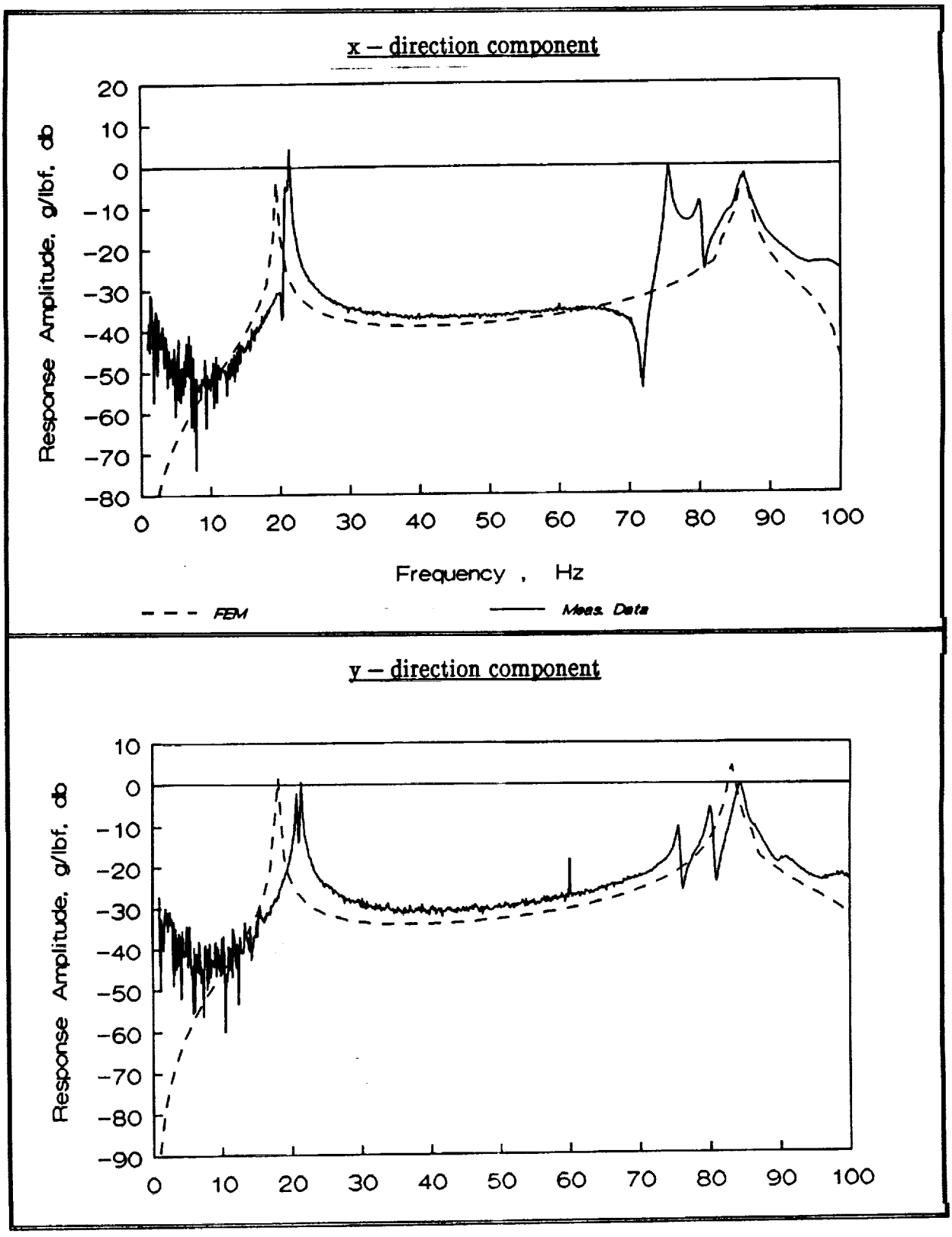

Figure 17g. Comparison of experimental and analytical frequency response functions, cantilevered (no shaft) configuration, accelerometer location 8R

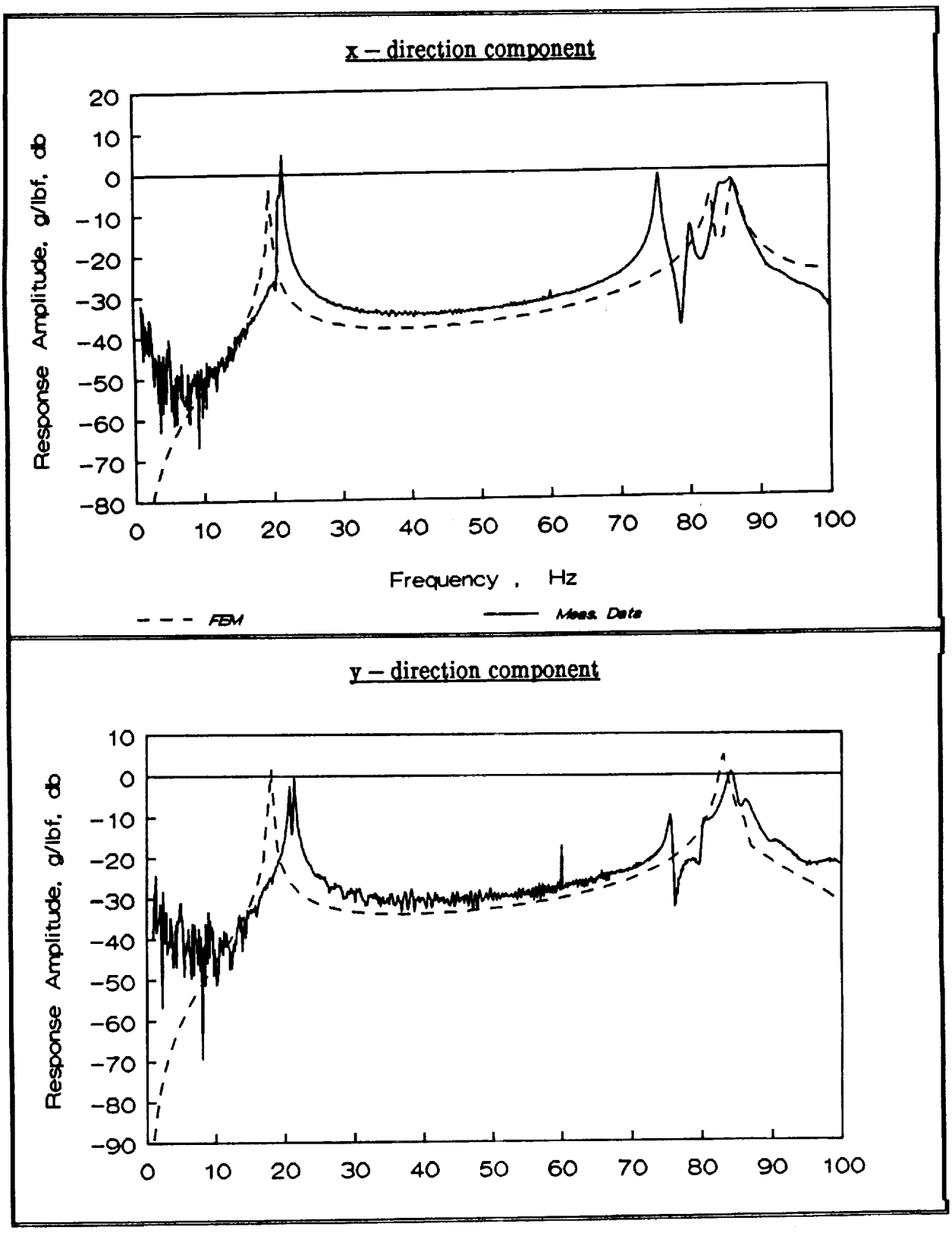

Figure 17h. Comparison of experimental and analytical frequency response functions, cantilevered (no shaft) configuration, accelerometer location 8L

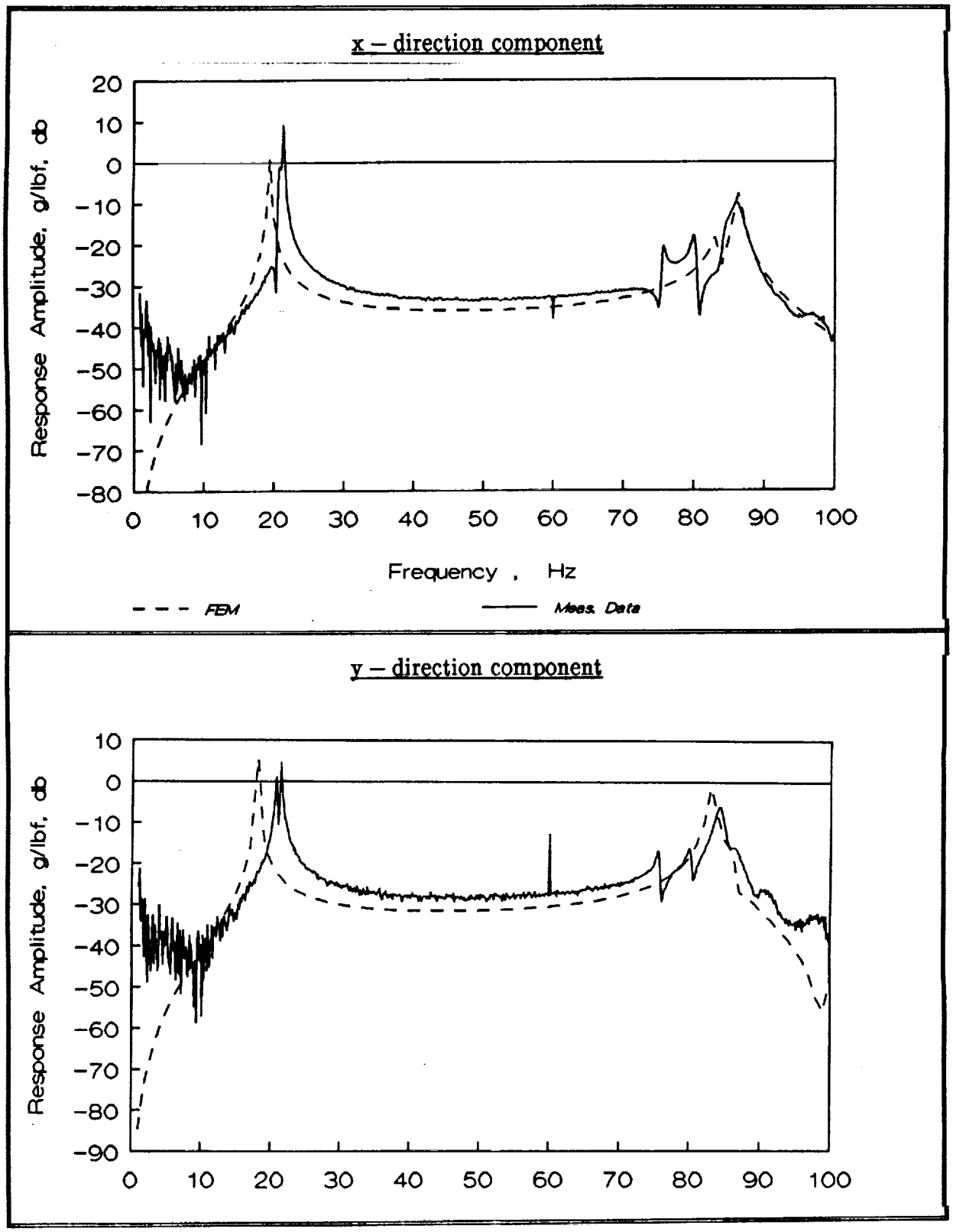

Figure 17i. Comparison of experimental and analytical frequency response functions, cantilevered (no shaft) configuration, accelerometer location 9R

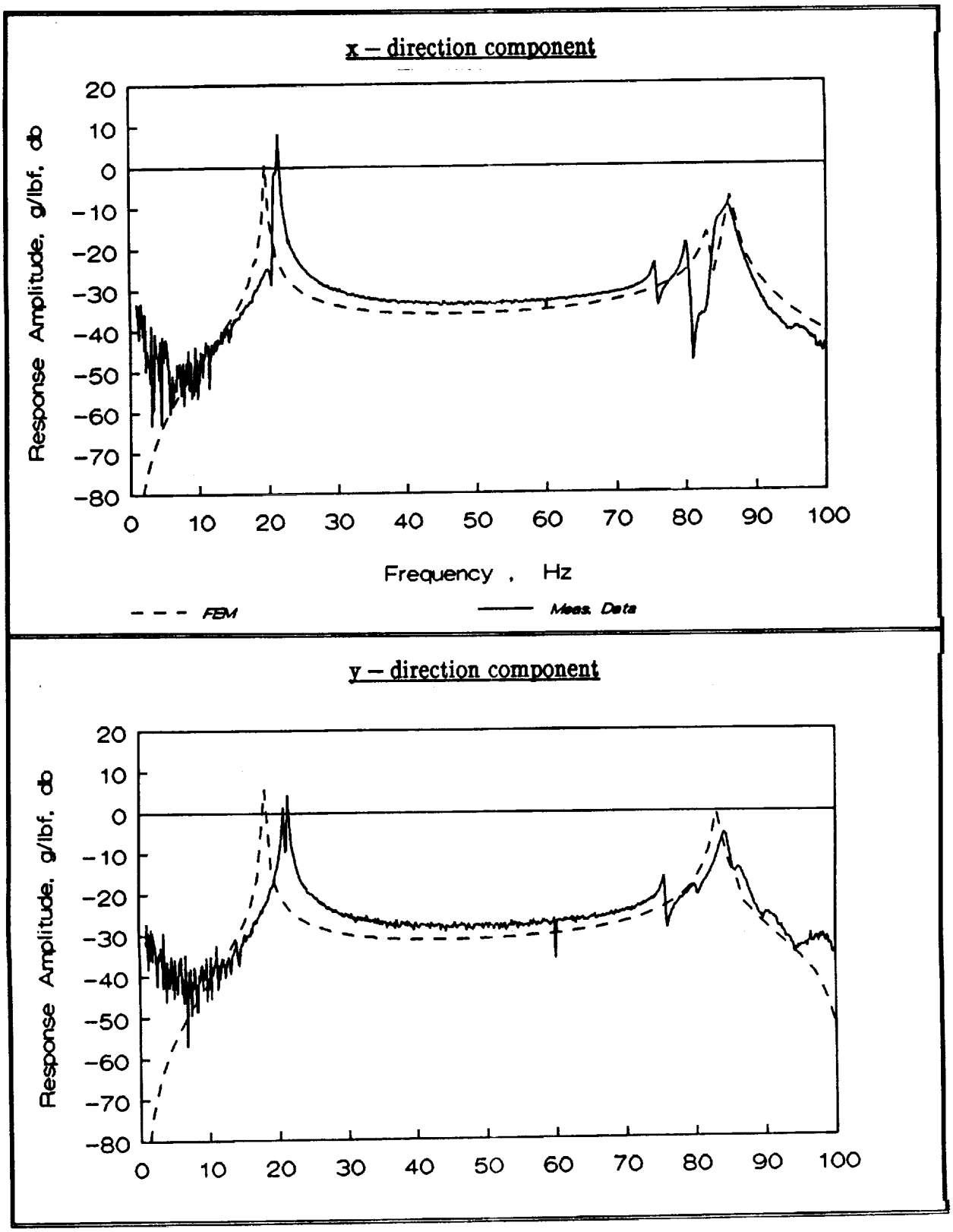

Figure 17j. Comparison of experimental and analytical frequency response functions, cantilevered (no shaft) configuration, accelerometer location 9L

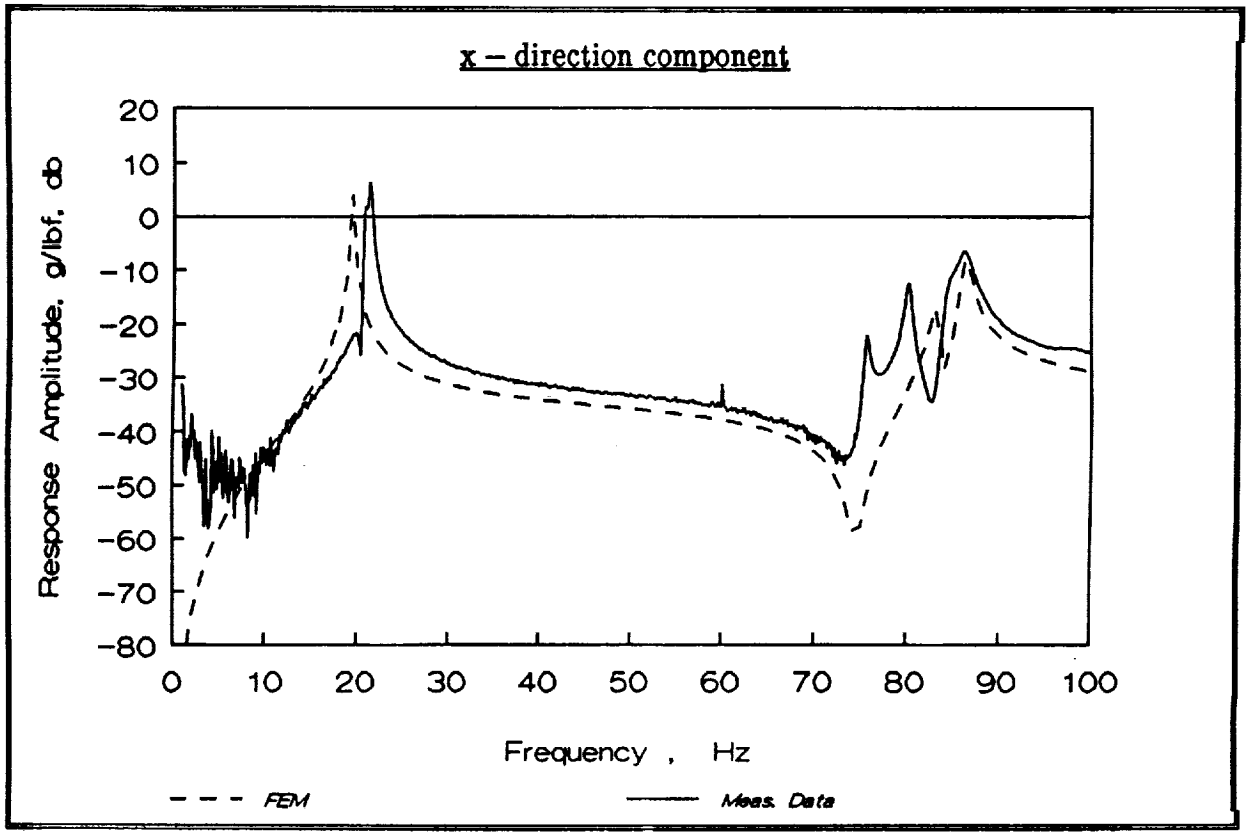

Figure 17k. Comparison of experimental and analytical frequency response functions, cantilevered (no shaft) configuration, accelerometer location 10R

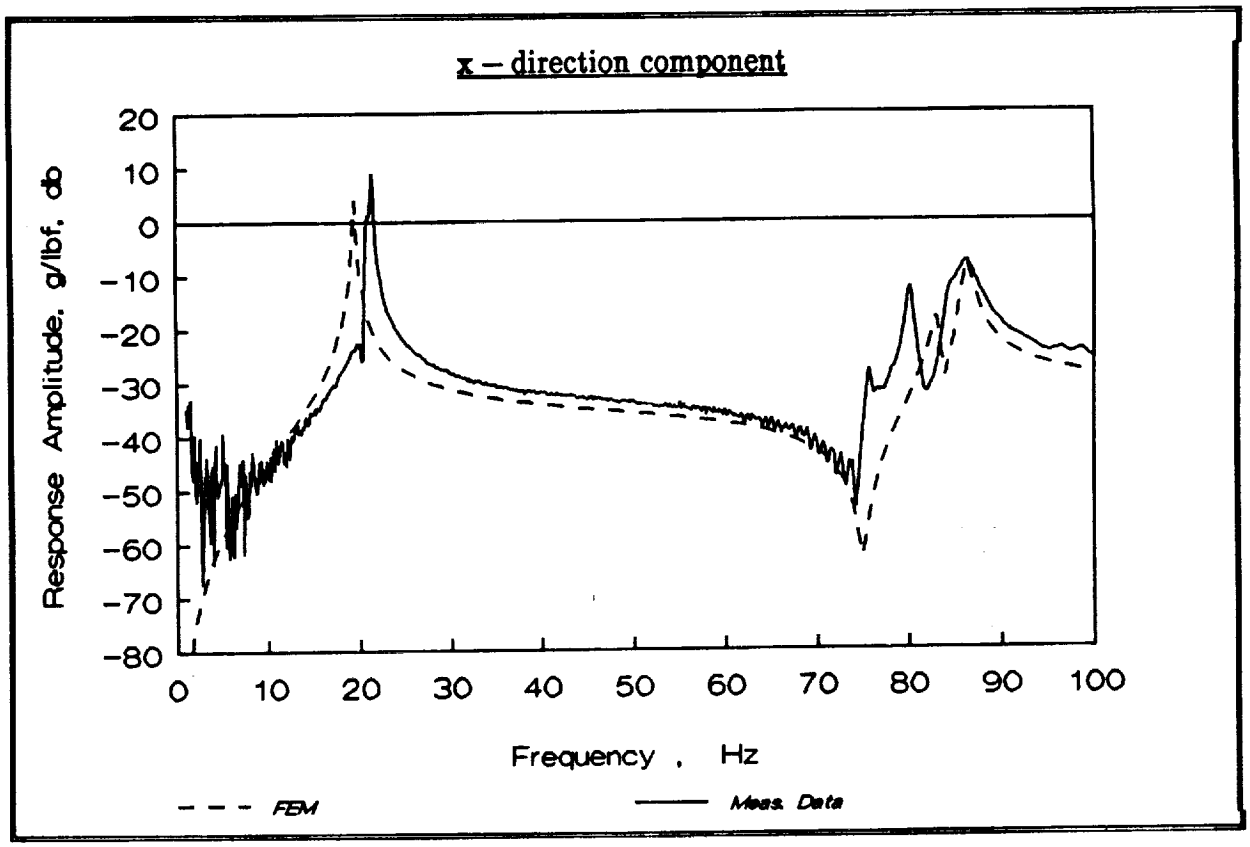

Figure 171. Comparison of experimental and analytical frequency response functions, cantilevered (no shaft) configuration, accelerometer location 10L

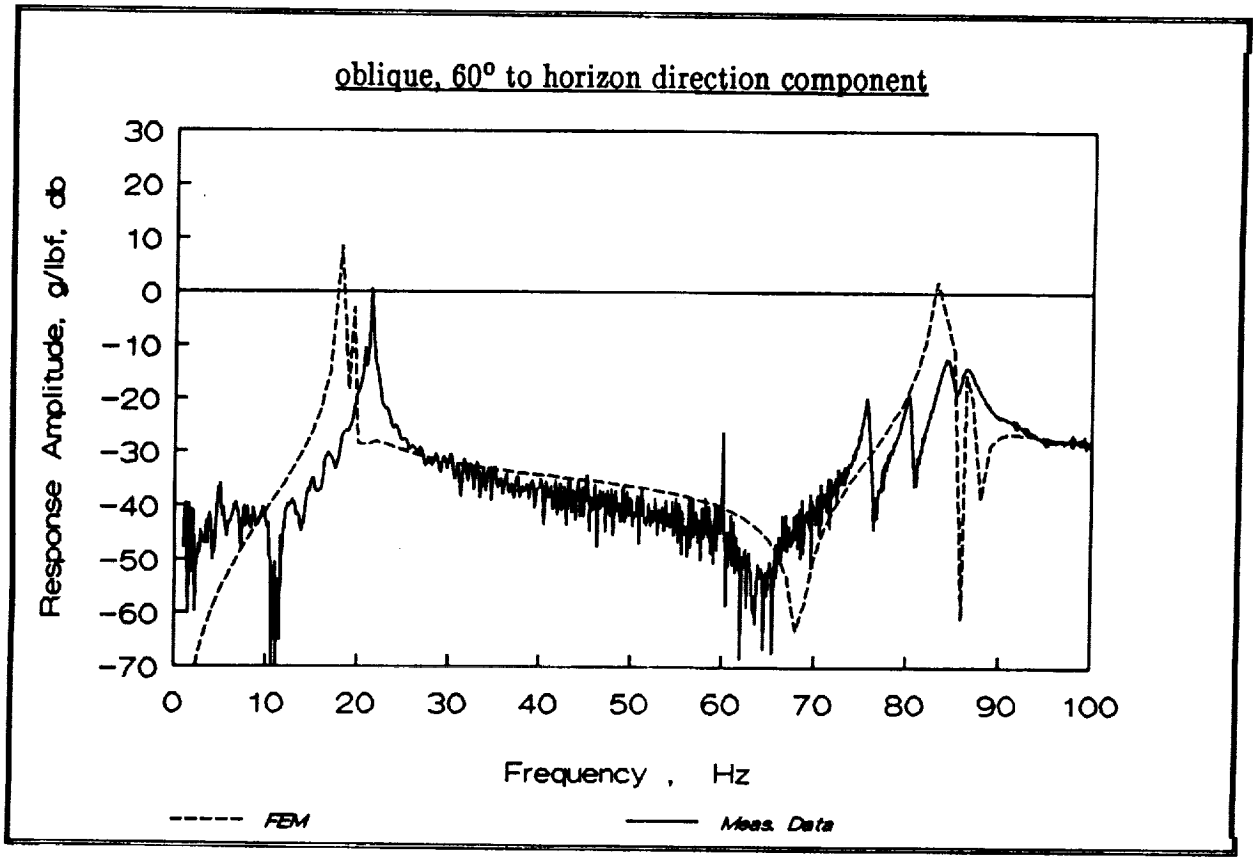

Figure 17m. Comparison of experimental and analytical frequency response functions, cantilevered (no shaft) configuration, accelerometer location 12L

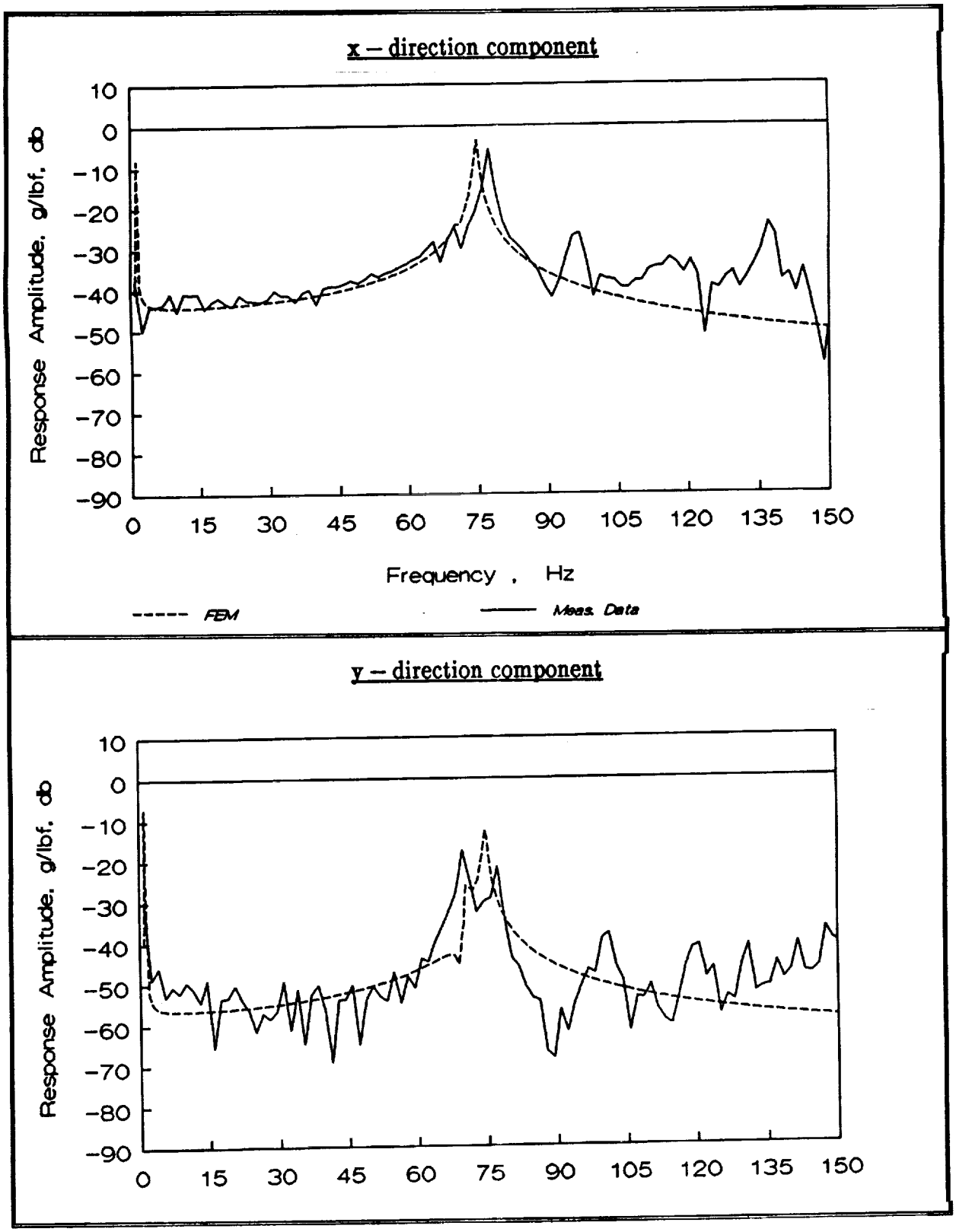

Figure 18a. Comparison of experimental and analytical frequency response functions, simulated free–free configuration, accelerometer location 2R

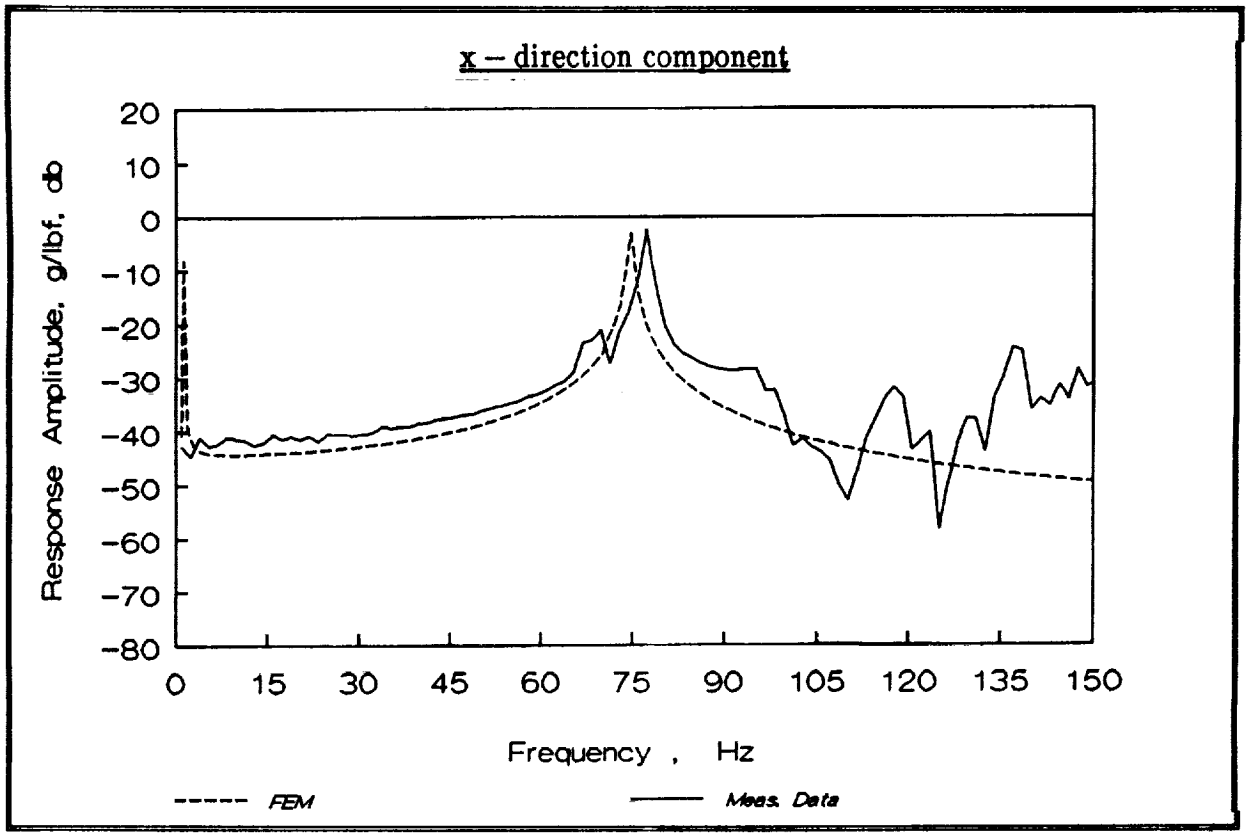

Figure 18b. Comparison of experimental and analytical frequency response functions, simulated free–free configuration, accelerometer location 2L

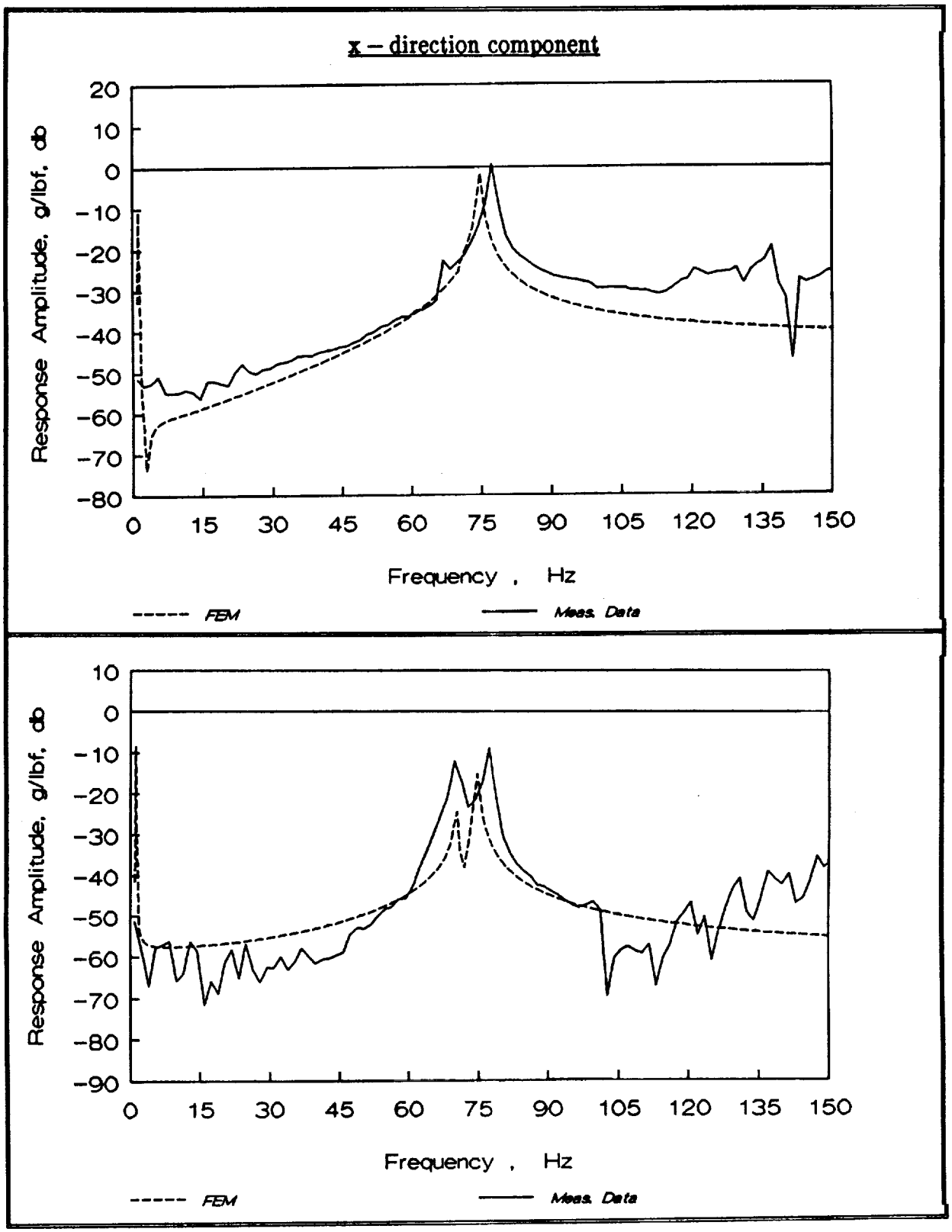

Figure 18c. Comparison of experimental and analytical frequency response functions, simulated free–free configuration, accelerometer location 4R

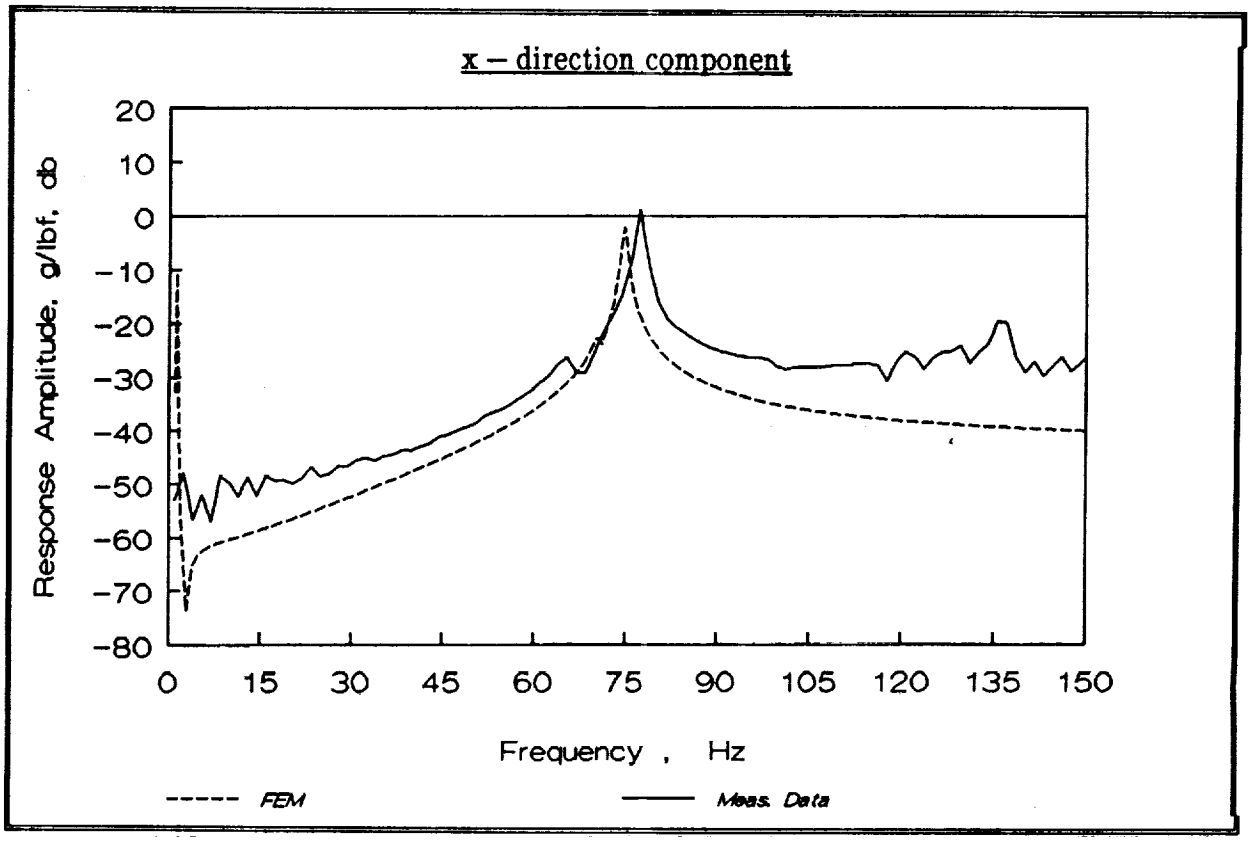

Figure 18d. Comparison of experimental and analytical frequency response functions, simulated free–free configuration, accelerometer location 4L

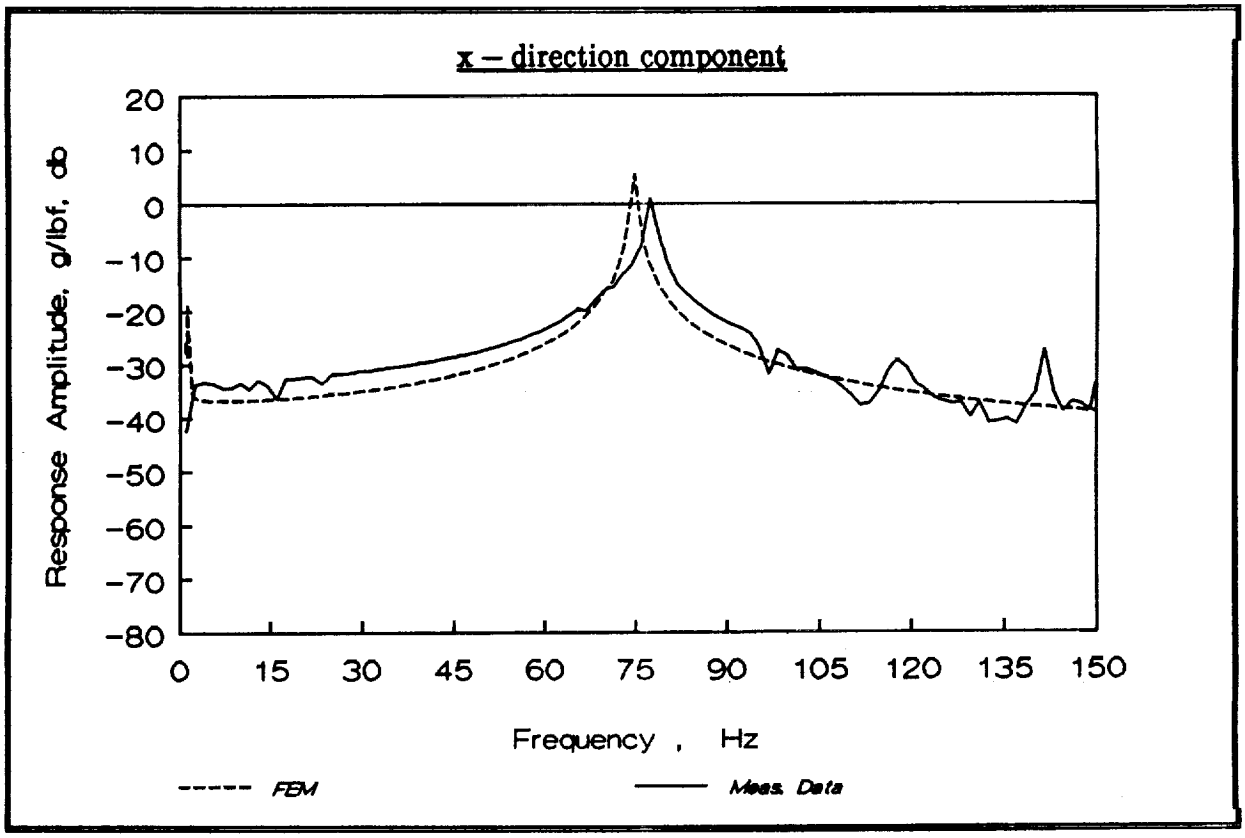

Figure 18e. Comparison of experimental and analytical frequency response functions, simulated free–free configuration, accelerometer location 8L

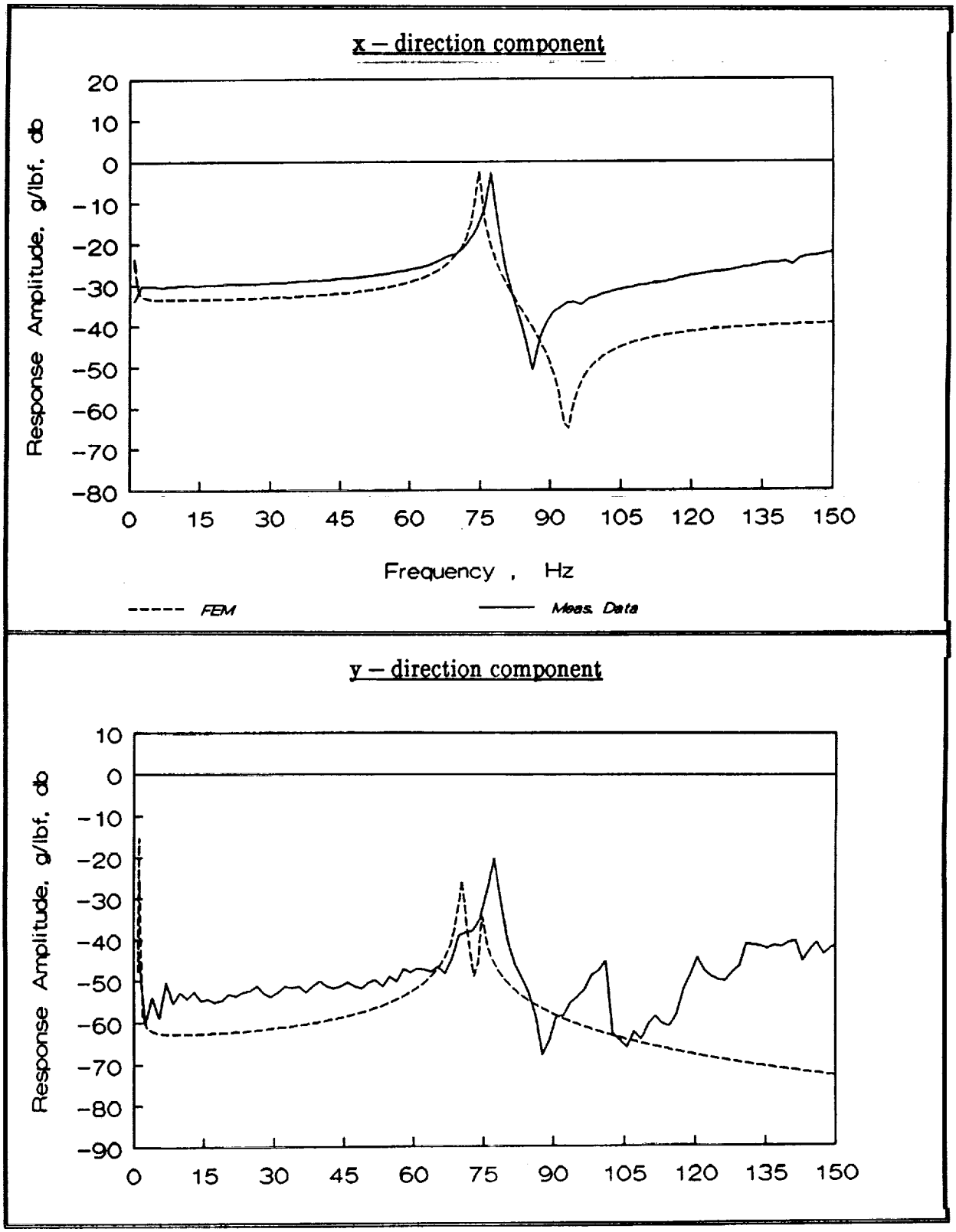

Figure 18f. Comparison of experimental and analytical frequency response functions, simulated free–free configuration, accelerometer location 9R

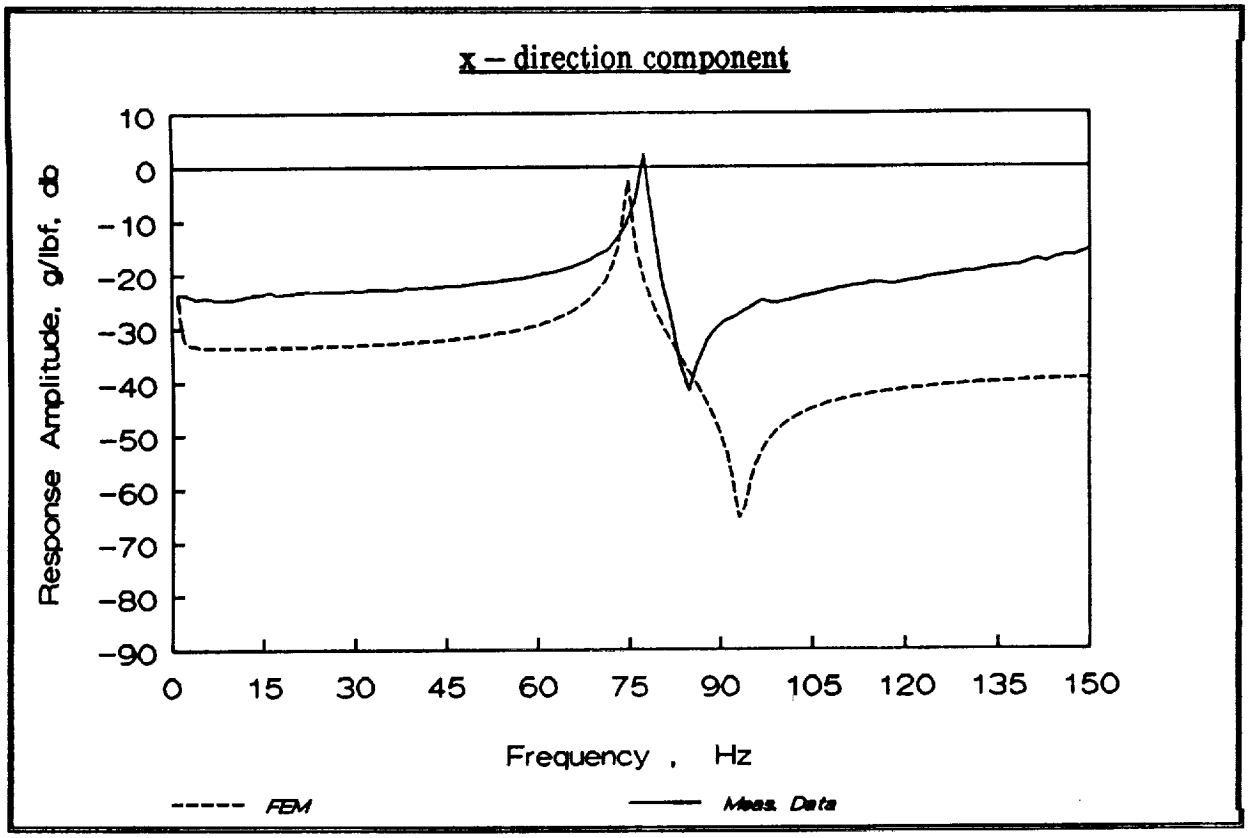

Figure 18g. Comparison of experimental and analytical frequency response functions, simulated free–free configuration, accelerometer location 9L

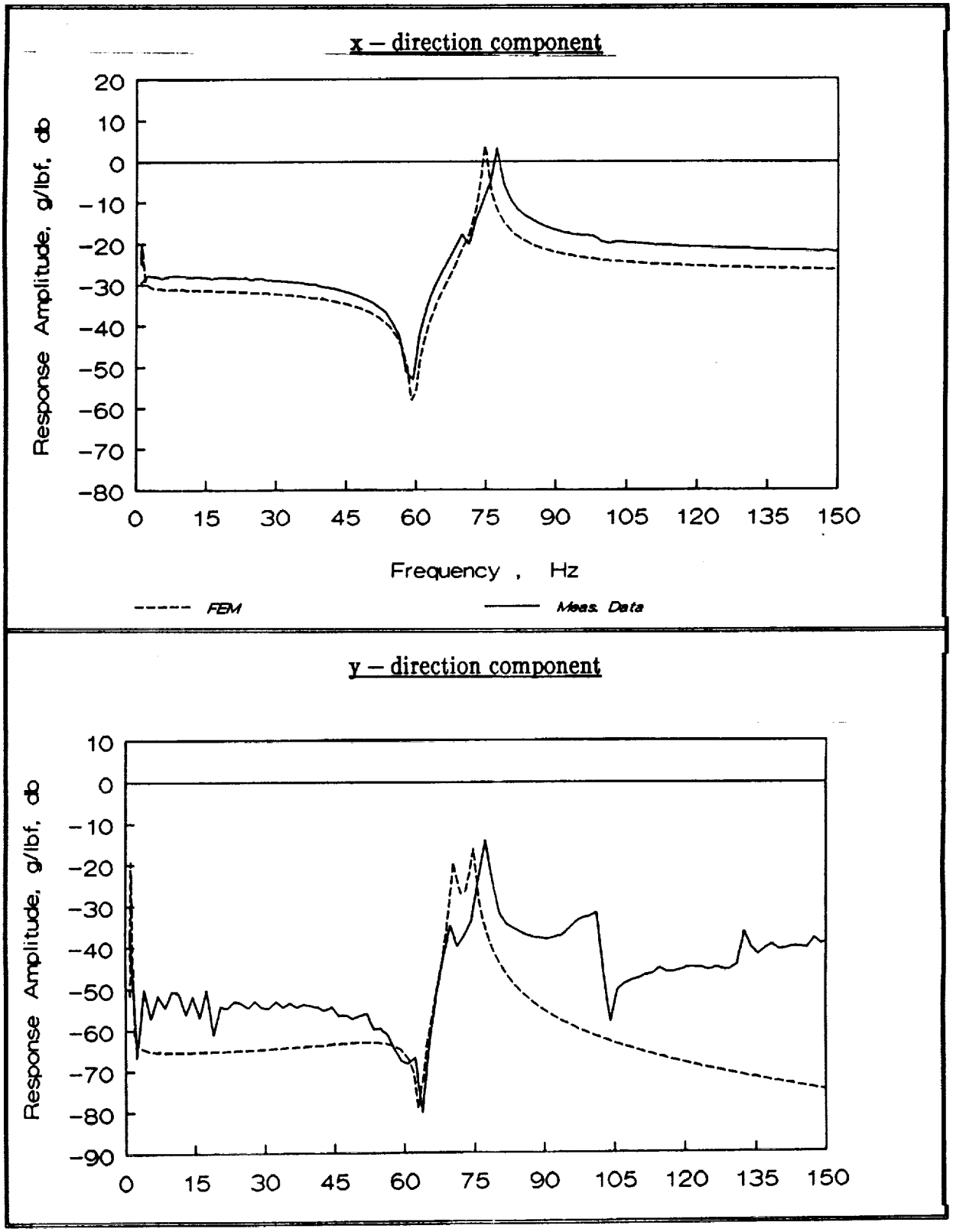

Figure 18h. Comparison of experimental and analytical frequency response functions, simulated free–free configuration, accelerometer location 10R

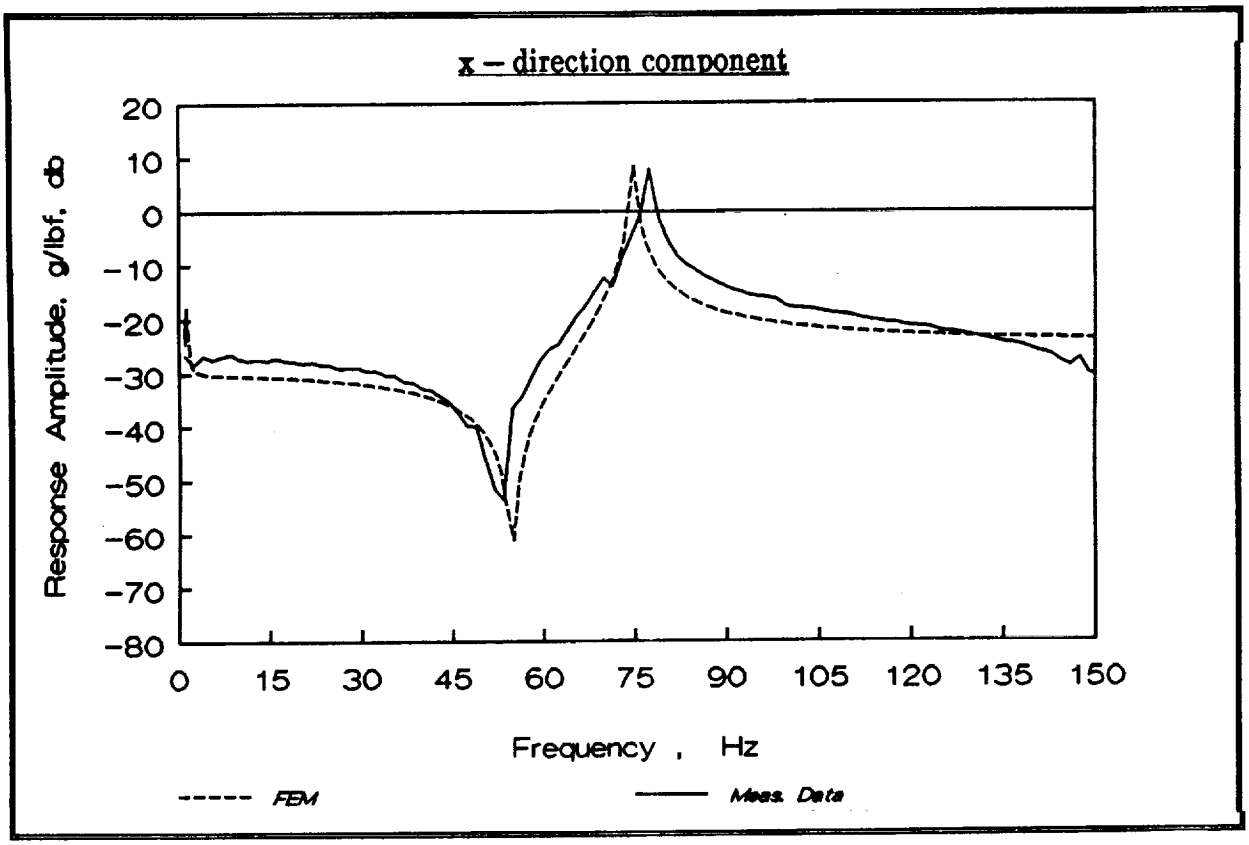

Figure 18i. Comparison of experimental and analytical frequency response functions, simulated free–free configuration, accelerometer accelerometer location 11L

NASA
National Aeronautics and Space Administration

Report Documentation Page

1. Report No.	2. Government Accession No.	3. Recipient's Catalog No.
NASA CR-187576		

4. Title and Subtitle
Static Strain and Vibration Characteristics of a Metal Semimonocoque Helicopter Tail Cone of Moderate Size

5. Report Date
June 1991

6. Performing Organization Code
RTC D-91-1

7. Author(s)
Richard L. Bielawa, Rachel E. Hefner, and Andre Castagna

8. Performing Organization Report No.

10. Work Unit No.
505-63-36-01

9. Performing Organization Name and Address
Rensselaer Polytechnic Institute
Troy, NY 12180-3590

11. Contract or Grant No.
NAG1-807

13. Type of Report and Period Covered
Contractor Report

12. Sponsoring Agency Name and Address
National Aeronautics and Space Administration
Washington, DC 20546-0001

14. Sponsoring Agency Code

15. Supplementary Notes
Langley Technical Monitor: Raymond G. Kvaternik
Final Report

16. Abstract

This report presents the results of an analytic and experimental research program involving a Sikorsky S-55 helicopter tail cone directed ultimately to the improved structural analysis of airframe substructures typical of moderate sized helicopters of metal semimonocoque construction. The study included experimental static strain and dynamic shake-testing measurements as well as correlation studies of each of these tests with a PC-based finite element analysis (COSMOS/M). The tests included static loadings at the end of the tail cone supported in the cantilevered configuration as well as vibrational shake-testing in both the cantilevered and free-free configurations. Generally, excellent to very good correlations were achieved for the first order elasto-mechanical effects. The tests and correlational analyses, while falling short of the ultimate objectives of effecting improved correlation and detailed characterization of damping, represent achievement in firmly establishing the RPI Shake-Test Facility as well as the basic finite element modeling of the S-55 tail cone, as operational resources. As a result, these resources are now poised to address the ultimate objectives identified above.

17. Key Words (Suggested by Author(s))	18. Distribution Statement
Finite Element Modeling Ground-Vibration Testing Helicopter Structures	Unclassified - Unlimited Subject Category - 39

19. Security Classif. (of this report)	20. Security Classif. (of this page)	21. No. of pages	22. Price
Unclassified	Unclassified	130	A07